DISSERTATION

Improvements and applications of quantitative single molecule localization microscopy

ausgeführt zum Zwecke der Erlangung des akademischen Grades eines Doktors der technischen Wissenschaften unter der Leitung von

Univ. Prof. Dipl.-Ing. Dr. Heinz Redl

E166

Institut für Verfahrenstechnik, Umwelttechnik und technische Biowissenschaften

und

FH-Prof. Dipl.-Ing. Dr. Jaroslaw Jacak

FH Oberösterreich, Institut für Medizintechnik und Angewandte Sozialwissenschaften

eingereicht an der Technischen Universität Wien

Fakultät für Technische Chemie

von

Fabian Hauser

01635637

Wien, am Februar 2023 Unterschrift

Acknowledgements

First of all, I would like to thank my supervisor Heinz Redl at the TU Wien and my co-supervisor Jaroslaw Jacak at the FH Linz. Without both of you, my thesis would not have been possible. Special thanks also go to the Austrian Cluster for Tissue Regeneration for networking and providing a stage for me to present my ideas.

A big thank you to Michael B. Fischer for his medical and scientific input and for all biological advice.

Thank you, Eleni Priglinger, for improving my cell culture skills and helping me professionalize my microfluidics. Thank you for your support and resources.

I thank Anja Peterbauer and the Red Cross Transfusion Service for supplying human platelet samples.

I thank my FH colleagues, Sandra Mayer, Markus Axmann, Martina Hofmann, Dmitry Sivun, Sandra Milic, Robert Merwa and all the others for their help, support and input, and long conversations.

I would like to thank my fellow PhD colleagues from the lab Boris Buchroithner, Florian Weber and Christoph Naderer for their time and advice.

I would like to thank my friends Markus, Nici, Behnam, Hartl, Klemens and everyone else from the APS pub (especially OT and Rexi) for their time and patience to endure my thesis.

And finally, I would like to thank my parents Renate and Gerhard as well as my sister Simone, who set me on the path to this PhD a long time ago.

Table of Contents

Abstract

Single molecule localization microscopy (SMLM) covers a group of stochastic photo-switching super-resolution microscopy methods for example PALM, and STORM, in which fluorescent signals are localized using fitting algorithms. The goal is to image a sufficiently low density of non-overlapping, randomly active fluorophores to determine their sub-pixel position and reconstruct a super-resolved image from thousands of images. Localization of sparsely distributed single molecule signals allows SMLM to break the resolution limit and localize emitter centres with sub 20 nm precision.

In the four contributions included in this thesis, I applied SMLM and advanced software tools to analyse the morphology of subcellular structures and the spatial distribution of proteins. In my first contribution, we applied SMLM to observe the actin cytoskeleton of platelets at different morphological states. The three major actin reorganization states of platelets were imaged and the width of filopodia was determined. Improved imaging buffers containing glycerol and an oxygen-scavenger system allowed the localisation of single molecule signals with an accuracy of 12 nm. In the second contribution, we developed software tools for comparative analysis of protein distributions. We studied the distribution of CD41 (integrin α-IIb) and CD62P (P-selectin) in an artificial platelet clot model using 3D SMLM. Hierarchical clustering confirmed that CD41 and CD62P have different distributions at the nanoscale level. In the third contribution, I improved real-time 3D SMLM localization algorithm by combining the least-square approach with template images. Automated control of a reactivation laser based on real-time localizations allowed to counteract photo-bleaching and to ensure optimal molecule density throughout the experiment. In my final contribution, I developed a platform combing microfluidics, simultaneous two-colour 3D SMLM and advanced software tools. This platform was applied to a blood vessel model to study platelet activation on the endothelial monolayer under flow conditions. Our results prove a link between activated platelets and stressed endothelial cells determined via machine learning assisted mitochondrial morphology analysis. Furthermore, laser-treated cells showed no sign of platelet activation. Quantitative analysis of platelet volumes showed that dynamic incubated platelets on an endothelial monolayer have increased volumes compared to static incubation.

In summary, the work presented in this thesis demonstrated that advanced software tools in combination with SMLM enable a more detailed analysis of subcellular processes, cellular structures, and protein distribution at a nanometre level. Automation, real-time analysis, and improved imaging buffers increased the image quality necessary for precise post-processing. Simultaneous two-colour SMLM has proven its utility in linking nanoscale protein distributions with macroscopic subcellular structures in 3D.

Kurzfassung

Die Einzelmoleküllokalisationsmikroskopie (single molecule localization microscopy, SMLM) umfasst eine Gruppe von stochastischen photo-schaltenden hochauflösenden Mikroskopie Methoden, z.B. PALM und STORM, bei denen Einzelmolekülpositionen mit Hilfe von Algorithmen lokalisiert werden. Ziel in SMLM ist es eine ausreichend geringe Dichte an nicht überlappenden und zufällig aktiven Fluorophoren auf einem einzelnen Bild aufzunehmen. Die bestimmten Einzelmolekülpositionen von mehreren tausend dieser Bilder werden dann verwendet, um ein einzelnes hochauflösendes Bild zu rekonstruieren. Die Lokalisierung von spärlich verteilten Einzelmolekülsignalen ermöglicht SMLM, die Auflösungsgrenze zu durchbrechen und Einzelmolekülzentren mit einer Genauigkeit von unter 20 nm zu bestimmen.

In den vier Beiträgen dieser Arbeit habe ich SMLM und fortschrittliche Softwaretools eingesetzt, um die Morphologie subzellulärer Strukturen und die räumliche Verteilung von Proteinen zu analysieren. Im ersten Beitrag haben wir SMLM angewandt, um das Aktin-Zytoskelett von Thrombozyten in verschiedenen morphologischen Zuständen zu beobachten. Die drei wichtigsten Zustände von Thrombozyten wurden dabei aufgenommen und die Breite der Filopodien wurde bestimmt. Verbesserte Bildgebungspuffer, die Glycerin und ein Sauerstoffabfangsystem enthielten, ermöglichten die Lokalisierung von Einzelmolekülsignalen mit einer Genauigkeit von 12 nm. Im zweiten Beitrag entwickelten wir Software-Tools für die vergleichende Analyse von Proteinverteilungen. Dabei untersuchten wir die Verteilung von CD41 (Integrin α-IIb) und CD62P (P-Selektin) in einem künstlichen Modell eines Blutgerinnsels mittels 3D SMLM. Hierarchisches Clustering bestätigte, dass CD41 und CD62P unterschiedliche Verteilungen im Nanometerbereich aufweisen.

In meinen dritten Beitrag habe ich Echtzeit-3D-SMLM-Lokalisierungsalgorithmus verbessert, indem ich die least-square Methode mit Vorlagenbildern von Einzelmolekülen kombiniert habe. Die automatische Steuerung eines Reaktivierungslasers auf der Grundlage von Echtzeit-Lokalisierungen ermöglichte es, dem Effekt von gebleichten Fluorophoren entgegenzuwirken und während des gesamten Experiments eine optimale Moleküldichte zu gewährleisten. In meinem letzten Beitrag habe ich eine Plattform entwickelt, die Mikrofluidik, simultane zweifarbige 3D-SMLM und fortschrittliche Softwaretools kombiniert. Diese Plattform wurde auf einem Blutgefäßmodell angewandt, um die Thrombozytenaktivierung auf dem Endothel

unter Strömungsbedingungen zu untersuchen. Unsere Ergebnisse belegen eine Verbindung zwischen aktivierten Thrombozyten und gestressten Endothelzellen, die mit Hilfe von maschinellem Lernen unterstützter Analyse der mitochondrialen Morphologie festgestellt wurde. Darüber hinaus zeigten laserbehandelte Endothelzellen keine Anzeichen einer Thrombozytenaktivierung. Schließlich zeigte die quantitative Analyse der Thrombozytenvolumina, dass dynamisch inkubierte Thrombozyten auf dem Endothel ein größeres Volumen aufweisen als bei statischer Inkubation.

Zusammenfassend lässt sich sagen, dass die in dieser Arbeit vorgestellten Arbeiten zeigen, dass fortschrittliche Softwaretools in Kombination mit SMLM eine detailliertere Analyse subzellulärer Prozesse, zellulärer Strukturen und der Proteinverteilung auf Nanometerebene ermöglichen. Automatisierung, Echtzeitanalysen und verbesserte Bildgebungspuffer erhöhten die für eine präzise Nachbearbeitung erforderliche Bildqualität. Darüber hinaus zeigte die simultane 3D Zweifarben-SMLM ihre Nützlichkeit bei der Verknüpfung von Proteinverteilungen im Nanobereich mit makroskopischen zellulären Strukturen.

List of Figures

List of Abbreviations and Symbols

SMLM .... Single molecule localization microscopy

PALM .... Photoactivated localization microscopy

STORM .... Stochastic optical reconstruction microscopy

STED .... Stimulated emission depletion

MINFLUX .... Minimal photon fluxes

SOFI .... Super-resolution optical fluctuation imaging

PAINT .... Points accumulation for imaging in nanoscale topography

FRAP .... Fluorescence recovery after photobleaching

TOCCSL .... Thinning out clusters while conserving stoichiometry of labeling

PSF .... Point spread function

NA .... Numerical aperture

CMOS .... Complementary metal oxide semiconductor

EM-CCD .... Electron multiplying charge-coupled device

SNR .... Signal to noise ratio

QE .... Quantum efficiency

LED .... Light emitting diode

FPGA .... Field programmable gate array

CD .... Cluster of differentiation

CD41 .... Integrin alpha 2b

CD62P .... P-selectin

GFP .... Green fluorescent protein

IgG .... Immunoglobulin G

ROS .... Reactive oxygen species

NHS .... N-Hydroxysuccinimide

MES .... 2-(N-morpholino)ethanesulfonic acid

EGTA .... egtazic acid

LM .... Levenberg–Marquardt algorithm

MLE .... Maximum likelihood estimation

CRLB .... Cramér–Rao lower bound

DNN .... Deep neuronal network

CPU .... Central processing unit

GPU ....Graphics processing unit

SIMD ....Single instruction, multiple data

λ .... wavelength

n .... refractive index

N .... total number of photons

σ .... Gaussian sigma (width)

1 Introduction

1.1 Microscopy

Optical microscopes are designed to magnify and enhance the image of a specimen to allow for observations in the micrometre domain. Image quality is influenced by magnification, contrast, and aberrations. However, it has been known since 1873 that light microscopy is limited by diffraction to a spatial resolution of roughly 250 nm [1]. Structures with finer features cannot be distinguished from each other. Abbe couldn't improve resolution even with more precisely manufactured lenses. The reason is due to the limited light collection of objective lenses. Due to the objective lens aperture, light can only be collected within a limited angular range and is described by the numerical aperture (NA). Consequently, point-light sources appear on the imaging plane as an Airy function which is the impulse response of the point-light source convolved with objective lens aperture. Usually, these diffraction patterns of point-light sources deviate from the ideal Airy function due to aberrations introduced by the optical system (microscope) and are then called point spread function (PSF).

One possibility to improve image quality is to use contrast-enhancing microscopy extension. In bright-field microscopy, specimens are uniformly illuminated using white light. The contrast in the image is caused by light absorption and attenuates intensities in dense areas. Contrast-increasing techniques such as phase contrast microscopy use a phase-shift and filter ring to visualise phase shifts as brightness variations. Dark-field microscopy utilizes a condenser phase ring to stop parts of the light so that only scattered light is imaged. Differential interference contrast microscopy utilizes interference of polarized light to increase the contrast. Usually, interfaces with different refractive indices are well highlighted by this method.

Although bright-field microscopy can resolve cellular detail by contrast-enhancing techniques, subcellular structures are often difficult to distinguish from one another. Fluorescence microscopy provides a significant improvement in contrast. Fluorescent labelling allows subcellular structures and specific proteins to be stained by fluorescent dyes. Fluorescence microscopy uses highly concurrent and frequency-specific light sources (e.g., lasers) to excite fluorescent dyes. Additional filters for specific fluorophores help to block unwanted wavelengths from reaching the camera and further increase the contrast. However, fluorophores

outside of the desired focal plane are still illuminated, which decreases the quality of fluorescence imaging. To avoid out-of-focus emissions, several methods have been proposed. In light-sheet fluorescence microscopy, a thin slice of the specimen is illuminated perpendicular to the optical axis. Cylindrical lenses have been proposed for illumination from the side. The specimen is axially moved though this beam [2]. Furthermore, total internal reflection fluorescence microscopy uses critical angle illumination where the fluorophores are only excited by evanescence waves a few hundred nanometres above the coverslip (typically < 100 nm, up to 200 nm) [3].

1.2 Image acquisition

Two major technologies are currently used for scientific applications: charge-coupled device (CCD) and complementary metal-oxide semiconductor (CMOS) cameras. The quality of images captured by modern camera sensors depends not only on sensor size, pixel size or pixel density but also on the achievable signal-to-noise ratio (SNR) and quantum efficiency (QE) of the device. SNR and QE are inherently wavelength dependent due to photon absorption or reflection in the silicon layers. In some applications, it can be beneficial to use cameras with smaller sensors and low pixel densities to collect more photons on fewer pixels, which increases the contrast and photon count. Equally important is the consideration of noise. Read noise adds Gaussian distributed intensities to the camera pixel values and originates from the photoelectron conversion process. Dark noise or dark currents result from thermally generated electrons that influence camera pixel values. Finally, shot noise introduces random high-value intensity spikes from natural photon fluctuations (quantum fluctuations) or high energy radiation (cosmic or background radiation) [4].

Cooled and electron-multiplier CCD (EM-CCD, typically back-illuminated) produce high-quality images even in low-light conditions (read noise < 1 e$^-$ with EM gain) by amplifying photoelectron signals before digital conversion (QE up to 97%). EM-CCDs are well-suited for high-sensitive microscopy but have relatively low readout speeds (pixel readout rate ~20 MHz). In comparison, scientific CMOS (sCMOS) cameras solve this problem by utilizing active camera pixels to archive higher readout speed (~500 MHz), higher pixel densities and larger chip sizes. sCMOS cameras are also well-suited for high-sensitive microscopy (read noise 1 ~ 2 e$^-$), and back-illuminated cameras with QE of 95% were reported [5]. However, sCMOS cameras introduce an additional pixel-depended noise (non-uniform read noise) [6]. To

counteract this sCMOS specific noise, several correction algorithms have been developed and implemented by the scientific community [4].

Important for fluorescence microscopy experiments is also the time-sensitive control and synchronization of the exposure systems (e.g., lasers, LEDs) with the camera. This precise control of camera triggers and illumination sources is critical for fluorescence experiments with low photon yield or time-sensitive illumination sequences (e.g. "fluorescence recovery after photobleaching" (FRAP) [7], "thinning out clusters while conserving stoichiometry of labelling" (TOCCSL) [8], or other bleaching protocols). Timings should be precise down to microseconds. In general, standard computers are incapable of real-time control and specialized hardware is required. Arduino microcontrollers are often utilized for automation and signal generation due to their simplicity and cost [9, 10]. Other commercial solutions from National Instruments (DAQ cards) or Triggerscope (Advanced Research Consulting) use predefined protocols that are sent to the device prior to the start of the sequence. Furthermore, field programmable gate arrays (FPGAs) have been used as a controller with microseconds resolution and parallel input/output control [9–11]. A widely used and open-source software for controlling microscopy systems is "micromanage". It provides an extensive library of controllable hardware components (e.g. different lasers, cameras, positioning stages, …) and a user interface to combine, configure and control hardware [12].

1.3 Breaking the diffraction limit

A measure for the spatial resolution limit or diffraction limit was proposed by Rayleigh. It is defined as the minimum distance d at which two point-light sources with overlapping point spread functions - PSFs can still be distinguished from each other. Rayleigh's resolution [11] is defined as $d = 0.61 \frac{\lambda}{NA}$, where λ is the wavelength of the point light source and NA is the numerical aperture of an objective lens in epi-configuration. Another definition of resolution can be derived from the Fourier transform of the PSF. The Abbe criterion states that the absolute value of the Fourier-transformed PSF, which gradually decays with increasing spatial frequency, reaches zero at a maximum frequency k_{max} (due to the limited collection of information from spatial frequencies). Finally, the Abbe diffraction limit for lateral resolution $d_{x,y} = \frac{\lambda}{2NA}$ can be derived from the inverse of k_{max} [11]. Similarly, the axial resolution can be calculated by the Abbe criterion, which results in $d_z \approx \frac{2n\lambda}{(NA)^2}$, where n is the refractive index.

Overall, the spatial resolution limit of about 250 nm ($\lambda \sim 700\ nm, NA \sim 1.4$), cannot be overcome with conventional optical microscopes and lenses.

At the end of the 20th century, several fluorescence microscopy techniques crossed the diffraction limit. These methods are referred to as super-resolution fluorescence microscopy or nanoscopy. Eric Betzig, Stefan W. Hell, and William E. Moerner were honored with the Nobel Prize in Chemistry for the development of super-resolution fluorescence microscopy (2014). Stefan W. Hell developed a super-resolution scanning method, stimulated emission depletion (STED) microscopy, which uses an excitation laser pulse and a depletion laser pulse with a central zero-intensity spot generated by PSF engineering (doughnut-shaped). This eliminates all fluorescence signals outside of this central spot, resulting in a much smaller volume in which the fluorophores can emit photons [12]. Dependent on the illumination (pulsed or continuous), a typical resolution of less than 30 nm for organic fluorophores is possible for STED. Improvements to STED such as LocSTED, which involve sub-pixel fitting of fluctuations in STED images, could resolve molecules down to at least 15 nm resolution [13]. In addition, MINFLUX, a tracking/triangulation method, achieved sub-nanometre resolution using the STED principle [14].

In 1989, William E. Moerner was the first to detect a single fluorescent molecule [15]. Later, he found that green fluorescent protein derivatives can be turned on and off using two different wavelengths of light [16]. Based on the work of Moerner, Eric Betzig developed a stochastic super-resolution method that trades temporal resolution for an increase in spatial resolution. This involves turning off fluorophores and allowing only a small random subset of fluorophores to emit photons. The goal is to image a sufficiently low density of non-overlapping active fluorophores to determine the sub-pixel positions and reconstruct a super-resolved image from about ten thousand images. The requirement to acquire several thousands of images follows from the condition to ensure high spatial resolution during reconstruction. Depending on the application and field of view, up to 10^7 single molecule signals are required. Several strategies for stochastically switched fluorophores were developed and involve two-laser switching (photoactivated localization microscopy (PALM) [17], stochastic optical reconstruction microscopy (STORM) [18]), chemically switching (direct STORM (dSTORM) [19]), fluorescent fluctuation (Super-resolution Optical Fluctuation Imaging (SOFI) [20]), or binding kinetics (Point Accumulation for Imaging in Nanoscale Topography (PAINT) [21]). Still, stochastic blinking events of single molecule signals require image processing to reconstruct a

super-resolved image. Stochastic photo-switching super-resolution techniques that localize fluorescence signals using fitting algorithms are then referred to as single molecule localization microscopy (SMLM). In this context, SMLM can archive resolutions of 20 nm or better. The resolution gain by SMLM is dependent on the number of collected photos N per single molecule signal and increases with the square root of N.

In the context of SMLM, PSF engineering can be utilized to enable 3D imaging. In general, the width of the PSF changes with axial positions. However, the axial direction cannot be determined because the PSF is symmetric around the focus [22]. In 2008, B. Huang et al. presented astigmatism 3D SMLM to solve this problem. They added a cylindrical lens into the detection pathway to introduce additional astigmatism to the measured PSFs. Astigmatism elongates the PSF around the focus and changes the magnitude and direction of elongation depending on the axial position. Thus, additional information about the axial position is encoded into the PSF shape and the axial direction can be determined [23]. In the biplane method, two images with different focal planes are generated by a beam splitter with additional lenses. Due to the different foci of the two image planes, the axial direction can also be determined to archive 3D SMLM [24]. More sophisticated PSF engineering approaches use phase masks, deformable mirrors or spatial light modulators in the detection pathway to produce axially asymmetrical PSFs (e.g. double helix [25], tetrapod PSF [26]). These methods allow more precise localization and higher possible axial depths than astigmatism.

1.4 Chemistry of SMLM

In order to select the correct fluorescent dye for an SMLM experiment, a basic understanding of the concept of fluorescence is necessary. A characteristic feature of a dye is its ability to absorb visible light. The two electrons in the lowest molecule orbital are usually spin-paired (opposite spins, singlet state S0) and reside in a relaxed ground state. A photon absorption of a certain wavelength causes a transition from the electronic ground state to an excited electronic state. Photons with insufficient energy are not absorbed and simply pass through. The transition from the ground to an excited state (S1, S2, …) corresponds to the excitation of an electron from an occupied, binding π-orbital into an unoccupied, anti-binding π^*-orbital. Energy transitions and electronic states of a molecule can be illustrated by the so-called Jablonski diagram (see Fig 1a). The absorption colour of a dye results from the energy difference between the highest occupied and the lowest unoccupied π-orbital [27]. In general, all light-absorbing

molecules contain a central chromophore. A chromophore can consist of different chemical compounds like polymethine chains, aromatic rings, C=C, C=O, or N=N bonds. Typically, the absorption spectrum and optical properties can be modified by elongation of the chemical chains, increasing the number of π-electrons or chemical modification of end groups (changing electron acceptor-doner ratio). Typically, elongation of the conjugated electronic system shifts the maximum absorption spectrum to a longer wavelength [28] (as exemplified by Fig 1b,c).

a) Jablonski diagram   b) Cyanine3 (Cy3)   c) Cyanine5 (Cy5)
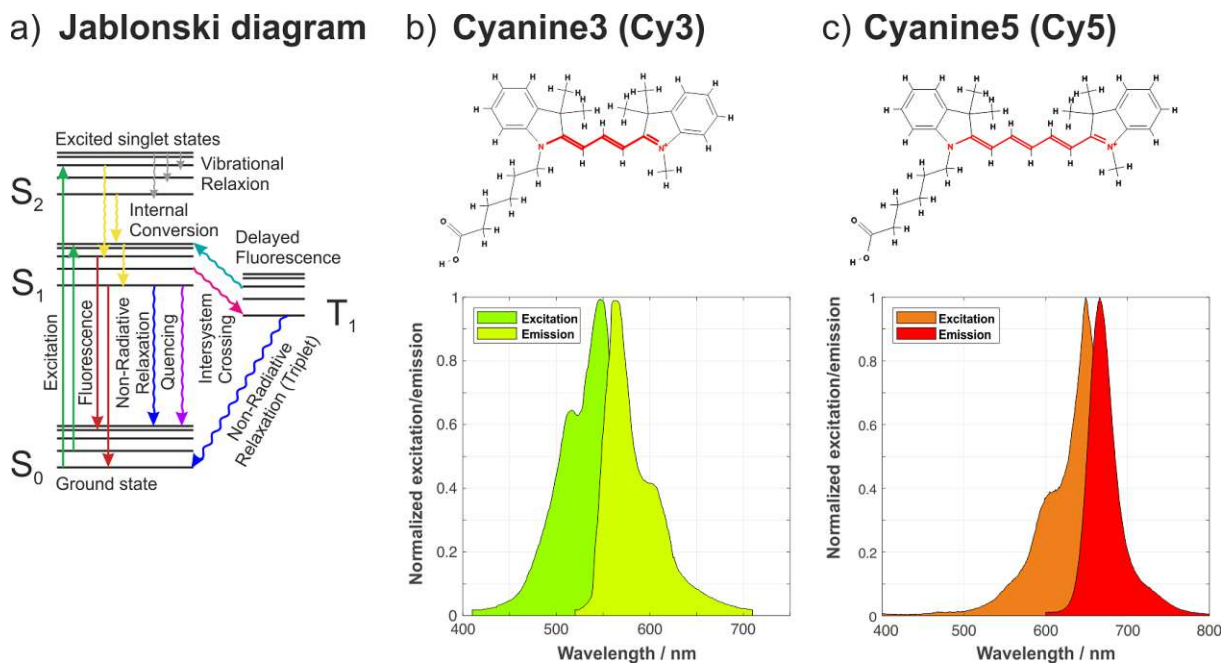
Figure 1: a) shows a Jablonski diagram with possible energy transitions and electronic states of a fluorophore. b) and c) illustrate the shift of excitation/emission wavelength with longer methine chains. The fluorescence of cyanine dyes is mostly depended on the charge delocalized between the two nitrogen atoms and the polymethine chains. b) shows the chemical structure of cyanine 3 (Cy3) and the fluorophore's excitation and emission spectrum (max. excitation at 546 nm and max. emission at 561 nm). c) shows the chemical structure of cyanine 5 (Cy5) with the fluorophore's excitation and emission spectrum (max. excitation 649 nm, max. emission 666 nm). In b) and c) the chromophore in the chemical structure is shown in red. Chemical structures are downloaded from PubChem [29] (Cy3 PubChem CID: 25228404, Cy5 PubChem CID: 25228272) are rendered using Open Babel [30]. Cy3 and Cy5 excitation/emission spectra are downloaded from fluorophores.tugraz.at.

Fluorescence occurs if the fluorescent dye or fluorophore emits a photon during the relaxation from the excited to ground state. Fluorophores in their excited electronic state always release some energy through non-radiative transitions to lower excited vibrational states. The absorption spectrums arise from the varying probability of allowed transitions that populate the various vibrational energy levels of excited states. For the relaxation back to the electronic ground state, several pathways exist with varying probabilities. In general, after a few nanoseconds (fluorescence lifetime), fluorophore release energy by photon emission via radiative transition. The emitted photon has a longer wavelength (also called Stokes shift) with a range of possible wavelengths (spectrum) due to energy loss from various transitions of

vibrational states. Rarely, nonradiative relaxation to the ground state is possible by energy release through internal conversion. This process depends on the fluorophore's chemical properties and environment. The ratio of absorbed to emitted photons is called quantum yield. In addition, excited fluorophores can also release excess energy by intramolecular and intermolecular conversion. The energy can be dissipated non-radiatively as heat or transferred to other colliding or nearby molecules via quenching or Förster resonance electron transfer.

Fluorophores can also transition to an intermediate energy state, called the electronic triplet state (T1), by intersystem crossing. This triplet state involves flipping the spin of the excited electron (rare event, forbidden quantum state) and has a prolonged lifetime (microseconds up to seconds). The probability of intersystem crossing can be tuned by chemical modification of the end groups of the conjugated electronic system [31]. During the triplet lifetime, excited molecules have a high degree of chemical reactivity and promote the production of harmful free radicals. Electron transfer reactions can lead to a non-fluorescent radical state ($F^{\bullet-}$, lifetime of seconds to minutes), also called dark or OFF state. Fluorophores in this state are more susceptible to photobleaching. While quenching is reversible and involves the reduction of excited state lifetimes and induces non-radiative relaxation, bleaching is permanent and arises from photon-induced chemical damages or covalent modifications. Molecular oxygen affects the fluorophore's state transitions from the triplet state to the ground state. Since molecular oxygen usually occurs in the triplet ground state, it easily reacts with fluorophores in the triplet state via an electron transfer reaction. However, when molecular oxygen reacts in the singlet state, reactive oxygen species (ROS) are formed, which promotes photobleaching [32]. The accumulation of ROS can be counteracted by enzymatic oxygen-scavenging systems (i.e. buffer containing glucose, glucose oxidase, and catalase), which reduces oxygen during enzymatic reactions [33]. And yet oxygen plays an important role in quenching the triplet state. The depletion of molecule oxygen can lead to an overpopulation of fluorophores in the triplet state, decreasing photon yield. Reducing agents such as mercaptoethylamine and β-mercaptoethanol, potassium iodide, dithiothreitol or Trolox can favour the conversion of fluorophores to their dark state. In addition, deprivation of oxygen can lead to prolonged dark states, as oxidation of the fluorophore is required for returning to the ground state. In praxis, complete oxygen removal is impossible, and residual oxygen allows individual fluorophores to stochastically return to the ground state.

Photo-switchable fluorophores are the main choice for SMLM experiments because they can

be reversibly switched from an ON to an OFF state. In 2006, E. Betzig et. al. proposed the PALM method for SMLM. Originally, PALM used a photoactivatable fluorescent protein, where isolated single molecules were activated, resulting in lower-density images, and subsequently bleached [17]. In the same year, M. J. Rust et al. presented STORM that uses fluorescent dye-pairs, where an activator dye (e.g., Alexa 405, Cy2, Cy3) is used to reactivate the main dye (e.g. Cy5, Alexa 647, Cy5.5, Cy7). Cy5 a cyanine dye was reported to be photo switchable between an ON and OFF state using laser pulses of different wavelengths. Illuminating Cy5 with a red laser pulse produces fluorescent emission and switches it into a dark state. The fluorophores can be reactivated using green laser pulses, but recovery rates are improved using a second activation dye like Cy3. They also showed that the dye-pair can be cycled hundreds of times before bleaching [18]. Chemical photo-switching like in dSTORM is archived by embedding rhodamine dyes like Alexa 647 in aqueous buffers containing thiol (i.e. mercaptoethylamine). During excitation, the fluorophore stochastically enters a triple state in which the thiol buffer reduces the molecule into the dark state ($F^{\bullet-}$) and reaction with oxygen allows the fluorophores to transition back to its ground state. It was also shown that this cycling can be repeated hundreds of times before fluorophores bleach [19].
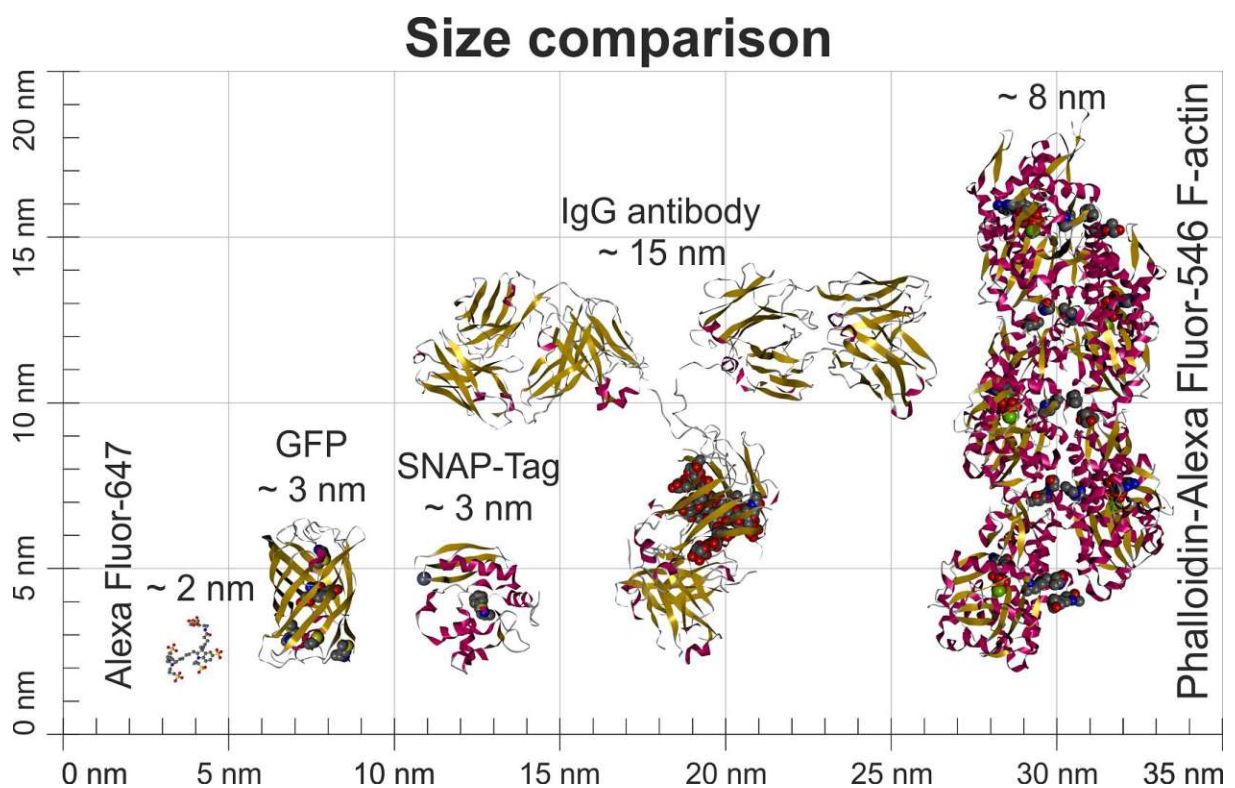
Figure 2: Size comparison of Alexa Fluor 647, green fluorescent protein (GFP), labelling protein SNAP-tag [34, 35], immunoglobulin G (IgG) antibody and F-actin labelled with phalloidin Alexa Fluor 546 with an approximate diameter of 2 nm, 3 nm, 3 nm, 15 nm and 8 nm, respectively. Proteins and molecules are rendered using the visualization toolkit (VTK) [36]. All proteins 3D models are from rcsb.org (protein data bank [37]): GFP (PDB ID: 1EMA [38]), SNAP-Tag (PDB ID: 3L00), IgG (PDB

ID: 1IGT [39]*) and phalloidin Alexa Fluor 546 F-actin (PDB ID: 6T25* [40]*).*

There are two major classes of fluorophores for SMLM: synthetic dyes (<2 nm in size, Fig 2) and fluorescent proteins (~3 nm is size, Fig 2). Fluorescent proteins can be fused or genetically encoded to the biomolecule of interest using recombinant expression in live cells. However, a major disadvantage of fluorescent proteins is their vulnerability to photobleaching and unpredictable labelling efficiency. In contrast, synthetic dyes have a much higher photon yield (brighter), are more robust against photobleaching and have a higher quantum efficiency compared to fluorescent proteins. Synthetic dyes can also be covalently bound to proteins and antibodies of interest using linkers and chemical modifications (e.g., click chemistry, ligand-binding enzymes (SNAP-tag [34, 35, 41]) or NHS-ester conjugation). Furthermore, highly specific toxins like phalloidin conjugated with fluorescent dyes are used to stain the actin cytoskeleton with high affinity. Labels always add distance between the molecule of interest and the fluorophore (which is mainly imaged). For SMLM these short distances can introduce measurable distortions (see Fig 2., antibody ~15 nm, fluorescent proteins ~3 nm, SNAP-tag ~3 nm, phalloidin & click chemistry < 1 nm) [28]. Some fluorescent labels are also membrane permeable, which eliminates the requirement of permeabilization and allows for live cell experiments. Silicon rhodamine and Janelia Fluor® dyes were reported to have excellent membrane permeability and are well-suited for live cell experiments [42, 43].

1.5 SMLM analysis

The most important part of SMLM is the accurate localization of single molecule signals in noisy images (Fig 3). Computer vision is typically utilized to identify single-molecule signals. Background signals, autofluorescence or noise induced by scientific cameras influence image quality and complicate the identification task. Therefore, background removal and filtering are important steps in SMLM analysis. Background estimation and removal of background structures can be archived by temporal median filtering [44], wavelet decomposition [45] or the rolling ball algorithm [46]. Furthermore, deep neuronal networks (DNN) were applied to reconstruct images containing only the background without the noise and single molecule signal of arbitrary PSFs. By subtraction the background can be completely removed [47].
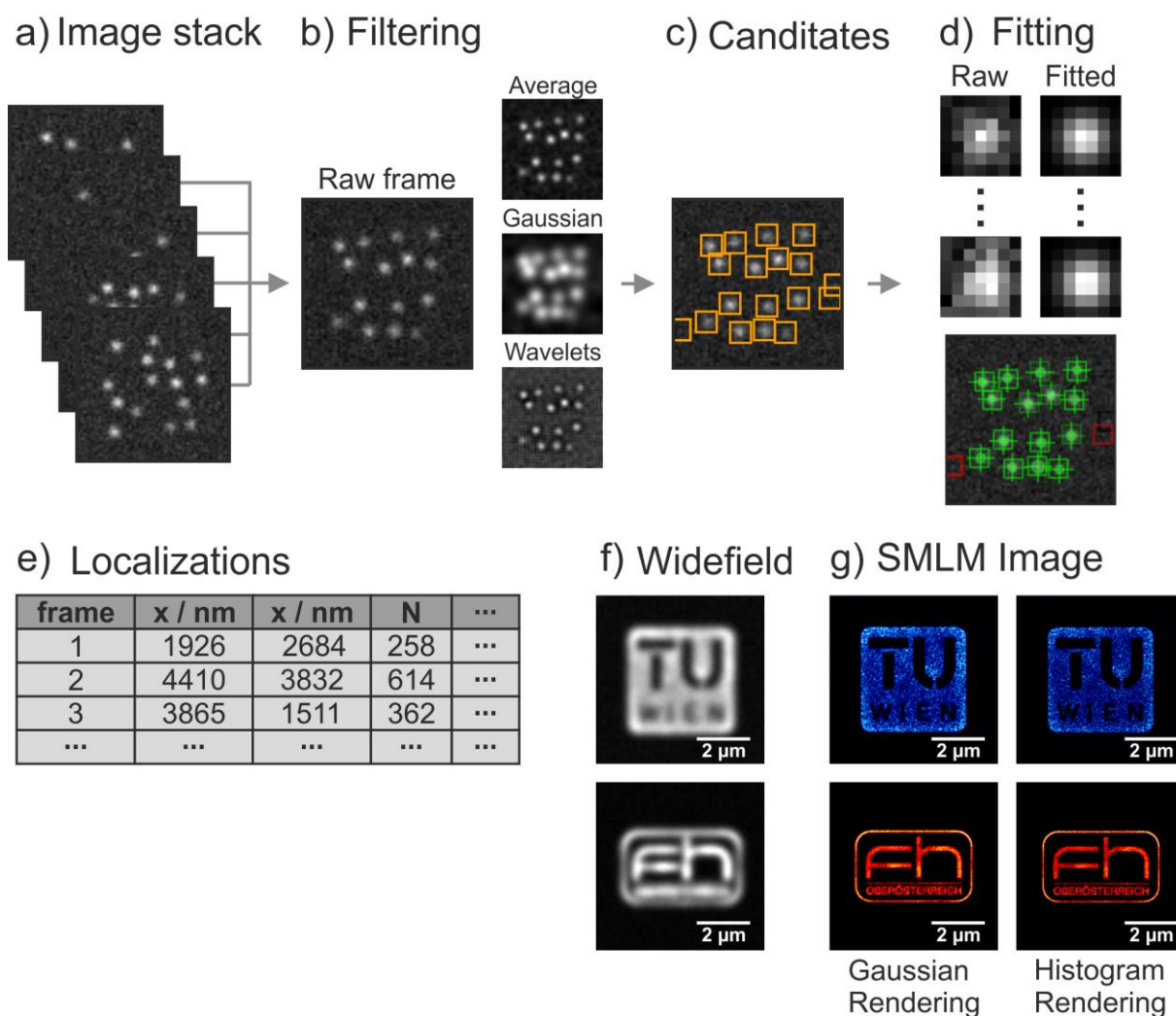
SMLM analysis

Figure 3: Sequence of SMLM analysis on the example of simulated data. a) during the SMLM analysis a sequence of several thousand of acquired frames is analysed. b) to find candidates within a single frame, multiple filters can help to find single molecule signals in noisy images (i.e.: average filtering, Gaussian filtering (smoothing) or wavelets). c) candidates are determined from local maxima of filtered or raw frames. For each candidates a suitable bound box around each signal is chosen for fitting. d) each candidate is then fitted with a suitable PSF model (e.g., Gaussian model) and parameters such as subpixel position, intensity and background are optimized. Fits with positions outside the bound box, negative values or extreme cost values are discarded. e) all successful fits are collected in a list containing the retrieved values. Additionally, values for the quality of the fit are calculated (positional accuracy or Cramer-Rao lower bound). f) shows the widefield image of the simulated SMLM experiment (average of all frames). g) a final SMLM image is rendered from the list of fitted single molecule signals.

Equally important is the identification of single molecule signals even under low signal-to-noise conditions. Therefore, different filters are used to enhance the contrast of signals (Fig 3b). It is important to note that these filtered images are only utilized to identify potential single molecule signals. Simple filtering is achieved by convolving the image with a 2D Gaussian function. The sigma is chosen to be as close as possible to the PSF width. However, 2D convolutions can be slow and computationally intensive. As a substitution, a windowed average filter can be applied,

which gives similar results to Gaussian filtering [48]. Wavelets have also been used for filtering. The fast "à trou" wavelet implementation uses the difference of two windowed low pass filters optimized for single molecule signals to massively enhance contrast [49].

Various algorithms have been developed to identify single-molecule signal candidates from these filtered images (Fig 3c). One commonly used algorithm is non-maximum suppression (NMS) [50]. In this algorithm, the image is scanned pixel by pixel, and if the pixel intensity is not the maximum intensity value within a defined area, the signal is rejected. Otherwise, the pixel intensity and location are added to a list of candidates. NMS is a very fast and computationally inexpensive algorithm but is not well suited for high-density signals and PSFs with multiple maxima (e.g., tetrapod PSF). Another method is template matching, which searches for maxima after a 2D convolution with the PSF [51]. This algorithm allows for the identification of arbitrary PSFs but is computationally much more intensive and becomes even slower with 3D SMLM images.

Subsequently, the accurate parameters for each single molecule signal in the list of candidates must be determined (Fig 3d). Subregions around the candidate positions are cropped and used to fit a suitable PSF model. After fitting, unsuitable or wrongly identified signals must be discarded in a judgment step. In SMLM, Gaussian models are commonly applied due to their simplicity. Since PSF models are typically nonlinear functions, parameters have to be iteratively retrieved, to minimize a cost function (i.e., least-squares; the squared difference between model and observed data). Full nonlinear least-squares fits replaced the inaccurate methods previously applied in SMLM (e.g. Gaussian mask fitting [52]). Gradient-descent [53], Levenberg-Marquardt (LM) [54] or trust-region methods [55] are usually applied for nonlinear optimization. However, studies suggested that the least-square method isn't the best choice for fitting data with Poisson statistics [56]. Maximum-likelihood estimation (MLE) for SMLM incorporates the Poisson process, which provides a better approximation of single molecule signals. Usually, MLE requires maximizing a cost function with the second derivative of the PSF model, which is very computationally intensive. A solution to this problem has been proposed by combining MLE with the LM algorithms [57], which doesn't require the second derivatives. A measure for the highest possible localization precision archivable by an unbiased estimator is the Cramer-Rao lower bound (CRLB, calculated from the diagonal of the Fisher information matrix) [58]. Studies suggest that MLE can archive the CRLB if the PSF approximation model is accurate [59].

One possibility to find an accurate PSF model that accounts for the aberrations of the optical system is phase retrieval [51, 60, 61]. This involves modelling arbitrary PSFs from the pupil function, which is retrieved during calibration prior to the experiment. ZOLA 3D expands on this model to include also refractive index mismatch correction and MLE fitting [51]. Nevertheless, phase-retrieved PSF models are very computationally intensive due to the extensive use of Fourier transforms. Moreover, these models do not account for the rotation of fluorophores (dipole PSF broadening), which often results in a PSF with sharper structures (steeper intensity flank) compared to the measured PSF. This is usually corrected by convolution with an empirical rescaling function (i.e. 2D Gaussian filter) [60]. Y. Li et al. proposed splines for the interpolation of arbitrary PSFs. Here, 3D stacks of single molecule singles at multiple axial positions are fitted using cubic splines with 64 coefficients in each voxel. These coefficients accurately represent the experimental PSF and are used in conjunction with MLE-LM fitting to accurately localize single molecule signals. An open-source software of this algorithm is available as SMAP [62]. Experimental and simulated data confirmed that both software packages ZOLA 3D and SMAP achieve the highest possible localization precision (CRLB) [63].

In addition to CRLB estimation of the fit quality, other formulas have been developed to calculate the positional or localization accuracy of single molecule fits. Mortenson (based on the work of Thompson [52]) published a formula for localization accuracy of single molecule signals using least-squares fitting [64]:

$$PA_{x,y} = \sqrt{\frac{\sigma^2 + \sigma^2/12}{N}\left(\frac{16}{9} + 4\tau\right)}$$

Where σ is the fitted width, N is the number of collected photons, b is background photons per pixel, a is the pixel size and $\tau = 2\pi b(\sigma^2 + \sigma^2/12)/(N \cdot a^2)$. This formula can be further extended to calculate the axial positional accuracy for astigmatism [65]:

$$PA_z = \frac{l^2 + d^2}{2l\sqrt{N}}\sqrt{1 + 8\tau + \sqrt{\frac{9\tau}{1 + 4\tau}}}$$

Where l is a measure of the focal depth and d is the distance between the minima of the calibration curve.

Still, estimators are expected to analyse non-overlapping single molecule signals at low densities to achieve the best possible localization accuracy. Advanced algorithms originating from astronomy (DAOPHOT [66]) can identify and fit dense single molecule signals. Theoretically, the optimal solution for dense SMLM would be to fit all signals within an image at once. However, this approach is extremely computationally demanding and usually leads to overfits [67]. Therefore, DAOSTORM [67, 68] and WTM [69] use an iterative process in which successfully fitted single molecule signals are subtracted from the original image. Smaller regions with overlapping PSFs are then fitted all at once. This procedure is repeated until no more single molecule signals can be identified [67–69].

Recently emerging new fitting algorithms use deep learning and DNNs to solve both the high-density and accurate PSF model problem. Furthermore, no filtering or background removal is required as all these tasks are incorporated by the DNN. Typically, U-Nets [70] or convolution layers with fully connected outputs are applied to one or more full input frames [71–73]. The DNN then generates either a single output image or a discrete output list containing the positions of detected single molecule signals. The network is trained with simulated data and applied to each image of the experiment. The results of the individual frames are then combined into a single super-resolution image. However, using this method, subpixel positions usually used for post-processing and quantitative data analysis are lost. DECODE [74] extends this method by providing additional output images for subpixel positions and localization accuracies in 3D. Consequently, single molecule data retrieved by DECODE can be used for post-processing.

In a final step, super-resolved images are reconstructed from the list of fitted single molecule signals (Fig 3e). The most truthful reconstruction of super-resolved images is to render each single molecule signal as a 2D symmetrical Gaussian function with the calculated localization accuracy as sigma (Fig 3g). Furthermore, a 2D histogram of the fitted position data can be used for super-resolution rendering (Fig 3g). For 3D SMLM experiments, axial information must be encoded into 2D images, which usually involve representing axial positions with false colours. Images are reconstructed using alpha blending, where the axial position is represented by a colour value and the lateral position is encoded using 2D Gaussian functions as the alpha channel. In addition, 3D SMLM data can be rendered as a 3D volume using anisotropic Gaussian functions (lateral and axial localization accuracy for sigma). GPU (graphics processing unit) accelerated real-time rendering of 3D signals can also be archived using the

ViSP software tool, which provides additional functionality for cluster analysis and surface reconstruction [75].

Furthermore, DNNs were proposed to produce augmented fluorescence images from bright-field images. Cheng et al. proposed a DNN that uses images from reflectance-mode microscopy (backscattered signals that provide higher spatial frequencies [76]) to produce label-free augmented fluorescence images of subcellular structures such as the Golgi complex, DNA, endosomes, and the actin cytoskeleton [77]. This method could allow for SMLM image generation from bright-field images. Similar methods that speed-up SMLM by artificial neural networks were already proposed. SMLM images can be reconstructed from fewer frames without altering spatial resolution or density. The artificial neural network learned to fill in missing localization by exploitation of structural redundancies of biological images (e.g. actin filaments, microtubes, mitochondria or the nuclear pore complex) [78].

1.6 Application of SMLM in biology

Over the past two decades, SMLM has enabled imaging of biological structures down to the nanometre scale. However, imaging of subcellular structures such as actin filaments of the cytoskeleton with a diameter of about 7 nm remains challenging. Several extensions of SMLM have been proposed to image these fine structures of the actin cytoskeleton. K. Xu et al. used a dual-object microscope in combination with 3D STORM to obtain sub 10 nm lateral resolution and resolved individual actin filaments [79]. Furthermore, refractive index matching by adding glycerol allows for the collection of more photons and therefore increased the position accuracy of detected fluorophores. Buffers containing up to 80% glycerol were reported [80, 81]. These buffers can be further improved by using oxygen scavenger systems that reduce photobleaching and triplet state times [81]. In addition, special staining buffers (containing MES, KCl, MgCl2, EGTA and sucrose) can increase the levelling degree and stabilize the cytoskeleton during fixation [82].

Spatial sample drift during the long acquisition times is a common problem in SMLM. Drift adds a blurring effect to SMLM images and is often unavoidable even in temperature and vibrational-controlled environments. One possibility to track and measure sample drift is to use fiducial markers (e.g. fluorescent beads, gold nanoparticles, Tetraspeck™ microspheres or quantum dots) [83]. The calculated drift of the fiducial markers can then be subtracted from the

SMLM image. Furthermore, marker-less drift correction can be applied to SMLM images with distinct or periodic structures (e.g. cytoskeleton). Thereby, the drift is calculated by grouping signals from multiple frames and calculated drift based on the shift determined in cross-correlation images [84]. An improved algorithm similar to cross-correlation uses Parzen-window density estimation [85] and utilizes the positional data and localization accuracies of single molecule signals to directly estimate the drift [81].

SMLM experiments typically require 5 to 10 minutes to acquire the necessary image frames for a single super-resolved image. Due to long acquisition times, constant surveillance of the experiment by an operator is required. This can be very time-consuming for the operator, especially for biological experiments that often require several recordings for statistical evaluation. One remedy can be the automation of such SMLM experiments. Often operators manually increase the power of 405 nm reactivation laser pulses to counteract bleached fluorophores and to keep a constant number of active fluorophores. This can be automated by real-time SMLM analysis with a feedback loop that controls the reactivation laser [63, 86, 87].

An inherent feature of SMLM is the ability to further analyse single molecule data in a post-processing step. Quantitative analyses of SMLM data allow for the calculation of densities, spatial distributions and to approximate the signal count in certain areas. Clustering is used to group data points into subsets with similar distributions. A major challenge in biology is the determination of nanoscale positions and quantification of molecular clusters in a cellular and subcellular structure. Usually, positional data calculated from the SMLM experiment is used for clustering in the nanoscale domain [88]. For example, clustering has been applied to find underlying membrane structures in stained SMLM membrane samples [89] or study synaptic signalling [90]. A wide range of algorithms has been developed to identify shapes, densities, and orientations of distinct clusters in SMLM localizations. In addition to the typically used density-based algorithms such as DBSCAN [91] and tessellation [92], optimization-based methods like K-Means enable the iterative partitioning of signals into clusters with the closest means [93]. Furthermore, based on the computed clusters, segmentation of biological structures with minimal backgrounds is possible. These determined clusters can be further used to study their morphology. Methods for the extraction of structures from SMLM data such as microtubules [92, 94] and mitochondria networks (own paper: *Platelet activation studies via 3D localization microscopy and machine learning on a blood vessel chip) have been proposed. Similar publications showed that the morphology of mitochondrial networks can be further

analysed to quantify the health of individual cells using machine learning algorithms [95].

Equally important for biological questions is the imaging of multiple protein targets. Two or more colours were successfully used for SMLM. In one of the first multi-colour SMLM publications (2008), sequential imaging of different coloured fluorophores was utilized to study the spatial relationship between mitochondria and microtubules [80]. In this context, two-colour STORM utilizes an alternating sequence of two different activation lasers and an imaging laser between the activation pulses. Another publication demonstrated simultaneous two-colour SMLM by using a beam splitter (e.g., OptoSplit from Cairn Research) that projects the colour channels onto two non-overlapping areas of the camera chip [96]. More proteins can be sequentially imaged using multiplexed DNA-PAINT. First, different molecular targets are labelled simultaneously using different DNA docking strands. Buffers containing the complementary DNA strands conjugated with a fluorescent dye are successively imaged and exchanged until each molecular target is imaged [97]. Due to the multiplex nature of this method, the same fluorescent dye can be used for each target.

2 Description of contributed papers

During my Batchelor's and Master's thesis, I developed the 3D-STORM-Tools software for 2D and 3D SMLM analysis and QSdtControl, a software for acquisition and laser control. My developed 3D astigmatism analysis software reached the 6th place, during the 2016 SMLM challenge among international participants [98]. In this thesis, I extensively utilized and improved both software packages. I demonstrated that SMLM and advanced software tools can be applied to biological applications to extract the most amount of data possible. Real-time analysis was enabled by the application of software optimization methods such as multi-threading, single instruction, multiple data (SIMD) and GPU acceleration. I also used machine and deep learning to extract more data from experiments and segment cells and subcellular structures.

2.1 Localization Microscopy of Actin Cytoskeleton in Human Platelets

S. Mayr, F. Hauser, A. Peterbauer, A. Tauscher, C. Naderer, M. Axmann, B. Plochberger, and J. Jacak

Localization Microscopy of Actin Cytoskeleton in Human Platelets

Int. J. Mol. Sci. **19**(4), 1150 (2018)

In Mayr e. al. "Localization Microscopy of Actin Cytoskeleton in Human Platelets" [81], we applied 2D SMLM imaging to observe the actin cytoskeleton of platelets at different morphological states in 2D. Platelets are small blood cells that are primarily responsible for wound closure. During activation, their actin cytoskeleton is reorganized, and platelets undergo multiple states. The three major states were imaged and filopodia formation was studied. We developed a new medium composition to image rhodamine class fluorophores (Alexa 488) with dSTORM. In this contribution, I have applied my SMLM software to image and reconstruct the actin cytoskeleton of platelets. Thereby, improvements to the imaging buffer using 80% glycerol and an oxygen-scavenging system in combination with marker-less drift correction allowed imaging of single molecule signals with a localization accuracy of 12 nm. Furthermore, I calculated for the first time the width of the platelet's filopodium from reconstructed dSTORM image.

2.2 Statistical analysis of 3D localisation microscopy images for quantification of membrane protein distributions in a platelet clot model

S. Mayr, F. Hauser, S. Puthukodan, M. Axmann, J. Göhring, and J. Jacak

Statistical analysis of 3D localisation microscopy images for quantification of membrane protein distributions in a platelet clot model

PLOS Comput. Biol. **16**(6), e1007902 (2020)

In Mayr et al. "Statistical analysis of 3D localisation microscopy images for quantification of membrane protein distributions in a platelet clot model" [99], we applied hierarchical clustering and feature extraction on a platelet clot model. The developed platform 2CALM allows for the determination of the similarity of two samples of 3D SMLM images. A trained DNN allowed for the automated determination of similarity or dissimilarity based on the calculated features from both samples. We demonstrated the biological applicability of 2CALM on the distribution of CD41 and CD62P in an artificial platelet clot. 3D dSTORM images of CD41 and CD62P were analysed using my 3D-STORM-Tools software. I reimplemented the necessary marker-less drift correction algorithm for 3D into my 3D-STORM-Tools project to ensure the best possible image qualities. I was also involved in the acquisition and generation of 3D SMLM images. Results showed that CD41 and CD62P have different distributions at the nanoscale level.

2.3 Real-Time 3D Single-Molecule Localization Microscopy Analysis Using Lookup Tables

F. Hauser and J. Jacak,

Real-Time 3D Single-Molecule Localization Microscopy Analysis Using Lookup Tables

Biomed. Opt. Express **12**(8), 4955–4968 (2021)

In Hauser et al. "Real-Time 3D Single-Molecule Localization Microscopy Analysis Using Lookup Tables" [87], I developed a fitting algorithm using a hybrid least-square approach with template images. My real-time 3D SMLM algorithm is capable of localizing ~120 single molecule signals in ~2.6 ms on a single CPU (central processing unit) thread. I evaluated the performance and accuracy of the approach, resulting in a balance between archivable precision, speed, and resource allocation. This algorithm was also implemented into the 3D SMLM setup

control software QSdtControl. Typical acquisition times of 40 ms per frame allowed additional tasks to be performed based on the real-time SMLM data, such as rendering or controlling an activation laser. Simulations and further tests on the 3D SMLM challenge dataset demonstrated the capabilities of the algorithm I developed. I also tested this method on primary human endothelial cells and human platelets to image the 3D actin cytoskeleton.

2.4 Platelet activation studies via 3D localization microscopy and machine learning on a blood vessel chip

F. Hauser, C. Naderer, S. Milic, E. Priglinger, B. Buchroithner, A. Peterbauer, M.B. Fischer, H. Redl, and J. Jacak

Platelet activation studies via 3D localization microscopy and machine learning on a blood vessel chip

Under revision (2022*)

In Hauser et al. "Platelet activation studies via 3D localization microscopy and machine learning on a blood vessel chip" (under revision), I have developed a platform to analyse platelet activation on an endothelial cell monolayer within a microfluidic chip. I custom built a microfluidic chip that allows for imaging with a high-NA objective lens. The microfluidic chip was optimized for sterile cultivation of primary human endothelial cells. An automated pump enabled optimal growth under flow conditions. I trained a convolutional deep neuronal network (U-Net) to automatically segment cell nuclei from phase-contrast images for counting. This allowed us to determine the cell density, confluency and optimal timepoint for experiments (> 500 cells/mm²). The microfluidic chip, which models the inner endothelial layer of small blood vessels, was then incubated under flow conditions with human platelets. Single selected endothelial cells within the microfluidic chip were laser treated using femtosecond laser pulses (1600 W/μm³). Two-colour 3D SMLM of CD62P (platelet activation marker) and mitochondria was performed simultaneously on these samples using a beam-splitter (Cairn OptoSplit II). I added support for two-colour 3D SMLM to my 3D-STORM-Tools software. I also implemented a machine learning-based method for the removal of residual fluorescent bleed-through. 3D SMLM mitochondria data was segmented, and further parameters were extracted. Machine learning-assisted classification of mitochondria segments allowed us to identify stressed-prone, stress-resistant, and laser-treated endothelial cells. Platelet activation on or

between the endothelial cell layer was correlated with the classified cellular types. Results showed that platelets mostly activated in the proximity of stressed-prone endothelial cells, whereas no activation at all was observed near laser-treated endothelial cells. Statistical analysis of platelet volumes also revealed higher values under flow conditions compared with statically incubated endothelial cells and platelets.

3 List of contributed papers

In this chapter all important papers written for my thesis are listed in the same typeset as used by the publishing journal.

Communication

Localization Microscopy of Actin Cytoskeleton in Human Platelets

Sandra Mayr [1],* iD **, Fabian Hauser [1], Anja Peterbauer [2], Andreas Tauscher [1], Christoph Naderer [1], Markus Axmann [3], Birgit Plochberger [1] and Jaroslaw Jacak [1]**

[1] School of Medical Engineering and Applied Social Sciences, University of Applied Sciences Upper Austria, Garnisonstr. 21, 4020 Linz, Austria; fabian.hauser@fh-linz.at (F.H.); andreas.tauscher@fh-linz.at (A.T.); christoph.naderer@students.fh-linz.at (C.N.); birgit.plochberger@fh-linz.at (B.P.); jaroslaw.jacak@fh-linz.at (J.J.)

[2] Red Cross Blood Transfusion Service for Upper Austria, Krankenhausstr. 7, 4017 Linz, Austria; anja.peterbauer@o.roteskreuz.at

[3] Center for Pathobiochemistry and Genetics, Institute of Medical Chemistry and Pathobiochemistry, Medical University of Vienna, 1090 Vienna, Austria; markus.axmann@meduniwien.ac.at

* Correspondence: sandra.mayr@fh-linz.at; Tel.: +43-50804-56017

check for
updates

Abstract: Here, we measure the actin cytoskeleton arrangement of different morphological states of human platelets using a new protocol for photo-switching of rhodamine class fluorophores. A new medium composition was established for imaging the cytoskeleton using Alexa Fluor 488 conjugated to phalloidin. Morphological states of platelets bound to a glass substrate are visualized and quantified by two-dimensional localization microscopy at nanoscopic resolution. Marker-less drift correction yields localization of individual Alexa 488 conjugated to phalloidin with a positional accuracy of 12 nm.

1. Introduction

Platelets are the smallest blood cells in circulation. Upon activation—usually triggered by binding of platelets to the extracellular matrix of damaged vessel walls—reorganization of the actin cytoskeleton takes place, introducing platelet shape change. The actin cytoskeleton of platelets is described in literature as a three-dimensional, sparse, and fibrous network without apparently long actin fibers. Upon cell attachment to a surface (round-shaped cells), the actin filaments are depolymerized into shorter filaments. During spreading, new filaments are assembled—the amount of F-Actin in the activated state, however, is low (only approximately two-thirds in comparison to the resting state) [1]. Thus, characterization of the actin cytoskeleton ultrastructure within these 2–5 μm-sized cells proves arduous. In contrast to conventional fluorescence microscopy and the inherent resolution limit [2,3], localization microscopy provides insight into the distribution of specific proteins at the nanoscale and creates snapshots of cellular dynamics within single cells [4–10]. Thus, application of the super-resolution technique dSTORM (direct stochastic optical reconstruction microscopy) is the method of choice for these small cells [11]. The most common used fluorophore for dSTORM is the cyanine Alexa Fluor 647. The number of protocols for the application of rhodamine class fluorophores, however, is limited [12–15] and localization microscopy with dyes like Alexa Fluor 488 remains a constant challenge and relies on high-power lasers. For illumination, we used a low cost UV laser, which allowed for fast image acquisition. Fast illumination can reduce the drift, hence less correction is required.

Here, we apply dSTORM in order to display the actin cytoskeleton of platelet shape changes for the first time. For imaging we use the cyanine derivative Alexa Fluor 647 and the rhodamine class dye Alexa Fluor 488. We introduce an additional protocol for photo-switching of rhodamine derivatives like Alexa Fluor 488 in order to have an additional color channel available for labeling. The super-resolved images of platelet cytoskeleton allow quantitative characterization of the actin network, such as the width of the filopodia and of the actin accumulated at the periphery of spread platelets. Quantitatively comparable results from both color channels were obtained.

2. Results

2.1. Platelet Attachment Protocol

To observe morphological states upon platelet shape change, we incubated the cells in cell culture medium on plain glass slides as described in literature [16–19]. Figure 1 represents typical, distinguishable platelet morphological states, visualized using differential interference contrast (DIC) microscopy. The three described states correspond to typical morphological states of platelet activation [16]. Platelet activation is a multi-factorial process that involves shape change, cell adhesion, degranulation, and ultimately clot formation [20]. The (at least partial) activation of the platelets observed here was confirmed by staining for the standard activation marker CD62p (see Supplementary Figure S1). Here we talk, however, about morphological states of platelet shape change rather than platelet activation states since the complex and multifactorial process of platelet activation was not investigated further.
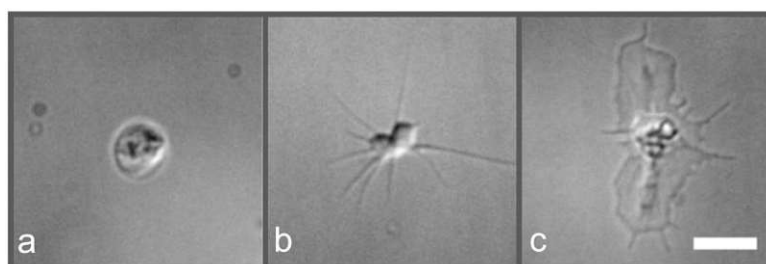
Figure 1. DIC images of human platelets at three different morphological states upon platelet shape change (cell culture medium on plain glass support). Upon glass contact, platelets adopt a round shape (**a**) that facilitates cell adhesion. Subsequently, filopodia form a spindle-like morphology (**b**). Lamellipodia fill the area between individual filopodia, and platelets spread further forming a so-called "fried-egg" morphology (**c**) [1,16]. Scale bar 5 μm.

Upon incubation of cells on a glass substrate, discoid platelets adopt a round shape (Figure 1a) facilitating cell adhesion, analogous to the rolling mechanism of leukocytes on activated endothelial cells of blood vessels [1]. Subsequently, highly dynamic and actin-rich cell protrusions (filopodia) serve as sensors, probing the platelet's environment [21] and forming a spindle-like morphology (Figure 1b). Upon occurrence of lamellipodia that fill the intermediate area between individual filopodia for cell motility, cells spread further (adopting a "fried-egg" shape; Figure 1c).

2.2. Nanoscopic Localization of the Actin Cytoskeleton in Platelets

In this study, we present a new protocol (see Section 4) for photo-switching of the rhodamine derivative Alexa Fluor 488 (Figure 2a–c). We visualized the actin cytoskeleton of platelets that undergo morphological shape changes at the single-cell level using nanoscopic localization of fluorescently labeled phalloidins. The three exemplarily shown states correspond to typical morphological states of platelet shape change [16]. Figure 2a–c show similar morphological states of platelets labeled with Alexa Fluor 488 phalloidin (additional images in Supplementary Figure S2). Figure 2a shows the cytoskeleton of a round-shaped platelet in an early state of adhesion. Figure 2b depicts a platelet in

a spindle-like morphology with filopodia and Figure 2c displays a 'fried-egg'-shaped cell with actin accumulated in the central granulomere and at the periphery of the cell.

The areas with higher local phalloidin densities in the peripheral region are of unknown origin (fluorophore induced artifact or biological origin). However, they are frequently observed mainly in "fried-egg" shaped platelets. For imaging of the rhodamine derivative Alexa Fluor 488, a new, optimized protocol was used. To ensure efficient blinking of the rhodamine dye Alexa 488 a special medium composition was applied: photo-switching is achieved with the reducing agent tris(2-carboxyethyl)phosphine (TCEP), the oxidizing agent methylviologen (MV) and β-mercaptoethylamine in a 80% glycerine solution containing 5% glucose. In this environment, the fluorophore is excited at 488 nm for 20 ms at a frame rate of 25 images/s. The fluorophore in the triplet state is reduced by TCEP and is brought back to the singlet ground state by interaction with MV and illumination with a 405 nm laser for 20 ms using a low laser power (intensity = 100 W/cm^2). The dSTORM images were reconstructed from 15,000 frames. Alexa Fluor 488-labeled phalloidin molecules correspond to the blue colored localizations within the cells (Figure 2a–c); brighter areas correspond to a higher density of localized fluorophores. On average, we detected 740 signals/μm^2 within a cell (n = 3 cells).
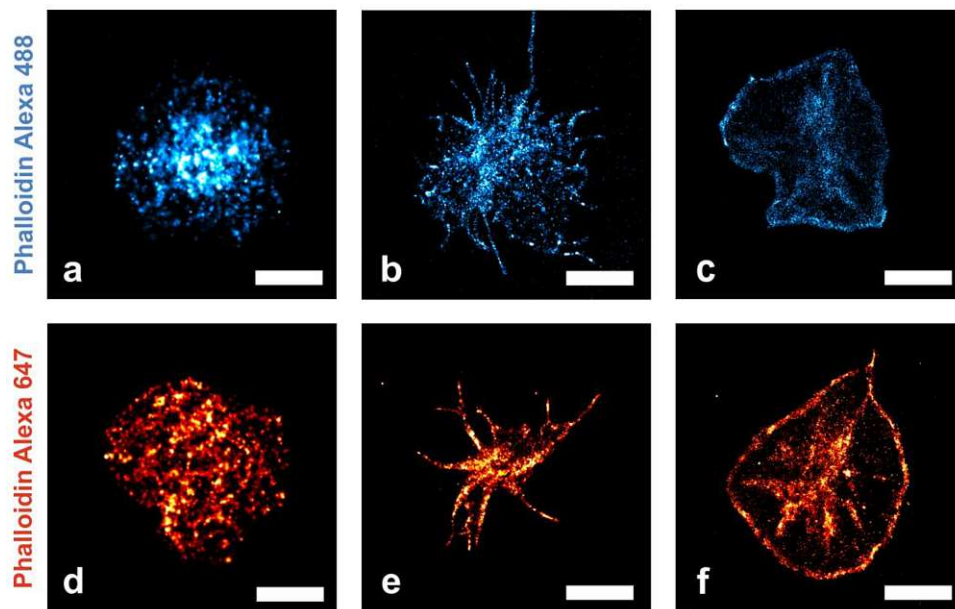

Figure 2. Reconstructed fluorescence microscopy images (dSTORM) of human platelets at three different morphological states (cell culture medium on plain glass support), stained with phalloidin Alexa Fluor 488 (top row) or phalloidin Alexa Fluor 647 (bottom row). F-actin molecules bound by fluorescently labeled phalloidin are represented by the red and blue colored localizations within the cells, respectively. Brighter areas are caused by a higher density of localized fluorophores. As platelets start to adhere to the glass support, an early, round-shaped appearance (**a**,**d**) transforms into a spindle-like morphology (**b**,**e**) and subsequently yields a "fried-egg" shape (**c**,**f**). The central granulomere and accumulated actin in the peripheral cell region in the 'fried-egg' morphology is clearly visible (Figure 2c,f) [1]. Scale bar for (**a**,**d**) 1 μm and for (**b**,**c**,**e**,**f**) 3 μm.

For verification, the platelets' cytoskeleton was labeled with a second fluorophore conjugated to phalloidin (Figure 2d–f). The three described states correspond to typical morphological states of platelets [16]. Image acquisition was performed in a medium containing beta-mercaptoethylamine (MEA) and glycerine. The samples were irradiated at 647 nm for 20 ms. Between acquisition of individual images, the sample was illuminated with a 405 nm laser light for 10 ms. The dSTORM images were reconstructed from 15,000 frames. The localization events determined from Alexa Fluor

647 blinking are shown in red. Individual F-actin molecules bound by phalloidin conjugated to the commonly used cyanine dye Alexa Fluor 647 were localized with a 12 nm positional accuracy after drift correction for compensation of the mechanical sample movement. On average, we detected 3500 signals/μm² within a cell (*n* = 3 cells).

The blinking behavior of Alexa Fluor 488 was compared to Alexa Fluor 647: Fewer signals were detected for the Alexa Fluor 488 labeled cells (740 signals/μm² as compared to 3500 signals/μm² for Alexa Fluor 647). However, the blinking characteristics are similar: Alexa Fluor 488 showed on average 9 ± 2 blinking events per 15,000 frames (SD = 0.1; *n* = 45 analyzed image sequences) and Alexa Fluor 647 showed 10 ± 3 blinking events (SD = 0.1; *n* = 45 analyzed image sequences).

In contrast to conventional fluorescence microscopy, localization microscopy allows quantitative visualization of diffraction limited actin cytoskeleton substructures. The width of the peripheral actin network (i.e., the actin network at the edge of the 'fried-egg' shape as seen in Figure 2c,f) varies from 140 nm to 565 nm for Phalloidin Alexa 488 and from 200 nm to 580 nm for Phalloidin Alexa 647, respectively. Likewise, the width of filopodia was determined: Figure 3a shows the image of the actin cytoskeleton recorded with diffraction limited fluorescence microscopy; whereas Figure 3d depicts the cytoskeleton of the same cell reconstructed by localization microscopy. In Figure 3b, the filopodium from the boxed region in 3a is depicted (likewise the same filopodium at nanoscale resolution, however, seen in Figure 3e from the boxed region in Figure 3d). The width of a single filopodium (Figure 3b,e) was quantified by fitting the cross section profile with a Gaussian function. Figure 3c shows the profile of a filopodium whose width was determined (in the diffraction limited image a FWHM = 675 nm; for Phalloidin Alexa 647).
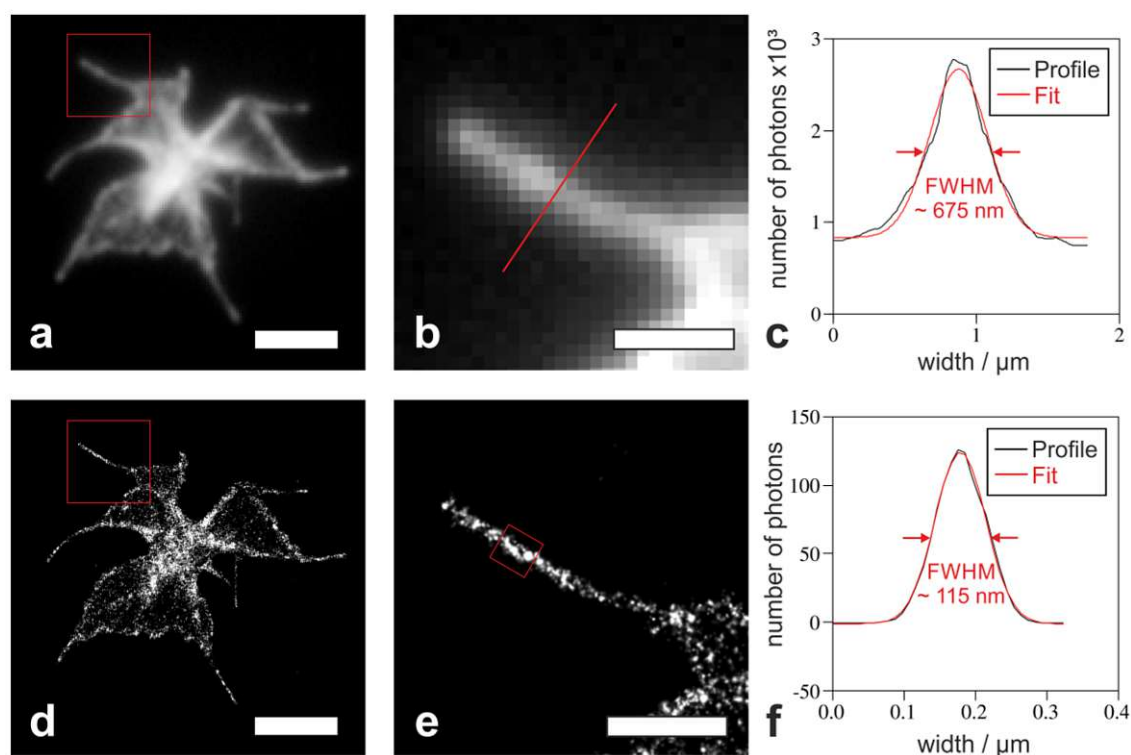
Figure 3. Comparison of a conventional fluorescence and a super-resolution image of the actin cytoskeleton of a platelet with a spindle-like morphology labeled with Phalloidin Alexa 647 (**a,d**). Close-up of the region of interest from the image in (**a,d**) shows a single filopodium (**b,e**). The intensity profile of the filopodium cross section from the boxed region (**b,e**) has been fitted with a Gaussian function (**c,f**). From the fit a FWHM of 675 nm (**c**) or of 115 nm (**f**) has been determined for the filopodium width. Scale bar for (**a,d**) 3 μm and for (**b,e**) 1 μm.

The width of the filopodium was determined from the reconstructed dSTORM image (Figure 3f): A FWHM of 115 ± 9 nm was measured for Phalloidin Alexa 647 and 106 ± 3 nm for Phalloidin Alexa 488, respectively.

Regardless of the used label, the same morphological characteristics (width of filopodia and peripheral actin network) at the same resolution (12 nm for both fluorophores) have been determined.

3. Discussion and Conclusions

In summary, we showed that our optimized protocol allows for recording qualitatively comparable images with Alexa Fluor 488 (compared to commonly used Alexa Fluor 647) labeled actin filaments. We showed for the first time the actin cytoskeleton of three different platelet morphological states resolved at a resolution beyond the diffraction limit. In contrast to the dSTORM images, the conventional fluorescence microscopy images of filopodia appeared as diffraction limited structures: Only the dSTORM images allowed us to determine the size distribution of platelets' filopodia width. A detailed quantification revealed an average filopodium width of 115 ± 9 nm (for Phalloidin Alexa 647) and 106 ± 3 nm (for Phalloidin Alexa 488), respectively. Apart from a report exclusively showing a filopodium width of a neuroblastoma cell [22] this is the first quantitative description of the width of filopodia and the very first on filopodia in human platelets.

Photo-switching of the rhodamine dye Alexa Fluor 488 is achieved in a special medium composed of the reducing agent TCEP, the oxidizing agent MV and glycerine as well as an optimized illumination protocol. Using this protocol allows for implementation of standard (i.e., low cost) diode UV laser sources in contrast to usually applied high-end laser sources. In addition, the applied marker-less drift correction enables acquisition of a sequence with a higher number of frames, thereby compensating the reduced number of signals/μm^2 in the blue channel. The applicability of the new medium for rhodamine class dyes is shown with Alexa Fluor 555 (Supplementary Video S1).

The medium applied here can be mixed with additives like oxygen scavengers to improve photo-switching properties of the dye [15]. A medium with higher refractive index (glycerine, $n = 1.45$) [23] compared to aqueous solutions allows us to detect more photons from a single fluorophore and a more precise position determination. Such high positional accuracy as obtained by our protocol allows for precise monitoring of distinct morphological changes. For filopodia width determination, our obtained 12 nm resolution is completely sufficient. Images of filopodia reconstructed with a lower resolution verify that even a resolution of ~20 nm is satisfactory (Supplementary Figure S3).

The use of different fluorophores for dSTORM, as demonstrated by qualitative comparison of the platelet actin cytoskeleton stained with phalloidin Alexa Fluor 647 as well as phalloidin Alexa Fluor 488, offers flexibility for multi-color imaging in the future and can be applied for any desired cell (Supplementary Figure S4).

4. Materials and Methods

4.1. Human Platelet Concentrates

Single donor platelet concentrates were provided by the Red Cross Blood Transfusion Service (Linz, Upper Austria, Austria). Platelet concentrates were prepared by apheresis with an automated cell separator (Trima Accel Automated Blood Collection System, TerumoBCT, Lakewood, CA, USA) during routine thrombophoresy: The platelets were separated from whole blood by centrifugation and diluted in 35% plasma, 65% platelet additive solution SSP+ (Macopharma, Mouvaux, France), and ACD-A anticoagulant (Haemonetics® anticoagulant citrate dextrose solution, Haemonetics®, Braintree, MA, USA) during transfer into Trima Accel storage bags. Two milliliters of the platelet concentrate (typically containing 1×10^6 platelets/μL) were transferred into a new storage bag and immediately transported to the laboratory. Transportation within a polystyrene box should minimize temperature variations. Platelets were used for experiments within 24 h after preparation and meanwhile stored under constant agitation in a climatic chamber that was tempered to 22 °C.

4.2. Statement on the Use of Human Platelet Concentrate Samples

All human blood samples were collected during routine thrombophoresy in accordance with the strict policies of the Red Cross Transfusion Service, Linz. All blood donors signed their informed consents that residual blood material can be used for research and development purposes. All experimental protocols were approved by and carried out in collaboration with the Red Cross Blood Transfusion Service, Linz.

4.3. Platelet Spreading, CD62p and Actin Staining

Platelets were diluted to a final concentration of 2×10^4 cells/mL in cell culture medium (DMEM, Sigma-Aldrich, Vienna, Austria), pipetted onto a glass slide and incubated for 15 min. Non-adhered cells were washed away with PBS (phosphate-buffered saline). For DIC microscopy, cells were fixed using 4% paraformaldehyde in distilled water and imaged. The actin cytoskeleton was visualized using Alexa Fluor 647 phalloidin and Alexa Fluor 488 phalloidin (Cell Signaling Technology, Leiden, The Netherlands), respectively. Platelet actin staining was performed in Cytoskeleton buffer with sucrose (CBS) containing 10 mM MES pH 6.1, 138 mM KCl, 3 mM $MgCl_2$, 2 mM EGTA, and 0.32 M sucrose according to a protocol of Louise Cramer (MRC Laboratory for Molecular Cell Biology, UCL, London, UK) [24]. Briefly, platelets were fixed using 4% paraformaldehyde in CBS for 20 min at room temperature, permeabilized in 0.5% Triton X-100 with CBS, blocked in 10% albumin from chicken egg white (Sigma-Aldrich, Vienna, Austria) and stained for 20 min with 66 nM fluorophore conjugated to phalloidin. For CD62p labeling, fixed cells were stained with 1 μg/mL anti-CD62p antibody marked with Alexa 647 (BioLegend, San Diego, CA, USA) for 10 min.

4.4. Fluorescence Microscope

Images were acquired using a modified Olympus IX81 inverted epifluorescence microscope with an oil-immersion objective (UApo N 100x/1.49 NA, Olympus, Vienna, Austria). The sample was positioned with nanometer precision on a XYZ piezo stage (P-733.3DD, Physical Instruments) on top of a mechanical stage with a range of 1×1 cm adjusted by precision screws (TAO, JPK Instruments, Berlin, Germany). A tube-lens with an additional magnification of 1.6 was used to achieve a final imaging magnification of 160 (corresponding to a pixel size of 100 nm). Platelets were illuminated with a 642 nm laser light from a diode laser (Omicron-laserage Laserprodukte GmbH, Phoxx 642, Rodgau-Dudenhofen, Germany), a 488 nm laser light from a solid-state laser (diode-pumped, Toptica Photonics, Graefelfing, Germany), and a 405 nm laser light from a diode laser (Insaneware, Gladbeck, Germany). The signal was detected using an Andor iXonEM+ 897 (back-illuminated) EMCCD camera (16 μm pixel size). The following filter sets were used: dichroic filter (ZT405/488/561/640rpc, Chroma, Olching, Germany), emission filter (446/523/600/677 nm BrightLine quad-band band-pass filter, Semrock, Rochester, NY, USA), and an additional emission filter (HQ 700/75 M, NC209774, Chroma Technology GmbH, Olching, Germany).

4.5. Imaging Protocols

Single-molecule photo-switching of the cyanine dye Alexa Fluor 647 was performed in a 50 mM β-mercaptoethylamine in 80% glycerine containing medium (refractive index 1.45) as described by Huang and co-workers [8] and applied to the cells immediately prior to fluorescence microscopy measurements. The signal was acquired for 20 ms at 25 images/s at 1.2 kW/cm^2 excitation intensity (647 nm). During the readout, laser light from the 405 nm laser (10 ms illumination at 100 W/cm^2) was used to recover the singlet ground state. For image reconstruction, a sequence of 15,000 images was recorded.

Single-molecule photo-switching of the rhodamine dye Alexa Fluor 488 was performed in a medium composed of 2 mM tris(2-carboxyethyl)phosphine, 2 mM methylviologen, 50 mM β-mercaptoethylamine in 80% glycerine with 5% glucose in distilled water (one example of a single

molecule can be found in Supplementary Figure S5). The signal was acquired during 20 ms with 20 ms delay at 3.3 kW/cm^2 excitation intensity. Between acquisition of individual images, laser light from the 405 nm laser (10 ms illumination at 100 W/cm^2) was used to recover the singlet ground state. For image reconstruction, a sequence of 15,000 frames was recorded. The illumination protocols were performed with a custom-written acquisition software.

4.6. Image Analysis

dSTORM image series were processed and analyzed using custom-written software ('STORM Tools') in Qt/C++ and is freely available at (GITHUB https://github.com/CURTLab/STORMTools). The high-performance non-maximum suppression algorithm is adapted (with permission) from rapidSTORM [25] and used to approximate the positions of single molecules in each frame [26,27]. Each fit is performed in a window surrounding the proposed position. The point spread function (PSF) is fitted using the symmetrical two-dimensional Gaussian error function model [28] and successively approximated by the trust-region Powell dogleg algorithm [29]. The resulting parameters (x-position, y-position, integrated signal intensity, background intensity, signal width) are further used to calculate the positional accuracy [30] for the super-resolution reconstruction. One of the parameters, which is additionally needed for estimation of the positional accuracy is the background variability. Each molecule is rendered at its determined (x,y)-position using a symmetrical Gaussian intensity distribution with the calculated positional accuracy as width parameters (Supplementary Figure S6). To correct for the linear drift of the stage, each localization set has been corrected before image reconstruction (see drift correction) (Supplementary Figure S7a,c). In order to determine the lower boundary for the localization precision, the mechanical stability of the whole instrument has been determined via imaging of TetraSpeck™ beads (T-7284, 0.1 μm, Molecular Probes) over 10,000 frames within 7 min (20 ms illumination time, excitation at 647 nm). The determined radial displacement relative to the averaged signal position is 3 nm (Supplementary Figure S7b,d), which sets the technical lower limit for the positional accuracy for drift-corrected localized images.

4.7. Drift Correction

4.7.1. Drift Calculation Method

The drift correction method has been applied according to Han et al. [31]. The concept of drift correction is similar to cross correlation analysis and is based on the Parzen-window density estimation [32,33].

The method uses the determined molecule positions to judge the similarity of two signal distributions. This is conceptually straightforward and easier to operate in comparison to the cross-correlation analysis.

Assuming there are two position sets SA and SB ($p_i \in S_B, j = 1, 2, \ldots N$ and $p_j \in S_B, j = 1, 2, \ldots M$), the cost function CF(T) of drift correction T is given by

$$CF(T) = \sum_{j}^{M} \sum_{i}^{N} \frac{1}{2\pi\sigma^2} \exp\left(-||T(p_j) - p_i||^2/2\sigma^2\right)$$

where $T(\cdot)$ is a transformation function (translation and/or rotation of positions), S_B is movable, and S_A is fixed (basis set of positions). The goal is to find an $T(\cdot)$ that maximizes the CF. The simplest transformation is linear (only translation), i.e., $T(p) = p + d$, where $d = (\alpha, \beta)^T$ is shift vector, α is the drift compensation of the *x*-axis and β is the drift compensation of the *y*-axis.

4.7.2. Drift Correction Algorithm

First, the reference position set (basis set of positions) S_{basis} is initialized. Hence, the positions within frames are combined into groups S(i). Equivalent time intervals or an equivalent number of

points per group arranges the groups. By comparison if the position set S(i) to the S_{basis}, the sample drift is estimated. Hence, the drift of S(i) is compensated and the positions of S(i) is merged with S_{basis}. A quasi-newton algorithm is used to find maximum of function CF(T). Repeat the selection and drift compensation process until all the point subsets S(i) are corrected. The last reference position set in S_{basis} is the referenced corrected data.

4.8. Grouping Process

The data of individual frames are grouped in two ways:

First, the same length of time interval (the same number of frames in the frame-group). This may result in frame-groups with a small number of positions (e.g., 1 or 2 points). In this case, the translation vector d can be very long. In order to avoid that, the drift length will be limited by max-limit-drift, calculated automatically from the accuracy (sigma) of the Gaussian fitting of individual signals.

Second, the same number of points (positions) in each frame-group. In this case grouping with a fixed number of points introduce variable illumination time intervals.

4.9. Smoothing

Smoothing of the time dependent drift of points is carried out by two methods:

- Fitting 'Smoothing-Spline' with parameter 10^{-4} only in the discrete time window (sliding along the time-axis).
- Fitting method 'Smoothing-Spline' with parameter 10^{-6} for the entire time line.

Supplementary Materials: Supplementary materials can be found at http://www.mdpi.com/1422-0067/19/4/1150/s1.

Author Contributions: Anja Peterbauer provided the samples; Andreas Tauscher, Christoph Naderer, and Fabian Hauser performed the experiments; Fabian Hauser and Jaroslaw Jacak wrote the analysis software; Fabian Hauser, Sandra Mayr, Markus Axmann, and Birgit Plochberger analyzed the data; Sandra Mayr and Jaroslaw Jacak designed the experiments; Sandra Mayr, Markus Axmann, Fabian Hauser, and Jaroslaw Jacak wrote the paper.

Conflicts of Interest: The authors declare no conflict of interest. The founding sponsors had no role in the design of the study; in the collection, analyses, or interpretation of data; in the writing of the manuscript, or in the decision to publish the results.

Abbreviations

dSTORM	Direct stochastic optical reconstruction microscopy
FWHM	Full width at half maximum
DIC	Differential interference contrast
TCEP	Tris(2-carboxyethyl)phosphine
MEA	β-mercaptoethylamine
MV	Methylviologen
CBS	Cytoskeleton buffer with sucrose
ACD-A	Acid citrate dextrose and adenosine
CF	Cost function
PSF	Point spread function

References

1. Michelson, A.D. *Platelets*, 2nd ed.; Elsevier: San Diego, CA, USA, 2006.
2. Italiano, J.E.; Bergmeier, W.; Tiwari, S.; Falet, H.; Hartwig, J.H.; Hoffmeister, K.M.; André, P.; Wagner, D.D.; Shivdasani, R.A. Mechanisms and implications of platelet discoid shape. *Blood* **2003**, *101*, 4789–4796. [CrossRef] [PubMed]

3. Bender, M.; Eckly, A.; Hartwig, J.H.; Elvers, M.; Pleines, I.; Gupta, S.; Krohne, G.; Jeanclos, E.; Gohla, A.; Gurniak, C.; et al. ADF/n-cofilin-dependent actin turnover determines platelet formation and sizing. *Blood* **2010**, *116*, 1767–1775. [CrossRef] [PubMed]

4. Bach, M.; Savini, C.; Krufczik, M.; Cremer, C.; Röesl, F.; Hausmann, M. Super-resolution localization microscopy of γ-H2AX and heterochromatin after folate deficiency. *Int. J. Mol. Sci.* **2017**, *18*, 1726. [CrossRef] [PubMed]

5. Borgmann, D.M.; Mayr, S.; Polin, H.; Schaller, S.; Dorfer, V.; Obritzberger, L.; Endmayr, T.; Gabriel, C.; Winkler, S.M.; Jacak, J. Single Molecule Fluorescence Microscopy and Machine Learning for Rhesus D Antigen Classification. *Sci. Rep.* **2016**, *6*, 32317. [CrossRef] [PubMed]

6. Poulter, N.S.; Pollitt, A.Y.; Davies, A.; Malinova, D.; Nash, G.B.; Hannon, M.J.; Pikramenou, Z.; Rappoport, J.Z.; Hartwig, J.H.; Owen, D.M.; et al. Platelet actin nodules are podosome-like structures dependent on Wiskott—Aldrich syndrome protein and ARP2/3 complex. *Nat. Commun.* **2015**, *6*, 7254. [CrossRef] [PubMed]

7. Sams, M.; Silye, R.; Göhring, J.; Muresan, L.; Schilcher, K.; Jacak, J. Spatial cluster analysis of nanoscopically mapped serotonin receptors for classification of fixed brain tissue. *J. Biomed. Opt.* **2013**, *19*, 11021. [CrossRef] [PubMed]

8. Huang, B.; Jones, S.A.; Brandenburg, B.; Zhuang, X. Whole-cell 3D STORM reveals interactions between cellular structures with nanometer-scale resolution. *Nat. Methods* **2008**, *5*, 1047–1052. [CrossRef] [PubMed]

9. Dani, A.; Huang, B.; Bergan, J.; Dulac, C.; Zhuang, X. Superresolution Imaging of Chemical Synapses in the Brain. *Neuron* **2010**, *68*, 843–856. [CrossRef] [PubMed]

10. Xu, K.; Babcock, H.P.; Zhuang, X. Dual-objective STORM reveals three-dimensional filament organization in the actin cytoskeleton. *Nat. Methods* **2012**, *9*, 185–188. [CrossRef] [PubMed]

11. Van De Linde, S.; Löschberger, A.; Klein, T.; Heidbreder, M.; Wolter, S.; Heilemann, M.; Sauer, M. Direct stochastic optical reconstruction microscopy with standard fluorescent probes. *Nat. Protoc.* **2011**, *6*, 991–1009. [CrossRef] [PubMed]

12. Dempsey, G.T.; Vaughan, J.C.; Chen, K.H.; Bates, M.; Zhuang, X. Evaluation of fluorophores for optimal performance in localization-based super-resolution imaging. *Nat. Methods* **2011**, *8*, 1027–1036. [CrossRef] [PubMed]

13. Van de Linde, S.; Krstić, I.; Prisner, T.; Doose, S.; Heilemann, M.; Sauer, M. Photoinduced formation of reversible dye radicals and their impact on super-resolution imaging. *Photochem. Photobiol. Sci.* **2011**, *10*, 499–506. [CrossRef] [PubMed]

14. Gunsolus, I.L.; Hu, D.; Mihai, C.; Lohse, S.E.; Lee, C.S.; Torelli, M.D.; Hamers, R.J.; Murhpy, C.J.; Orr, G.; Haynes, C.L. Facile method to stain the bacterial cell surface for super-resolution fluorescence microscopy. *Analyst* **2014**, *139*, 3174–3178. [CrossRef] [PubMed]

15. Nahidiazar, L.; Agronskaia, A.V.; Broertjes, J.; den van Broek, B.; Jalink, K. Optimizing imaging conditions for demanding multi-color super resolution localization microscopy. *PLoS ONE* **2016**, *11*, e0158884. [CrossRef] [PubMed]

16. Bearer, E.L.; Prakash, J.M.; Li, Z. Actin dynamics in platelets. *Int. Rev. Cytol.* **2002**, *217*, 137–182. [PubMed]

17. Hartwig, J.H.; DeSisto, M. The cytoskeleton of the resting human blood platelet: Structure of the membrane skeleton and its attachment to actin filaments. *J. Cell Biol.* **1991**, *112*, 407–425. [CrossRef] [PubMed]

18. Italiano, J.E.; Lecine, P.; Shivdasani, R.A.; Hartwig, J.H. Blood Platelets Are Assembled Principally at the Ends of Proplatelet Processes Produced by Differentiated Megakaryocytes 7. *J. Cell Biol.* **1999**, *147*, 1299–1312. [CrossRef] [PubMed]

19. Falet, H.; Barkalow, K.L.; Pivniouk, V.I.; Barnes, M.J.; Geha, R.S.; Hartwig, J.H. Roles of SLP-76, phosphoinositide 3-kinase, and gelsolin in the platelet shape changes initiated by the collagen receptor GPVI/FcR gamma-chain complex. *Blood* **2000**, *96*, 3786–3792. [PubMed]

20. Watson, S.P. Platelet activation by extracellular matrix proteins in haemostasis and thrombosis. *Curr. Pharm. Des.* **2009**, *15*, 1358–1372. [CrossRef] [PubMed]

21. Mellor, H. The role of formins in filopodia formation. *Biochim. Biophys. Acta Mol. Cell Res.* **2010**, *1803*, 191–200. [CrossRef] [PubMed]

22. Grimm, J.B.; Klein, T.; Kopek, B.G.; Shtengel, G.; Hess, H.F.; Sauer, M.; Lavis, L.D. Synthesis of a Far-Red Photoactivatable Silicon-Containing Rhodamine for Super-Resolution Microscopy. *Angew. Chem. Int. Ed.* **2016**, *55*, 1723–1727. [CrossRef] [PubMed]

23. Heilemann, M.; Margeat, E.; Kasper, R.; Sauer, M.; Tinnefeld, P. Carbocyanine dyes as efficient reversible single-molecule optical switch. *J. Am. Chem. Soc.* **2005**, *127*, 3801–3806. [CrossRef] [PubMed]

24. Symons, M.H.; Mitchison, T.J. Control of actin polymerization in live and permeabilized fibroblasts. *J. Cell Biol.* **1991**, *114*, 503–513. [CrossRef] [PubMed]

25. Wolter, S.; Löschberger, A.; Holm, T.; Aufmkolk, S.; Dabauvalle, M.C.; Van De Linde, S.; Sauer, M. rapidSTORM: Accurate, fast open-source software for localization microscopy. *Nat. Methods* **2012**, *9*, 1040–1041. [CrossRef] [PubMed]

26. Jacak, J.; Schaller, S.; Borgmann, D.; Winkler, S.M. Characterization of the Distance Relationship Between Localized Serotonin Receptors and Glia Cells on Fluorescence Microscopy Images of Brain Tissue. *Microsc. Microanal.* **2015**, *21*, 826–836. [CrossRef] [PubMed]

27. Göhring, J.; Fulcher, N.; Schilcher, K.; Barta, A.; Jacak, J. Suitable transfection methods for single particle tracing in plant suspension cells. *Plant Methods* **2014**, *10*, 15. [CrossRef] [PubMed]

28. Huang, F.; Schwartz, S.L.; Byars, J.M.; Lidke, K.A. Simultaneous multiple-emitter fitting for single molecule super-resolution imaging. *Biomed. Opt. Express* **2011**, *2*, 1377. [CrossRef] [PubMed]

29. Dennis, J.E.; Mei, H.W. Two new unconstrained optimization algorithms which use function and gradient values. *J. Optim. Theory Appl.* **1979**, *28*, 453–482. [CrossRef]

30. Mortensen, K.I.; Churchman, H.L.S.; Spudich, J.A.; Flyvbjerg, H. Optimized localization-analysis for single-molecule tracking and super-resolution microscopy. *Nat. Methods* **2010**, *7*, 377–381. [CrossRef] [PubMed]

31. Han, R.; Wang, L.; Xu, F.; Zhang, Y.; Zhang, M.; Liu, Z.; Ren, F.; Zhang, F. Drift correction for single-molecule imaging by molecular constraint field, a distance minimum metric. *BMC Biophys.* **2015**, *8*, 1. [CrossRef] [PubMed]

32. Rosenblatt, M. Remarks on Some Nonparametric Estimates of a Density Function. *Ann. Math. Stat.* **1956**, *27*, 832–837. [CrossRef]

33. Parzen, E. On estimation of a probability density function and mode. *Ann. Math. Stat.* **1962**, *33*, 1065–1076. [CrossRef]

RESEARCH ARTICLE

Statistical analysis of 3D localisation microscopy images for quantification of membrane protein distributions in a platelet clot model

Sandra Mayr[1], **Fabian Hauser**[1], **Sujitha Puthukodan**[2], **Markus Axmann**[1], **Janett Göhring**[3], **Jaroslaw Jacak**[1] *

1 University of Applied Sciences Upper Austria, Linz, Austria, **2** Johannes Kepler University Linz, Linz, Austria, **3** Center for Pathophysiology, Infectiology and Immunology, Institute for Hygiene and Applied Immunology, Medical University of Vienna, Vienna, Austria

* jaroslaw.jacak@fh-linz.at

Abstract

We present the software platform 2CALM that allows for a comparative analysis of 3D localisation microscopy data representing protein distributions in two biological samples. The in-depth statistical analysis reveals differences between samples at the nanoscopic level using parameters such as cluster-density and -curvature. An automatic classification system combines multiplex and multi-level statistical approaches into one comprehensive parameter for similarity testing of the compared samples. We demonstrated the biological importance of 2CALM, comparing the protein distributions of CD41 and CD62p on activated platelets in a 3D artificial clot. Additionally, using 2CALM, we quantified the impact of the inflammatory cytokine interleukin-1β on platelet activation in clots. The platform is applicable to any other cell type and biological system and can provide new insights into biological and medical applications.

Author summary

Single-molecule localisation microscopy (LM) became more accessible over the past years. Companies and research facilities developed instruments for 3D/2D LM, but there is a lack of comparison methods for LM-images. Our tool offers a new comparative analysis of LM data. Our system is capable of showing the difference on the level of single molecule clusters and provides information on differences between images on various scales. We determine if clusters formed of molecule localisations are comparable. We display the difference on density or the shape of these formed clusters for a certain dimension. Since the comparison is performed for all dimensions, the differences between cluster properties are observed very precisely. Thereby, we learn if clusters of molecules are formed and how they differ in both samples. For a fast/concluding comparison, we have added tools which derive a percentage of equality of both images based on all comparison results. The tool is useful for comparison of images of molecules in cells, which are expected to differ from

each other (exemplified with platelets). The differences might be caused by drug treatment, different disease progress or other environmental/genetical issues. The analysis is performed at a single cell level as well as cell cluster level.

This is a *PLOS Computational Biology* Methods paper.

Introduction

LM has progressed immensely over the last decade [1–5], however only a few of the approaches towards a comparative analysis of the resulting data have been achieved [6–9]. Primarily, these studies utilised comparative analyses of single molecules in the context of co-localisation in cells [10–14], with the majority visualising the 2D and 3D arrangement of proteins [10, 12, 13, 15, 16].

First attempts for cluster analysis for LM data, developed by Owen et al. [17], were based on Ripley's K-function, which quantifies the global distribution and heterogeneity of proteins at the cell plasma membrane. Alternatively, analysis systems like SR-Tesseler [18] or ClusterVisu [19] based on Voronoi tessellation were developed. These methods were well suited for visualization and rendering of localisation density distribution in a sample or colocalization between molecules primarily for 2D data.

Clustering–the formation of micro- and nano-domains within plasma membranes–is now a widely recognized feature that ensures hierarchical organisation of many proteins. The functions of these clusters are diverse [20, 21] and impaired integrin clustering for example has been shown to be involved in thrombasthenia [22]. However, there is a general lack of methods that enable a comparative analysis of localisation microscopy data on protein distributions and clustering.

Mainly, the presented analysis extracts spatial descriptors (spatial features), which allow the determination of the similarity of 3D localisation microscopy data of two samples, regardless of their rotation, translation and quantity. The basis for the feature extraction is multiple resampling of both samples with a given number of localisations (typically between 2 000 and 10 000) which increases the amount of data for statistical analysis and reduces the calculation time to minutes for very large samples (> 200 000 points = localisations). Furthermore, our method does not require transformation of the coordinate system, synchronisation of the region of interest (ROI) size or possible normalization for both samples.

For each pair of such bootstrap sub-samples, sequential hierarchical clustering of localisations is performed. To characterise clusters with a specific size, two crucial parameters have been derived–density and curvature distribution. For these distributions we perform nonparametric 2-sample statistical tests (such as Kolmogorov-Smirnov test, Wilcoxon rank sum test) and build a p-value-map (for each pair of samples and each cluster size, forming a first level of analysis). These p-value maps are directly used among other parameters (aggregated p-values) from second level of analysis to train the multilayer perceptron (MLP) neural network. In addition, in order to build a more robust analytical measure of similarity, we average over the generated distributions and their aggregations and generalizations. To aggregate the results of the 2-sample statistical tests, the weighted AND operator of fuzzy membership functions is used. The generalisation is performed by applying statistical tests on average values of density and curvature distributions and on values of the Ripley's K-function. The maximum Ripley's H function is used primarily to establish the parameters for the random sample generator.

Currently, global comparative analyses of clot formations have only used diffraction-limited fluorescence microscopy to characterise morphological changes (e.g. shape change upon activation) and the cytoskeletal organisation of platelets (e.g. actin and tubulin reorganisation) [23–29]. Nanoscopic localisation microscopy analyses have only been performed for single platelets characterising the content of α-granules [30], the arrangement of actin filaments [31, 32], various actin associated proteins (e.g. P4 or vinculin), and mitochondria [33, 34]. Therefore, an artificially formed clot presents a proficient system to characterise environmentally-induced protein redistributions on a nanoscopic scale.

In this study, we present a software tool that quantitatively compares and classifies two biological samples based on the protein distributions at the nanoscale using 3D localisation microscopy data. Our tool– 2-sample Comparative Analysis of 3D Localisation Microscopy Data (2CALM)–is an analysis pipeline, which organizes LM data into protein clusters of different dimensions and calculates the samples' statistical parameters using various numerical methods. The images obtained from LM can be regarded as a 3D cloud of points. A comparative analysis of such clouds requires the extraction of features representing their geometrical structure without losing accuracy. Several deep machine-learning algorithms, especially convolution neural networks (CNN), have been applied to single 3D point cloud analysis. A common approach is to rasterize the 3D point data into a 3D voxel grid [35–37]. This approach, however, suffers from a trade-off between its computational cost and its approximation accuracy. Thus, we employ a different concept and propose a new representation of a LM-derived cloud of points. This representation is based on empirical distributions of the density and the curvature of the point's clusters within point-clouds having a predetermined maximal dimension, yielding density and curvature distributions for each sample. These distributions are compared with non-parametrical statistical tests such as Kolmogorov-Smirnov or Wilcoxon test. The results of the tests create a features-array of the similarity of both samples that is not dependent on their size and location in space. Our system uses the constructed feature-arrays to determine the analytical similarity measure between samples and to train the fully-integrated MLP neural network for automatic classification of samples similarities. Generally, the system can be used to compare any 3D and 2D cloud of points regardless the origin of the samples and primarily provides a comparison between two LM images. The results directly show the comparison between the densities/curvatures of molecular clusters and do not directly provide information's on cellular structures.

For demonstration of the biological importance and applicability of 2CALM, we quantitatively analysed the nanoscopic distribution of CD41 and CD62p proteins on activated platelets within an artificial clot using 3D dSTORM. As changes in protein distribution during platelet activation and thrombus formation can impact further downstream signalling, the effect of the pro-inflammatory molecule interleukin 1-beta (IL-1β) on the CD62p distribution in platelets within an artificial clot was analysed.

CD41 (integrin α-IIb) is a protein that is present in the cell membrane as well as in the α-granules of platelets [38]. As part of the fibrinogen receptor GPIIb/IIIa it binds fibrinogen and von Willebrand factor (vWF). Upon activation, CD41 molecules from the granules are incorporated into the cell membrane. Platelet aggregates, which are formed by GPIIb/IIIa-fibrinogen interaction, are stabilized by the interaction of CD62p (P-selectin), which binds P-selectin glycoprotein ligand-1 and platelet sulfatides [39–41]. CD62p is a cell adhesion molecule and is transported upon activation from its location in the α-granules to the cell membrane [26, 42–46]. Activation of the coagulation system (i.e. clot formation) is heavily influenced by pro-inflammatory molecules such as IL-1β. These molecules have been shown to increase the response of the platelets towards elevated aggregation [47, 48].

The performance of 2CALM was tested by analysing the distributions of two protein types (CD41 and CD62p), which are known to exhibit different clustering behaviour upon activation. The detailed analysis of 2CALM shows the protein distributions of CD41 and CD62p at the nanoscopic level. Furthermore, 2CALM was tested on a system, which changes the protein (CD62p) distribution upon external treatment. We show that CD62p distributes diversely within untreated and IL-1β-treated clots providing different clustering-based statistical parameters. The data obtained from LM experiments on CD62p distribution in platelets were compared to simulated datasets. The presented experimental and simulated data showcase the software´s utility to support researchers in advanced two-sample comparisons of heterogeneous LM data. It will therefore advance the thorough investigation and ultimately the understanding of the nanoscopic organization of proteins in complex tissues.

Results

We developed a software system capable of a two-sample comparison named 2CALM (MatLab environment). In several experiments, artificial clots were stained, imaged using 3D dSTORM, and analysed. The resulting analysis is comprised of information on the sub-diffractional as well as on the bulk level, obtained in one measurement. The features of the 2CALM software system are depicted in Fig 1A. This platform contains a two-level statistical analysis of 3D spatial cluster features. The 1st-level analysis directly compares the properties of spatial clusters (cluster density and/or cluster curvature distributions) derived from LM datasets with different clustering dimensions [49–52]. The 2nd-level statistical tests are performed on averaged cluster features to assess their randomness and the distribution of the average cluster's curvature (shape) and density. The obtained sample features can then be compared pairwise using the methods of a statistic tools module, relying on a comparison of averaged statistical values (e.g. average cluster density or curvature distributions) of bootstrapped re-samples. The determined features are based on the relative cluster's density distributions for each clustering dimension and their individual curvature distribution and are independent of cluster positions and orientations. A detailed workflow of the features extraction and aggregation is depicted in S2 Fig.

Biological test system and image acquisition

In order to show the applicability of 2CALM, we designed an artificial clot [53]. After mixing thrombin, fibrinogen and platelets, the cells coagulate on a glass slide, which yields a viscous 3D clot. For visualisation purposes, we immuno-stained platelets within the protein matrix with fluorescently labelled antibodies that target CD41 and CD62p proteins. In all clot experiments, CD41 was labelled with Alexa488-conjugated anti-CD41-antibody, and CD62p was labelled with Alexa647-conjugated anti-CD62p-antibody. For imaging, we applied direct stochastic optical reconstruction microscopy (dSTORM) [54]. We used an oxygen scavenger system (OxEA) [55], which allows for two-colour imaging without buffer exchange. To adjust the blinking rates of both fluorophores, an additional UV-laser illumination was utilized. A cylindrical lens in the optical detection pathway of the microscope introduced astigmatism and an axially dependent deformation of the point spread function (PSF) of individual emitters. The single-molecule positions were determined using customized software with fitting routines derived from rapidSTORM [56]. Automated tools for extraction, characterization and comparison of the protein distributions at the nanoscopic level were implemented.

Software features: Dataset pre-processing module

2CALM includes a collection of software tools enabling a pairwise comparative analysis of independent sets of localisation microscopy data. Datasets usually have a different number of
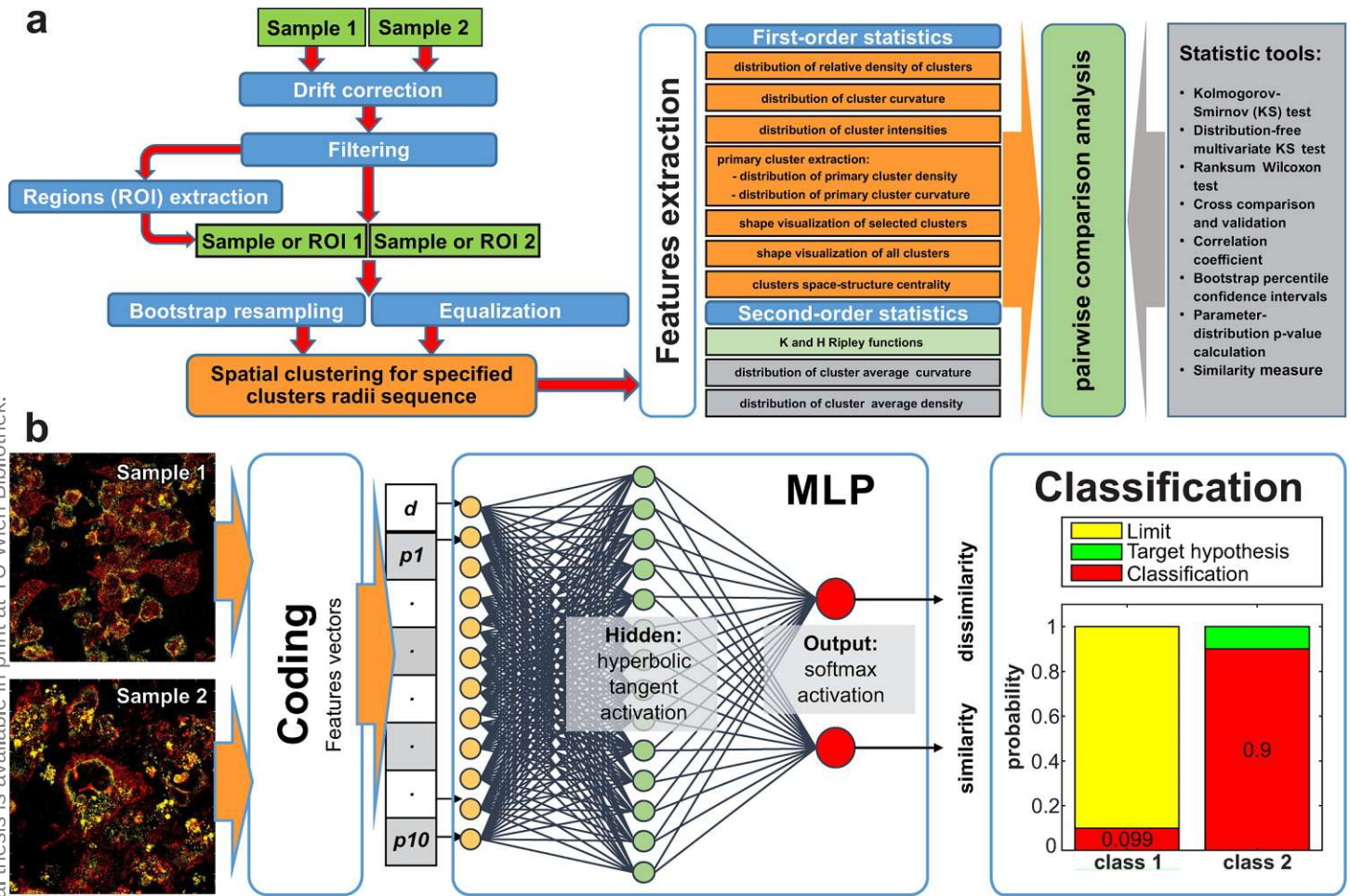
Fig 1. 2CALM workflow. (a) represents the features of the 2CALM platform. Datasets are pre-processed using drift correction and filtering of outliers (optionally: ROI-extraction). For a full image comparison, dataset sizes are optionally equalized. The default bootstrapping step re-samples the datasets into sub-samples (used for spatial clustering). Hierarchical spatial clustering enables the extraction of the density-distribution and the curvature-distribution of clusters. For comparison, a two-level, multi-parameter analysis of different clustering dimensions is performed. Kolmogorov-Smirnov-, Wilcoxon-test and bootstrap confidence interval analysis is used for a comparison of protein distributions. (b) depicts the structure of the multilayer perceptron (MLP) neural network based machine learning module. The clustering from (a) provides parameters (feature vectors) which are used to train a MLP (including one hidden layer) network to assign the datasets to their classes (similarity classification).

https://doi.org/10.1371/journal.pcbi.1007902.g001

localisation events (often gathered into 3D point-clouds), varying noise due to unspecific binding and/or localisation errors resulting from sample drift during the measurement. Our toolset enables noise filtration and drift correction. Typically, special convolution algorithms [57, 58] or fiducial markers [59, 60] are deployed to correct for sample drift; we expanded a developed drift correction algorithm [32] to support 3D position accuracy of localisation events [61]. The 3D dSTORM images contain single localisation events which are not of interest in cluster analysis and henceforth are classified as outlier points. Filtering of individual outlier points (or small group of points) is carried out using a DBSCAN (Density-Based Spatial Clustering of Applications with Noise) algorithm [62–65]. An additional modified version of DBSCAN [66] allows for an automatic determination of the ROI. It is used for spatially well-separated domains with single-molecule localisations (e.g. signals in sparsely distributed individual cells) (S11 Fig). Both tools–drift correction and outlier filtering–are combined in a dataset pre-processing module.

Software features: Equalization of data sets (bootstrapping)

Although an analysis of all points in a sample at once is possible, it is rather time-consuming and less robust to errors. When datasets have a small number of localisation events (up to 50 000), a 1st-level statistical analysis–after equalization of both samples–can be performed. The number of points is equalized to the smaller of the pairwise compared data sets. Representative datasets are shown in S1A and S1B Fig. When larger differences in localisation events are detected, errors due to a random selection of points from the equalized sample dataset may lead to an incorrect comparison, even though the samples originate from the same biological replica. In such instances bootstrapping is used to randomly draw events from the measured datasets, which yields an equalized data set. In order to improve the robustness of the analysis, we performed multiple re-sampling (bootstrapping) [67–69] using a defined number of points. The bootstrap procedure involves choosing random samples (with replacement) from a large dataset and analysing each bootstrap sample in a similar way. Bootstrapping reduces the risk of accidental one-time errors (when there are not sufficient points in a subgroup) and allows for better parameter-estimation for subsequent comparative analyses.

Software features: Statistical analysis of cluster features (Two-level statistics)

The 1st-level analysis relies on a direct comparison of sample features like cluster density and cluster curvature distributions for each cluster dimension. For a comparison between the protein distributions of the two samples, non-parametric statistical tests are used. The 2nd-level analysis combines the parameters obtained from the 1st-level analysis and compares them globally. It relies on a comparison of averaged values of localisation densities and curvatures per cluster dimension and eliminates the influence of noise (disturbance of point localisations). Additional K-/H-Ripley's tests [70, 71] show the deviation of the distributions from a random Poisson distribution.

Software features: Classification of similarity (Two-sample comparison)

Statistical Tools. Various statistical tests are implemented for a holistic two-sample comparison at nanoscopic and microscopic level. Non-parametric Kolmogorov-Smirnov (KS) [72–74] and Wilcoxon (WX) [75, 76] tests were used for a pairwise comparison of cluster features. In order to calculate the aggregated p-value (e.g. fusion of results of KS and WX tests) we applied the weighted t-norm-AND operator [77, 78] on the p-values of the KS-/WX-test obtained from the bootstrapping process. By introducing appropriate weights for the t-norm-AND operators the significance of a particular test increases. These tests precisely identify the cluster parameters necessary for classification of sample similarity/dissimilarity for any clustering dimension. It is not capable to automatically classify data sets.

To simplify the comparison, we determined a measure for sample similarity combining all cluster dimensions. We defined two similarity measures, sim_M and sim_L. sim_M is the rescaled aggregated p-value with an interval of [0,1]. If sim_M is < 0.5, the parameters describing clusters are dissimilar (see Fig 2C zoom-in). Sim_L measures the dependency of the critical area (spanning the cluster dimension/sizes interval and the significance level) and lower bound of the confidence interval of the aggregated p-value and delivers a value within the interval of [0,1].

Machine learning

In order to combine all features necessary for the similarity classification, we use a machine learning method, a MLP neural network, as a classifier of sample similarity [71, 79–81] (Fig
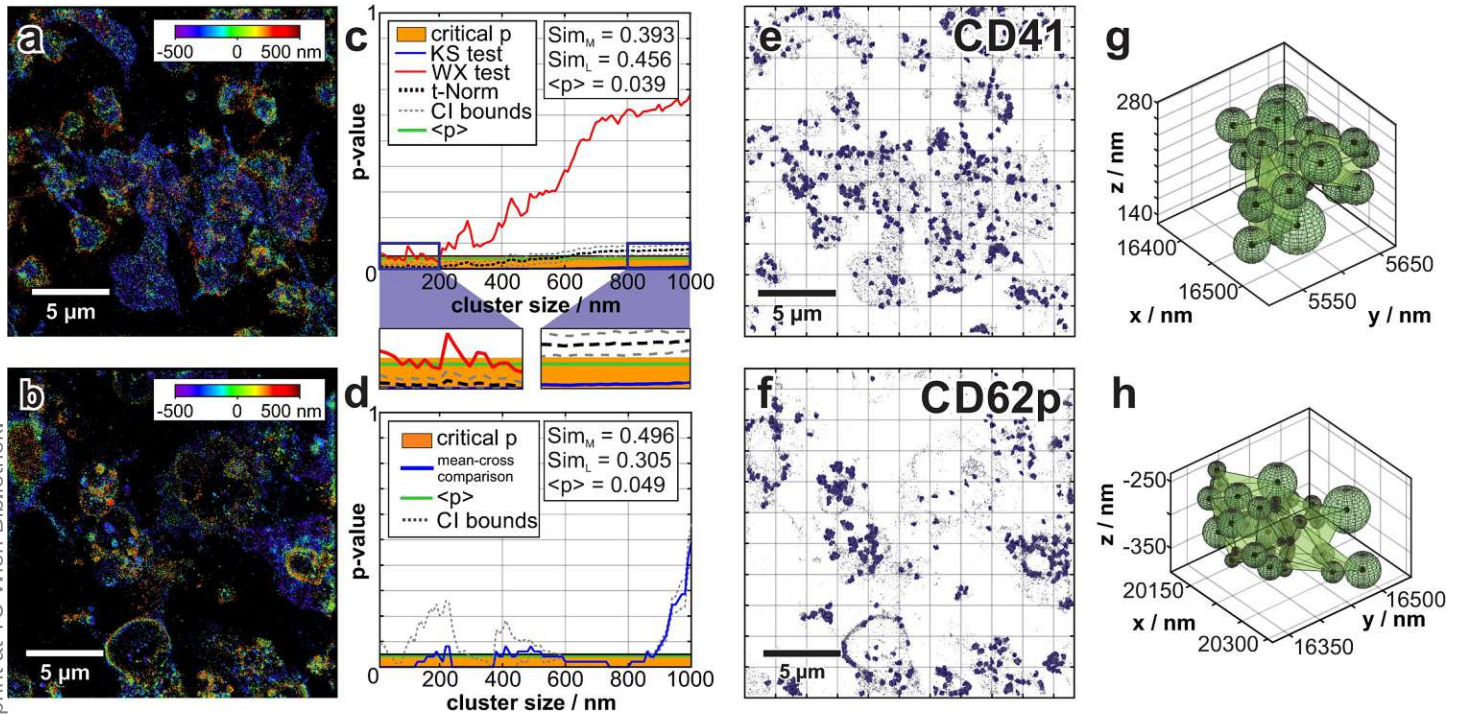
Fig 2. Two sample comparison of the CD62p and CD41 distributions in clots. (a) and (b) show reconstructed 3D dSTORM images (approx. 100 000 data points/ image). (a) shows the 3D distribution of CD41 (Alexa488-antibody). (b) represents the 3D distribution of CD62p (Alexa647-antibody). (c) shows the comparison of the cluster densities for all given cluster dimensions between the two datasets (1st-level comparison). The blue/red lines depict the KS- and WX-test results, respectively. The aggregated p-value for KS and WX tests (dashed black line) remains within the critical p-value-area (orange) disproving the similarity hypothesis. The zoomed-in areas depict: a cluster dimension (5 nm—200 nm, sim_M, sim_L below 0.5); pairwise KS- and WX-test comparisons of cluster densities for both samples indicate dissimilarity (left) and a second cluster dimension (800 nm—1000 nm, sim_M, sim_L larger 0.5); pairwise KS- and WX-test comparisons of cluster densities for both samples show similarity (right). (d) shows the 2nd-level comparison of the mean cluster density for all given cluster dimensions. The mean-cross p-value comparison (blue) and lower/upper confidential bounds (grey dashed line) are shown. (e) and (f) represents 600 clusters localized within the CD41/CD62p distribution respectively, displayed using the Delaunay-triangulation method (clustering dimension 390 nm). (g) shows two representative clusters from from (e) and (h) from (f).

https://doi.org/10.1371/journal.pcbi.1007902.g002

1B). The neural net consists of three layers: an input layer, a hidden layer and an output layer. Except for the input nodes, each neuron uses a nonlinear activation function. The network requires the preparation of input data for characterization; and it applies the previously determined statistic-based features of the dataset in the training and classification mode.

We trained the MLP neural network with a data set of CD41/CD62p protein distributions in an artificial clot. Approximately 262 000 training patterns were determined using this data set. The trained MLP neural network classifier was tested on ~40 different pairs of data sets, which were not included in the training set. All of the tests showed a similarity classification with a probability between 0.75 and 0.95 for a pairwise comparison of similar samples and <0.2 for a pairwise comparison of dissimilar samples (S2 Table), i.e. the parameter extraction presented in the analysis sets is a suitable base for machine learning based pattern recognition. The results on MLP neural network classification for a representative statistical comparison of sample pairs are presented in Fig 3G. The overall values of further data sets are show in the S2 Table.
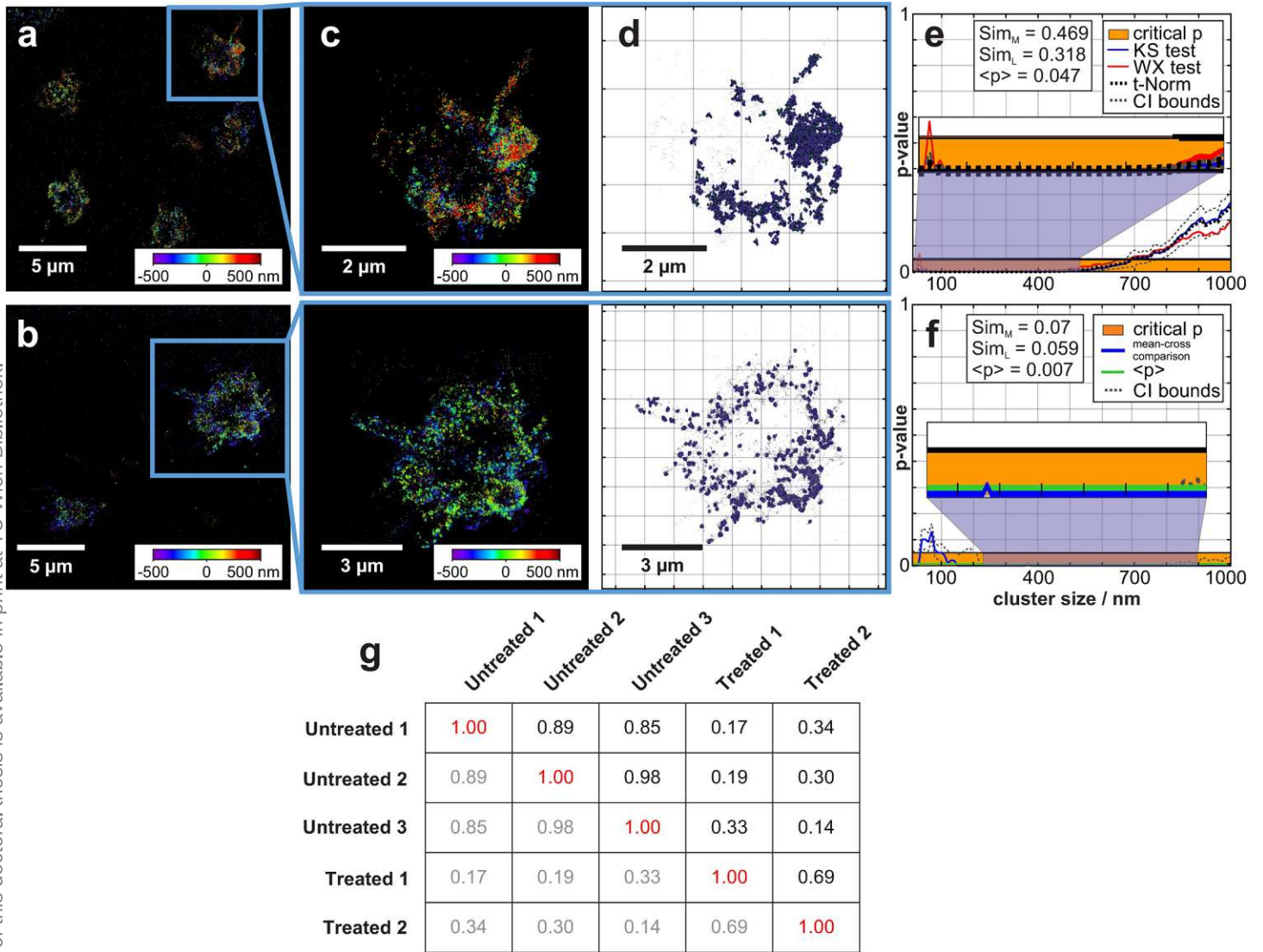
Proof-of-principle: Comparison of CD41 and CD62p clusters

In Fig 2, we show a typical reconstructed image of two areas in the central region of the clot, which visualises the distribution of CD62p (Fig 2A) and CD41 (Fig 2B) upon platelet

Fig 3. Comparison of IL-1β treated and untreated clot samples. (a) and (b) show reconstructed dSTORM images of two clots, untreated (a) and treated with IL-1β (b). In (c) zoomed images of two regions extracted from (a) and (b) are shown. In (d) two populations of clusters from both images with a cluster dimension of 145 nm are visualised. (e) shows the comparison of cluster densities for all given cluster dimensions between the two datasets (1st-level statistic). Blue and red lines depict the results of the KS- and WX-test, respectively [75, 88]. The aggregated p-value between KS and WX tests (black dashed line) remains below the critical p-value area (orange bar) and thus proves the dissimilarity hypothesis for most of the cluster dimensions. (f) shows the aggregated p-values of averaged density and curvature distribution, determined via mean-cross analysis (blue) and the average p-value (green, including confidential intervals: black dashed lines) ($sim_M = 0.07$ and $sim_L = 0.06$). The table in (g) shows the classification table with MLP neural network classification values for dissimilar and similar samples. The output values of the trained network can be interpreted as *a posteriori* probability of similarity hypotheses.

https://doi.org/10.1371/journal.pcbi.1007902.g003

activation (~ 100 000 single-molecule localisations each). The reconstructed images have been compared using the developed statistical tools, proving a dissimilarity of both datasets at a very detailed level.

1st-level statistics: KS/WX tests of cluster density and curvature

For each pair of data sets (or regions) hierarchical spatial clustering is performed [49–52]; i.e. we performed a 1st-level analysis for the relative density (Fig 2C) and curvature [82] (comparison data: S1A Fig) for all cluster dimensions of a given interval (typically from 5 nm to 1000

nm). Samples are typically equalized via the bootstrap method (100 curves for relative density and curvature of 100 re-samples all including 8000 points). Based on KS and WX tests, a direct comparison of the clusters density distribution and curvature distribution is performed (Fig 2C and S1D Fig). The determined p-values disprove the hypothesis of both samples being dissimilar. The aggregated p-value between KS-(blue) and WX-(red) tests = 0.04, and the similarity measures sim_M = 0.39 and sim_L = 0.45 indicate a difference in the cluster density distributions for all clustering dimensions between the two samples. The detailed density comparison proves that for clustering dimensions larger than 700 nm both samples have a significant similarity (Fig 2C). Further 1st-level analysis results on cluster curvatures (shape) [82] are presented in S1A–S1D Fig. S1C Fig represents the aggregated data of KS-/WX-test results on the characterization of cluster curvature for all clustering dimensions. The detailed curvature analysis indicates a similarity for clustering dimensions larger than 500 nm up to 1000 nm.

For the combination of the results of various tests, the calculated p-values of the individual ones are aggregated using the t-norm-AND operator (AND operation in fuzzy logic). For the similarity measure, the p-values are further transformed into sim_M and sim_L values by averaging the aggregated p-values and taking into account their confidence intervals. The process of hierarchical aggregation of individual p-values as shown in S2 Fig.

In conclusion, the results of averaging the KS-/WX-test values for cluster densities and curvatures of the bootstrapped re-samples indicate a strong dissimilarity of the samples for the maximal clustering dimension of an interval of 5 nm-1000 nm.

2nd-level statistics: Mean-cross comparison of cluster density and curvature distribution

2nd-level statistics were performed solely for the bootstrap derived re-samples (Fig 2D and S1E–S1I Fig). This relies on a mean-cross p-value obtained from cross-comparison tests (KS/WX) of the averaged cluster density distributions between all bootstrap resamples. Fig 2D shows the 2nd-level comparison of the mean cluster density for all given cluster dimensions. The mean-cross comparison for curvature distributions is presented in S1E Fig with mean-cross p-values and lower/upper confidential bounds. The mean-cross p-value (KS-/WX-test) of the density distributions equals 0.049, and sim_M = 0.49 and sim_L = 0.30 underlines the nanoscopic dissimilarity of the two samples. Similar to the results on density analysis, we determined the behaviour of the cluster curvature (S1E Fig); a mean-cross p-value for curvature of 0.23 and sim_L = 0.34 indicates a dissimilarity between the two samples. Comparable to the results of the 1st-level statistics, only for cluster dimensions larger than 700 nm the curvature as well as density distributions indicated a stronger similarity. The mean-cross p-values of the cluster curvature show a tendency towards sample similarity for cluster dimensions ~200 nm.

Additionally, the individual clusters can be visualised three-dimensionally using the Delaunay-triangulation method [83, 84] or as maximum radius spheres packed at given locations [85] (Fig 2G and 2H). Fig 2E and 2F show 600 clusters from both datasets (cluster dimension 390 nm). In Fig 2G and 2H two randomly chosen clusters have been depicted from e and f, respectively. The software feature for cluster visualisation provides detailed information on localisation of the clusters within the clot for each clustering dimension.

For large clustering dimensions, clusters cover large parts of a platelet (size 1–5 μm, see S11E–S11G Fig) and can therefore be regarded as 'bulk signal' by looking at micrometer-sized clusters in the nanoscopic scale regime. Hence, the results on a nanoscopic and microscopic level for dataset comparison are provided simultaneously. Further analysis (S1F Fig) displays the aggregated p-values of a mean-cross analysis for the cluster densities and curvatures (for all cluster dimensions). These aggregated p-values remain below the boundary of the critical p-

value for all clustering dimensions with a dimension smaller than 700 nm. The aggregated p-values of the mean-cross analysis for the cluster densities and curvatures again indicates a dissimilarity of the samples.

2nd-level statistics: K-/H-Ripley's functions

For further 2nd-level statistics we performed a Ripley's K-/H-analysis [70, 86, 87] (S1G–S1I Fig) on the bootstrap sample data. The K-/H-Ripley's function values are determined for each clustering dimension and are used to additionally prove the diversity of the two samples. The comparison of the values from the KS-/WX-test applied on the 3D K-/H- Ripley's function results for each of the cluster's dimensions (shown in S1H Fig). The results show an average p-value of 0.087, $sim_M = 0.71$ and $sim_L = 0.14$ for the K-Ripley function (left) and an average p-value of 0.086, $sim_M = 0.71$ and $sim_L = 0.22$ for the H-Ripley function (right). Additionally, the mean-cross analysis of the K-Ripley function distributions represented in S1H Fig are shown in S1I Fig. The overall Ripley analysis (sim_L) confirms the sample dissimilarity except for a small interval of the cluster dimension (400 nm– 600 nm). For these samples (Fig 1), the comparison based on the Ripley functions confirms the analysis performed with the clustering methods.

1st-level and 2nd-level statistics: MLP neural network

A multilevel analysis yields a general dissimilarity between CD41 and CD62p spatial distributions within a clot for the presented data sets. Additional data sets and analysis results are shown in S3–S8 Figs. We present in detail a pairwise comparison of CD41 distributions and CD62p distributions in distinct clots. In contrast to the sample presented in Fig 2, some CD41 and CD62p distributions in clots cannot be unambiguously discriminated against by individual statistical tests. Therefore, multilevel cross-testing is explicitly required. In particular, the data presented in S7 Fig and S8 Fig show divergent results regarding cluster comparison. For these technical replicas, a significant difference between the results of the 1st-/2nd-level cluster-based analysis and the results on K-/H- Ripley's analysis for all cluster distances is observable (S8 Fig (cluster analysis) and S8F–S8I Fig (Ripley analysis). The K-/H- Ripley's analysis indicates a strong similarity for clusters larger than 400 nm, which is not the case for all other 1st-/2nd-level cluster-based statistics. The calculation of the mean-cross p-value for all the parameters rejects the null hypothesis of similarity, showing that both datasets are dissimilar (S8H Fig). All statistical p-values are represented in S1 Table. The data comparison confirmed a significant dissimilarity for cluster dimensions. First level analysis shows a dissimilarity ($sim_M = 0.006$ and $sim_L = 0.5$ for density and curvature comparison, respectively). A higher similarity between the curvatures occurs only for cluster < 150 nm. Second level analysis indicates a general dissimilarity (aggregated sim_M values are 0.6 and 0.3 for density/curvature comparison, respectively). The mean-cross comparison of all results indicates a strong dissimilarity ($sim_M = 0.3$). The Ripley's K-/H-functions show a higher similarity $sim_M = 0.67/0.69$. The MLP neural network indicates a 0.74 probability for dissimilarity. A comparison of a clot sample (CD41 labelled) and simulated data is presented in S13 Fig. In the last analytical step the MLP neural network was applied for a comparison of the protein distributions of CD41 and CD62p in the platelet clots. The MLP neural network analysis showed that the samples were classified as similar with *a posteriori* probability of ~0.95 for a pairwise comparison of similar data sets and below 0.2 for a pairwise comparison of dissimilar ones. The *a posteriori* probabilities of the similarity hypotheses are depicted in S1 Table. The trained MLP neural network clearly discriminates between the two clustered protein populations under investigation within clots.

Characterization of CD62p clusters after platelet activation by the cytokine IL-1β

To quantify the effect of IL-1β on platelet activation, our software toolbox has been used to analyse dSTORM data of CD62p secretion. Various cytokine-treated and untreated samples were investigated. Due to IL-1β treatment, heterogeneities in clot formation (more sparsely distributed platelets) are observable. In order to capture the best overall picture of CD62p membrane incorporation after IL-1β treatment, images with varying cell densities were compared. We observed that the numbers of clusters changes significantly depending on clustering dimension. Herein, for cluster dimensions of 80 nm, 3620 and 9106 clusters were detected in total, whereas for cluster dimensions of 145 nm, 1849 and 5205 clusters were detected in treated and untreated samples, respectively. Furthermore, data obtained from sparse and dense clot regions were analysed. For a comparison of regions with sparsely distributed platelets, the best results were obtained for segmented images. The DBSCAN-derived segmentation is crucial for 2CALM analysis, especially in cases of sparsely distributed platelets; the unspecific signal outside the regions of interest exerts an influence on direct cluster comparison (for full image comparison). A detailed description of the differences in the comparison between segmented and full images is shown in Fig 3 and S9 Fig. Fig 3A–3D depict overviews and randomly chosen regions (image segmentation) for analysis in a cytokine-treated and untreated clot, respectively. Fig 3E depicts a direct 1st-level comparison of the clusters density distribution (curvature distribution is shown in Supplementary S6B Fig) in the chosen regions (S9A Fig). As can be seen in Fig 3E, untreated and treated samples gain similarity for larger cluster dimensions (> 800 nm). This difference was observed reproducibly for large as well as small extracted ROIs.

The 1st-level analysis results of cluster density and curvature indicates that both samples are in general dissimilar, whereas for clustering dimensions larger than 800 nm, both samples show a weak similarity. Overall, the sim_M- and sim_L-values determined for the 1st-level analysis are 0.46 and 0.31, respectively. With regards to cluster density, the comparison indicates that only for cluster dimensions larger than 800 nm a similarity of these two samples can be observed. The 2nd-level analysis of curvature confirms the dissimilarity hypothesis ($sim_M = 0.46$ and $sim_L = 0.45$) (S9B Fig). The mean-cross comparison of the aggregated KS-/WX-test values for density and curvature also shows a dissimilarity (Fig 3F).

The comparison of the averaged cluster curvatures tends to gain similarity for clustering dimensions larger than 500 nm (S9B Fig). The mean-cross analysis of the combined statistical data on 1st- and 2nd-level cluster density and curvature comparison is shown in S9C Fig. Results from the K-/H-Ripley-analysis support the cluster comparison data S9D and S9E Fig (K-/H-Ripley's-function (K-left, H-right) comparison for sim_M/sim_L are 0.03/0.01 and 0.04/0.01, respectively). The aggregation values of these data sets show similar tendencies (S9E Fig). A comparison of CD62p protein distribution and clusters for IL-1β treated and untreated samples verifies the effect of this cytokine on platelet activation in cluster formation. For clustering ranges between ten and a few hundred nanometres, the data sets differ most; this effect has not been observed in such detail before (see S2 Table).

The MLP neural network was used for a comparison of IL-1β treated and untreated clots. The neural network clearly classifies the samples based on the CD62p protein distribution. The tests showed a classification with a probability of 0.9 for a pairwise comparison of similar data sets and below 0.2 for a pairwise comparison of dissimilar ones. The *a posteriori* probability of similarity hypotheses are depicted in S2 Table. The results of the IL-1β treated samples are remarkable: In general, a larger heterogeneity within the group of treated samples in comparison to untreated samples can be observed (similarity probability = 0.67 for MLP

comparison of cytokine-treated samples; similarity probability > 0.8 for MLP neural network comparison within the group of untreated samples, Fig 3G).

Discussion

In this study, we demonstrated that 3D LM (dSTORM) with subsequent advanced statistical analyses can be used as a tool to determine and classify differences in protein distributions between two datasets. We have successfully used 2CALM for a comparison of CD41/CD62p distributions in platelets within a clot and for determination of the effect of IL-1β-treated platelets on CD62p membrane distribution.

The highly abundant CD41 (part of fibrinogen receptor GPIIb/IIIa) primarily binds fibrinogen, which bridges the actin cytoskeleton with the extracellular matrix to provide mechanical stability. Clustering of this membrane protein is known to be required for full activation of signal transduction (together with receptor occupancy) and acts as a signalling centre resulting in formation of focal adhesions [22]. The standard activation marker CD62p stabilizes platelet aggregates, which are formed by GPIIb/IIIa-fibrinogen interaction. Clustering of this activation marker has not been analysed previously.

Within this study, we observed apparent differences in the distributions of these two membrane proteins within a clot: While CD41 is distributed over the entire cell surface (see Fig 2A), CD62p's differing spatial arrangement can also be found concentrated on cell edges (see Fig 2B) and in the central region of platelets in the "fried-egg" morphology. This is caused by squeezing of organelles and granules during spreading [26, 32]. It is important to note that CD41 distribution at single cells' edges within the clot are located higher in z (app. 750 nm) than those within the cell area (Fig 2A), pointing towards the presence of inactivated, discoid cells within the clot–a phenomenon that has previously been reported in literature about murine thrombus formation [89, 90]. In Fig 2B, CD62p-positive vesicles of 400 nm– 800 nm in size most likely constitute microvesicles, which are known to be rich in CD62p and have a corresponding size of 100 nm up to 1 μm [91]. CD62p clustering (as clearly demonstrated in this study) may serve the formation of microclusters in order to support cell adhesion. A comparison of the CD41 and CD62p on a nanoscopic level in a 3D clot has not been addressed previously. Few studies, alongside other findings, show changes in the distribution of either CD41 or CD62p upon activation in platelets [46, 92, 93]. In general, our nanoscopic comparative analysis of CD41/CD62p cluster distributions shows a dissimilarity between the samples. The results on the 1st- and the 2nd-level statistics are in accordance and correlate well with the obtained Ripley's statistic. For a comprehensive quantification, the detailed comparison results on 1st- and 2nd-level statistics have been combined to teach a MLP neural network, which automatically classifies the samples. In S3–S6 Figs, we have shown the results of a comparison of two CD62p and of two CD41 labelled samples. In both cases, a high similarity of comparison levels has been determined. S8 Fig represents a comparison of different CD41 and CD62p labelled samples. In this experiment, the Ripley analysis does not match the more detailed results on cluster comparison. These results demonstrate that an analysis taking into account multiple sample-derived parameters provides a reliable input dataset for the MLP neural network.

Previous reports as well as preliminary experiments (S12 Fig) indicate that the spatial pattern of CD62p transported to the plasma membrane from the α-granules changes significantly upon IL1-β treatment [94]. We used our software platform 2CALM to compare the CD62p distribution of platelets in clots that are either untreated or treated with the inflammatory cytokine IL1-β. As shown in S9 Fig and Fig 3, results on comparison of cluster density and curvature diverges between the two compared data sets. Our results clearly show that CD62p distributes and clusters differently upon platelet activation by IL-1β treatment confirming

previous reports in the nanoscale regime [92]. Herein, we observed a lower cluster number for clusters of different size (80 nm and 145 nm for example) for cytokine-treated samples.

The 2nd-level statistical results for the pairwise comparison of data in ROI's yield sim_M values of 0.7 ± 0.2 for cluster density and 0.5 ± 0.2 for cluster curvature.

A correlation between ROI size and data set similarity can be observed. This indicates that CD62p protein clustering is affected when platelets interact with each other (compared to individual platelets in a clot) as is expected considering its role in homo- and heterotypic contact formation.

We showed that CD62p protein distribution in a clot changes upon cytokine-stimulation (Fig 3). The 1st- and 2nd-level statistical comparison, as well as the Ripley's statistics show that densities and curvatures of the formed clusters differ significantly for all cluster dimensions. The MLP neural network classification allows for determination of the class (treated/untreated) with a 100% accuracy for all pairwise comparisons of the measured samples (S2 Table). Additionally, we showed that although the analysis indicates a general similarity of treated samples only, crowded platelets show slightly different clustering behaviour when compared to individual platelets embedded in a clot (S14 Fig).

We have been able to show that our system allows the examination of time dependent behaviour of platelets induced by external factors, by taking a time series of samples (S13 Fig). In case at a certain timestamp a dissimilarity is detected, it is possible to further analyse which cluster sizes interval shows the difference. These clusters can be filtered and further analysed regarding their dynamic behaviour in time. Cluster visualisation can be seen as performed on individual clusters and for the whole sample by creating a triangulation image.

Recently, research has been conducted on deep-learning based 3D-point clouds classification and segmentation [95]. These methods, however, require a multitude of samples for training, are time-consuming and computationally inefficient for large numbers of points in the clouds [95]. By employing a MLP neural network, we were able to combine the copious determined parameters, ultimately allowing for the classification of sample similarity. MLP neural network simplifies the comparison and extracts a combined measure, determining the probability of two data sets either being similar or dissimilar. We classified the CD62p distribution on IL-1β-treated and untreated samples using this particular machine learning approach. The high classification accuracy of the MLP neural network confirms the efficient parametrisation for the cluster-based analysis. The MLP neural network classifies crowded and individual platelets as the same class. However, the detailed 1st-/2nd-level statistical comparison precisely identifies the cluster dimensions, for which both samples show the highest similarity and dissimilarity.

Extracted spatial features based on statistical tests are directly used to create and train MLP neural networks. As the MLP neural network tests have shown, it is very robust even in case of controversial results of particular statistical tests. The training set also includes features in which the Ripley's K-function test is false as opposed to correct classification by the first statistical level. In neural network learning, if level one retail features are consistent with level 2-features, this will increase the probability of correct sample similarity classification. The features indicate wrong estimations. If the classification acceptance threshold is exceeded (e.g. posteriori probability <60%) this will be a signal of bootstrapped re-sampling repetition with an increased number of points and possibly filtering the noise.

The presented system has following advantages and limitations: There are no restrictions in types of samples, various distributions of localisations (e.g. random, concentrated and fibrous) have been correctly classified by MLP neural network and analytical similarity measures. MLP neural network is robust for opposite level classifications and can easily be extended to multi-channel CNN. The analysis gives correct classifications in contrast to often ambiguous classifications with standard methods, e.g. Ripley's. Our program allows short calculation time

regardless of sample size and sample type (resampling of 2000–10 000 points) and the methods used are suitable for parallel computing.

The limitations of the system concern the global structure of samples. Clouds with a large number of outlying localisations (noise due to unspecific protein binding) require filtering. Single outlier points deteriorate cluster density statistics. Samples with multiple separate segments (cells or cell structures) require regionalisation, which is long-lasting. High calculation time are required for bootstrapped samples containing above 50 000 localisations.

Clustering based analyses of LM datasets opens up a unique parameter range for sample classification. We have shown that the designated parameters (like KS/WX p-values for cluster density and curvature similarity, and mean-cross values of the tests) are sufficient to correctly classify any data set of a selected population. With this, the newly developed 2CALM platform is well suited for a pairwise comparison of protein distributions in healthy, pharmaceutically treated tissues. Moreover, 2CALM is also suitable for a comparison and classification of protein distributions on any other cell type. The provided statistical tool is versatile, applicable for any pairwise LM dataset and provides an essential tool for shedding light on protein distributions, which are detectable only at a high-resolution level.

The sequential calculation of the Ripley's K-function for an incremental radius as presented by Owen et al. gives one global characteristic of the density distribution of sample clusters. In our case, as shown by simulations and exemplary experimental data (S13 Fig) in particular for samples presenting polarised fibrous structures like actin, such a global approach can give an ambiguous or false estimation of sample similarity. The Ripley's functions K and H in our analysis pipeline can be seen as auxiliary additional features, sharpening estimates for the probability of sample similarity using machine-learning methods.

Analysis systems such as SR-Tesseler [18] or ClusterVisu [19] are based on Voronoi tessellation show great potential for either visualization and rendering of localisation events density distribution in a sample or colocalization between two-color localisation events. It has been demonstrated for 2D datasets with relatively low numbers of localisations. The Voronoi tessellation cell represent the 'area of influence' for localisation inside a single cluster. This corresponds to building of density distribution from single-point clusters using hierarchical clustering with small size radius, e.g. 1 nm or 2 nm with our software. The single point cluster density determined by our software in nearest proximity to SR-Tesseler, can be regarded as invers area/volume of Voronoi cell. However, in this case the sample density distribution becomes very sensitive to the number of localizations. Additionally, the computation time is high for large samples.

The method proposed by Burguet et al. [96] is based on comparison of the intensities of points at local spatial positions within the samples [97]. The method requires normalization and correction of spatial data. That way all localisation positions in the samples are expressed in the same 2D / 3D coordinate system. Within this normalized coordinate system, the number of points and their positions may vary depending on the spatial structure of the sample, which creates variations in the analysis. The proposed solution is based on the local intensity estimator, which than creates an intensity map for each sample and tests for local intensity differences. Secondly, the method has up to now never been used for LM applications. In contrast to the algorithm developed by Burguet, our software does not require synchronization of the coordinate system and the size of the observed region (i.e. ROI) or possible normalization of both samples.

The interpretation of the methods typically requires a multimodal analysis. Nowadays, correlative approaches combining multiple methods are used. The main goal of this work is to establish a platform which is based on multiple parameters yielding one global answer on two-sample similarity (regardless of the rotation or shifting of the localizations cloud). The software

we developed however allows accessing the comparison data on each analysis detail-level and extract the information on similarity for each cluster dimension. This information can as complement information's derived from other nanoscopic imaging method like Atomic Force Microscopy (AFM) or Electron Microscopy (EM).

Methods

Equalization and bootstrap resampling

We use inferential statistics to examine the relationships between the features of two samples based on a series of smaller samples in order to generalize how those features will relate to the larger sample [67, 36, 68, 69, 98–103]. For analysis, we chose representative subsets of two samples, which will be referred to as the bootstrap-resamples. The bootstrap procedure involves choosing random samples (with replacement) from a large dataset and analysing each bootstrap sample in a similar way. Sampling with replacement means that each point is selected randomly from the original dataset. Thus, a particular point from the original dataset may appear multiple times in a given bootstrap sample. The number of total points included in a bootstrap sample (including data from both compared samples) is equal. Let N_1, N_2 be the number of points in both samples, respectively. We perform M times random resampling of each sample with the same number of points $N < min(N_1, N_2)$. Default values for $M = 100$ and N is ~2000–10 000 points. These bootstrap-samples $(bs^1(k), bs^2(k))(k = 1, \ldots, M)$ are pairwise stored for further analysis.

Spatial clustering via hierarchical clustering

Hierarchical clustering (also called Hierarchical Cluster Analysis (HCA)) is a common algorithm, which creates a hierarchy of clusters [49–52]. The agglomerative approach at the beginning declares each point as an individual cluster. Thus, pairs of clusters merge as one-element cluster moves up the hierarchy. Hierarchical clustering creates a cluster tree or dendrogram. This tree is a multi-level hierarchy with clusters of one level being joined to clusters in the next level. Grouping of the clusters into a tree connects pairs of clusters, which are close together by using a linkage function. The linkage function uses the distance information between points to determine the proximity of clusters relative to each other. Next, newly created clusters are grouped into larger clusters until a hierarchical tree is created. We apply a complete-linkage clustering function, which uses the maximum of the pairwise distances between points for clustering [51, 52].

For data partitioning, we cut the hierarchical tree into clusters with a given maximal cluster dimension/cluster size (maximal Euclidean distance between points inside a cluster); e.g. at the level of $d = dim(i)$, where $dim(i)$ is a vector of cluster dimensions, by pruning off branches from the bottom of the hierarchical tree, and assigning all the clusters below each cut to a single cluster.

The use of complete-linkage hierarchical clustering guarantees that agglomerated clusters have a dimension ($size^{Cluster}$) no greater than given $dim(i)$. In the hierarchical clustering process, cluster sizes $dim(i)$ are ordered sequentially from $size_{min}$ to $size_{max}$ with a constant Δ step. In order to find features that allow comparison between two samples, both samples are clustered sequentially with a given maximum cluster size $d = dim(i)$, where $dim(i) = size_{min} + i \cdot \Delta$, and $i = 1, \ldots, L$ and $L \cdot \Delta = size_{max}$.

For linkage, the $size_{max}$ for both clustered samples is assumed to be ~ 40% to 50% of the minimum dimension of both samples. The dimension of the sample can be defined as the minimum length of the 3D box, which includes all points of the sample. We set the $size_{min}$ between 5 nm-10 nm and the step Δ to be 10 nm as default values.

Cluster parameter extraction

The platform allows extraction of **6 sample-independent parameters:**

- *Cluster density*

- *Cluster curvature*

- *Average cluster density*

- *Average cluster curvature*

- *Ripley's K function*

- *Ripley's H function*

Let *Cl(d)* be the set of *N(d)* clusters for one of the samples (1 or 2) with the cluster maximum size $d = dim(i)$ (for sake of clarity, we will omit the *i* index from now on).

Cluster density

For each cluster c_k (where $k = 1...N(d)$) from the set Cl(d) one can calculate its density $dens_k = n_k \frac{1}{V_k}$ and relative density as $density_k = dens_k / density(sample)$, where n_k is the number of points in k^{th}-cluster from the set *Cl(d)*, V_k is its volume and the $density(sample) = \frac{N}{V}$ is the density of the whole sample.

The density of the cluster slightly depends on the method of determining its volume. The platform allows one to use three different methods to determine the cluster volume:

1. Sum of the sphere volumes with the sphere centre in each point of the cluster and the radius equal to the half-distance to the nearest neighbour (called bullet-density, S10E Fig) [84].

2. Volume of convex hull spread upon cluster points (called hull-density, S10F Fig).

3. Volume estimated as a volume of a rectangular box including cluster points (called box-density, S10G Fig).

As default, we use the bullet-density that best reflects the shape of the 3D cluster.

Cluster curvature

The value of the curvature reflects the concave-convex degree of the cluster surface. We use the method presented by He et al and Williams and Shah [82, 104] to estimate the curvature of the cluster by analysing the covariance between all cluster points. For a 3D cluster, we determine the covariance matrix of each point in a cluster based on a centroid calculation.

Let $pos_k = (x,y,z)_k$ be a matrix of the 3D point locations in a cluster c_k from the set *Cl(d)* and p_k be the centroid of these points. The pos_k is a c_k x 3 matrix. The 3D covariance matrix $COV_k = \Sigma_j (pos_k(j) - p_k) \cdot (pos_k(j) - p_k)^T$ where $j = 1,...,n_k$ is a semi-positive definite three-order symmetric matrix. Next, the three eigenvalues of the COV_k matrix $\lambda_1, \lambda_2, \lambda_3$ and its corresponding unit eigenvectors ev_1, ev_3, ev_3 are calculated. Let $\lambda_1 \leq \lambda_2 \leq \lambda_3$. Eigenvalue λ_1 describes the change of the value of the surface along the normal direction. The surface variation can be expressed as $\tau_k = \lambda_1 / (\lambda_1 + \lambda_2 + \lambda_3)$. The curvature $curv_k$ of the cluster c_k can be approximated as a surface variation τ_k [104].

Both features, densities and curvatures of clusters, can be used for first level comparison or detailed level sample comparison. The relative density and curvature of clusters with a given dimension *d* can be considered as empirical distributions with an unknown probability density

function (pdf). The empirical distributions of both samples can have a different number of elements (different number of clusters).

Based on these detailed distributions, we can also specify the global features of the clusters used later in the second level analysis. For each cluster size $d = dim(i)$, the two additional sample features can be determined:

Average density of clusters: $av\_density(d) = mean(density_k|k = 1,\dots,N(d))$
Average curvature of clusters: $av\_curv(d) = mean(curv_k|k = 1,\dots,N(d))$

3D Ripley's K-function and Ripley's H-function

Sequential clustering is simultaneously used to calculate the value of the Ripley's K-function for each sample [70, 86, 87]. Ripley's K-function is an intuitive approach for detection of deviations of general assumptions of point distributions within cluster samples. The analysis has a non-parametric character and is therefore the first step in the characterization of spatial point patterns. The K-function can be calculated for each size $d = dim(i)$ of clusters between given $size_{min}$ and $size_{max}$.

Let $Dist(l,k)$ denote the Euclidean 3D-distance matrix between each pair of points in the sample. An extension of the K-function from 2D to 3D is obtained by assuming 3-dimensional distance measures.

Thus, the **K**-function for a given distance $d = dim(i)$ is determined as

$$\boldsymbol{K}(d) = \frac{V}{N^2} \cdot \left(\sum_{k=1}^{n}\sum_{l \neq k} e_k(d) \cdot I[Dist(k,l) \leq d]\right) \tag{1}$$

where V is the volume of the sample, N is the number of sample points, $e_k(d)$ is the edge correction term for a sphere of radius d with k point as its center and $I[\cdot]$ is the indicator function [70]. The expected value of the complete spatial randomness (CSR) is $E[\boldsymbol{K}(d)] = 4\pi d^3/3$ as well as the function [86, 87]:

$$\boldsymbol{H}(d) = \sqrt[3]{3\boldsymbol{K}(d)/4\pi}\,d \tag{2}$$

Finally, for each sample, six features can be determined. The sample is sequentially divided into clusters with dimensions $dim(i) = size_{min}+i\cdot\Delta$. For each size $d = dim(i)$ the sample is represented by:

- Vector **density**(d) of the relative density of clusters for size d

- *Curvature vector* **curv**(d) of clusters for size d

- Value **av_density**(d) of average density of clusters

- Value **av_curv**(d) of average curvature of clusters

- Value **K**(d) of the Ripley's function

- Value **H**(d) of the Ripley's function

Using H-Ripley as the crucial dimension, representative for the largest difference (clustering caused) between the sample and complete spatial randomness can be determined.

Sample comparison based on extracted parameters

Regardless of whether comparisons are carried out on full samples or selected ROIs, we derive the above-described features for each given $d = dim(i)$. For every d, samples are compared using the results of the Ripley functions $\boldsymbol{K_1}$, $\boldsymbol{K_2}$ and $\boldsymbol{H_1}$, $\boldsymbol{H_2}$, density and curvature distributions

density₁, *density₂*, *curv₁*, *curv₂* clusters of samples 1 and 2, respectively. Cluster density distribution **density** and the distribution of cluster curvature **curv** are two random variables with an unknown probability density function.

1st-level analysis

For two cluster density distributions **density₁** *and* **density₂** originating from sample 1 and 2 the null hypothesis states that both distribution **density₁** *and* **density₂** belong to the same original distribution. To resolve the validity of this hypothesis at a given significance level α, we use two-sample Kolmogorov–Smirnov test [72–74].

Kolmogorov-Smirnov (KS) test compares empirical cumulative distribution functions based on their absolute differences. The null hypothesis is rejected at a significance level α in case the difference exceeds the critical value. The KS-test returns an asymptotic p-value as a scalar value in the range [0,1]. The p-value is the probability of observing a test statistic more extreme than the observed value under an assumption of a true null hypothesis. The asymptotic p-value becomes very accurate for large sample sizes and is reasonably accurate for sample sizes N_1 and N_2, such as $(N_1 N_2) / (N_1 + N_2) \geq 4$. Therefore, one can accept the p-value *pv* *(d) = testKS(**density₁**(d), **density₂**(d))* for each size *d* as one comparative variable.

The second null hypothesis assumes that both distributions **density₁** and **density₂** are taken from continuous distributions with equal medians. To resolve the validity of this hypothesis at a given significance level α, we can use the Wilcoxon rank-sum test (WX, Wilcoxon–Mann–Whitney test) [75, 76]. This non-parametric test is used to determine if two independent samples were selected from populations with equal distributions. The test assumes that the two samples are independent. A two-sided WX-test returns the p-value as a positive scalar in the range [0,1]. Data **density₁** and **density₂** can have different lengths.

Therefore, in addition to the p-value of the KS-Test, one can calculate the p- value *pw(d) = ranksum(**density₁**(d), **density₂**(d))* for each size *d* of the WX-test as the second comparative variable.

After calculating the p-values for both tests, one needs to aggregate both variables *pv* and *pw* for each size *d*. We apply the weighted t-norm-AND operator, which is often used in AND-aggregation in fuzzy logic [77, 78]. The weighted t-norm-AND operator calculates aggregated p-values as $pd = pv \bigwedge pw = 1 - \sqrt{w(1 - pv)^2 + (1 - w)(1 - pw)^2}$, where parameter *w* is a weight between 0 and 1 and allows to assign more significance to one of the tests. Default *w* is ~0.5–0.6.

The same method is applied to the clusters curvature distributions **curv₁** and **curv₂** with the given dimension *d*. As result, we obtain curves representing p-values **pv,pw,pd** for relative density and **pcv,pcw,pc** for curvature of clusters depending on the cluster size *d*. Additionally, the distribution-free multivariate KS-test allows for a comparison of the pair of distribution (**density₁**, **curv₁**) with the pair of distribution (**density₂**, **curv₂**) [72].

2nd-level analysis

The bootstrap technique provides M pairs of bootstrap samples $(bs^1(k), bs^2(k) | k = 1, ..., M)$. For each resampled pair, features are calculated based on the sequential clustering of both *bs* for each cluster size $d = \dim(i), i = 1...L$. For extracted features of each pair of *bs*, the above-described first level statistic tests are performed and the results are stored in a $L \times M$ matrix. The rows of the matrix are adequate to the cluster sizes and the columns represent the individual bootstrap samples. The values of the Ripley's K- and Ripley's H-functions of the bootstrap results are assigned to the matrices **KR** and **HR.** The p-values of the KS-test and the p-values of

WX-test for relative densities and curvature distribution in clusters are included in the matrices KD and KC, WD and WC, respectively. Additionally, the bootstrapping method stores the average values of relative clusters densities $av\_density$ and of the clusters curvatures av_curv into matrices DM and CM, for each dimension d of both samples.

Next, bootstrap confidence intervals are calculated. Having multiple realizations of random variables of density distribution and curvature distribution of clusters enables the estimation of confidence intervals for p-values generated by the KS- as well as the WX-test. Alternatively, for estimation of the standard parametric confidence intervals (of known distributions) we use the semiparametric or nonparametric methods with bootstrap estimates. Hence, the bootstrapping technique estimates the standard error deviation, which is used in a normal approximation of confidence intervals for significance level α (inaccurate estimation). For $\alpha = 0.05$ the normal confidence interval is approximated by $pd \pm 1.96 * std(pd)$. Alternatively, nonparametric *bootstrap percentile confidence intervals (BPCI)* can be calculated to infer the observed significance level of the variable. The bootstrap distributions of the p-values for each cluster size can be sorted, and α and $(1 - \alpha)$ percentiles of the sorted empirical distribution form the limits for the BPCI [98, 99, 102].

The comparative analysis of both samples is carried out on two levels: detailed (first level statistic) and global (second level statistic). At the detailed level, we use in the KD, KC, WD and WC matrices stored p-values of the KS-test and p-values of the Wilcoxon rank-sum test for comparison. In cases when $L = 1$ (whole sample), it is not possible to determine confidence intervals and the analysis is based only on the pd and pc curves and their aggregation with the t-norm AND-operator.

Having many realizations of random variables of densities and curvatures ($L > 1$), it is possible to carry out **cross tests** between the realizations as well as between their average values and Ripley functions. In addition to the previously described tests, we can directly calculate p-values (empirical p-values) between average values of the chosen variable of resamples from the first sample with all values of this variable in resamples from the second sample.

For the **global level** (second level statistic) comparison, we use additional matrices KR, HR (contain the values of Ripley's K and Ripley's H functions) and DM, CM of both series of resamples. The DM arrays (DM_1 and DM_2 –matrices of resampling series from sample 1 and sample 2, respectively) contain the average values of the relative cluster densities within a given dimension (rows) for each bootstrap sample (column). The CM (CM_1 and CM_2) matrices contain the average values of the cluster curvature with the given dimension (rows) for each resample (columns).

In order to compare the samples at this global level, we test two null hypotheses:

- **Mean-Cross-Hypothesis:** The average value of the mean cluster densities of all resample series determined from one original sample ($mean(DM_1)$) and all the resample distribution of mean densities determined from the second original sample ($mean(DM_2)$) originate from the same continuous distribution.

- **Cross-Hypothesis**: Randomly k-times chosen density distributions from one series of resamples (i[th]-column of matrix DM_1) and all the mean density distributions of the second resample series (DM_2) originate from the same continuous distribution.

A similar hypothesis can be made for matrices CM_1 and CM_2 containing average values of cluster curvatures. The same hypotheses can be formulated and tested for Ripley's function results (KR and HR matrices) for both samples. For both hypotheses, we calculated the empirical p-value with methods previously described.

Measure of similarity between samples

We determine one measure for sample similarity [105] using calculated p-value curves (for each cluster dimension). In cases of an unknown confidence interval (L = 1), we can only use the simplest method for calculation of a similarity factor between compared samples.

We use the average of the aggregated p-value ($mean(\boldsymbol{p})$) in significance level α and transform, it into a similarity measure as follows:

$$\boldsymbol{sim}_M = \begin{cases} mean(\boldsymbol{p})/2\alpha, & mean(\boldsymbol{p}) < \alpha \\ 1 - \alpha/(2 \cdot mean(\boldsymbol{p})), & otherwise \end{cases} \tag{3}$$

Based on confidence interval estimates, we can define an alternative measure of similarity: comparison of the intersection between the area below the critical boundary α and the lower confidence interval boundary of aggregated p-value curve.

Let $d_{interval} = [size_{min,} size_{max}]$ be the full length of the cluster sizes interval. Thus, $cr = \alpha * d_{interval}$ spans the critical area of the significant level α. The $intersec(\boldsymbol{p})$ is the intersection of the critical area cr and the area above the lower bound of the confidence interval of $\boldsymbol{p}$. The measure for the similarity is defined as:

$$\boldsymbol{sim}_L = 1 - \frac{intersec(\boldsymbol{p})}{cr} \tag{4}$$

The average value of the aggregated p-value and confidence intervals of p-values for each size of cluster (matrix rows) are used to calculate $\boldsymbol{sim}_M$ and $\boldsymbol{sim}_L$ values. For a $\boldsymbol{sim}_M$ and $\boldsymbol{sim}_L$ value between 0.45 and 0.55, the similarity of the samples is marginal.

Machine learning

We apply a machine learning method, namely MLP neural network as a classifier of similarity of samples [71, 79, 80] (S10H Fig). We train the MLP neural network with 11 input neurons and 20 neurons in a hidden layer with a hyperbolic tangent as activation function and two neuronal output nodes with a softmax activation function (S10H Fig). As a network training performance function, we use cross entropy measures [71]. This makes it possible to interpret the values of both outputs as a posteriori probability of samples similarity. Let us assume that we have carried out a Ripley functions and bootstrapping-based analysis of two samples and extracted features and tests on both analysis levels. We transform the results into a set of $L * M$ vectors, where L is the number of analysed sizes of clusters in $dim(i)$ and M the number of resampling processes. Each vector represents the result of tests and forms the input and output pattern of the MLP neural network.

Vector $\boldsymbol{Input} = (d,p1,\ldots,p10)$ and $\boldsymbol{Output} = [0,1]$ (similar) or = $[0,1]$ (dissimilar) where $\boldsymbol{d}$ is the cluster size, $\boldsymbol{p_1} = \boldsymbol{pv(d)}$ is the p-value derived from the KS-test for relative cluster densities, $\boldsymbol{p_2} = \boldsymbol{pw(d)}$ is the p-value derived from the WX-test for the relative cluster densities, $\boldsymbol{p_3} = \boldsymbol{pcv(d)}$ is the p-value derived from the KS-test for the curvatures of clusters, $\boldsymbol{p_4} = \boldsymbol{pcw(d)}$ is the p-value derived from the WX-test for the curvatures of clusters, $\boldsymbol{p_5} = \boldsymbol{mean\_cross_1}$ is the p-value derived from the cross-comparison of the average cluster densities between sample 1 and sample 2, $\boldsymbol{p_6} = \boldsymbol{mean\_cross_2}$ is the p-value derived from the cross comparison of average cluster densities between sample 2 and sample 1, $\boldsymbol{p_7} = \boldsymbol{c\_mean\_cross_1}$ is the p-value derived from the cross comparison of the average curvature of clusters between sample 1 and sample 2, $\boldsymbol{p_8} = \boldsymbol{c\_mean\_cross_2}$ is the p-value derived from the cross comparison of the average curvature of clusters between sample 2 and sample 1, $\boldsymbol{p_9} = \boldsymbol{R\_mean\_cross_1}$ is the p-value derived from the cross comparison via the Ripley K-function of sample 1 with sample 2, and $\boldsymbol{p_{10}} =$

$R\_mean\_cross_2$ is the p-value derived from the cross-comparison of Ripley K-function of sample 2 with sample 1. Output value is equal to [0,1] if the parameters describing the samples are similar or is [0,1] otherwise. For extraction of the proper network training set, K-Ripley and bootstrap tests of both sample groups are required. To get a full training set, we need to know a priori if the samples are similar or not.

Cluster visualisation

S11A and S11B Fig are showing 3D representations of platelet clusters. To obtain a graphic representation of 3D objects, the Delaunay triangulation method was used. The Delaunay triangulation allows one to visualise the selected individual clusters in two ways: as shown in S11C and S11D Fig with a set of spheres with the centre in each point of the cluster and the radius equal to the half-distance to the nearest neighbour. As the default value for the cluster dimension (size), the dimension at maximum of the H-Ripley function is chosen. The H-Ripley functions are used to detect the presence of clustering in the data [106, 107]. Since the H-Ripley function is often used to recognize clustering, a positive value of $H(d)$ indicates clustering over that spatial range whereas a negative value indicates dispersion. The value of d that maximizes $H(d)$ indicates the radius of maximal aggregation (i.e. the size of clusters which contains the most points per volume). Therefore, d can be chosen as a neighbourhood radius ρ in the DBSCAN clustering method. It is used to extract the main (primary) clusters from the samples. The platform enables display of these primary clusters in 3D (S11E Fig). It is also possible to determine the empirical probability distribution of densities (S11H Fig) and curvature (S11I Fig) of primary clusters for both samples and their comparison using the KS-test.

The comparative analysis was performed on a standard PC with CPU i7 Intel, 1.9 GHz, 8 logical processors and 16 GB of RAM. Total analysis time for one pair of resamples and for all cluster dimensions is dependent on the number of points in a resample: e.g. for 1000 points: 0.86 s, 5000 points: 6.61s and for 10000 points: 18.11s.

Statistics

Statistical analyses were performed using SPSS. All statistical tests are described in the Fig legends. Statistical significance value: $p < 0.05$.

Supporting information

S1 Methods. Supporting methods.
(PDF)

S1 Fig. Detailed statistical results on the comparison of CD41 and CD62p clusters. This figure shows the additional results regarding the statistical comparison for the two samples presented in **Fig 2** (sample 1 has $> 85\,000$ points and sample 2 has $> 93\,000$ points). (**a**) shows the direct comparison of the full samples (all localisations) via a KS-/WX-test of the cluster densities (top) and curvatures (bottom). (**b**) shows the aggregated KS-/WX-test p-values of curvature calculated with t-norm-AND operator of the results represented in (**a**). (**c**) displays the values of the KS-/WX-test and their aggregation via t-norm-AND operator determined from the cluster curvature distributions received from the bootstrap resampling (comparable to **Fig 2C**). (**d**) shows the bootstrapping results for cluster density and curvature (log, and normal scale). Herein, 100 resamples (all including 8 000 points) were plotted. Using the bootstrap method allows us to gain multiple testings required for the **second level analysis**. (**e**) presents a part of the **2nd-level analysis** and shows results on mean–cross comparison of the density and curvature distributions of resampled image data, respectively. (**f**) presents the aggregated

p-value for curvature and density comparison data at both analysis levels. (**g**) displays the results of the K-/H-Ripley functions for all bootstrap samples. (**h**) shows the KS-/WX-test results of the K-/H-Ripley data derived from both samples. On the left, the comparison of the K-functions values and on the right the comparison of the H-functions are presented. (**i**) shows the aggregated p-value for comparisons of K-/H-Ripley data.
(TIF)

S2 Fig. Workflow and parameters used for the comparative statistical analysis of the platform 2CALM. The figure depicts the flow diagram of the comparative analysis, including aggregation of parameters. In the first step, the sample data (full or bootstrap-resampled data of both samples) are clustered hierarchically for cluster dimensions (size) ranging from 10 nm– 1 000 nm. In the **first level analysis** of the pairwise resampled data, the Kolmogorov-Smirnov (KS)-/Wilcoxon (WX)-tests (relative density distribution/ curvature distribution) for each cluster dimension are performed. The KS- and WX-test results for comparison of cluster densities and curvatures of both (pairwise) samples are further aggregated using the t-norm-AND operator for all cluster dimensions. The results of p-value aggregation for density and curvature are once more aggregated, giving the average result of the comparison on the first statistical level. Next, the **second statistical level** analysis is performed. Here, the averaged density and curvature for each cluster dimension and resample are used to perform the mean-cross analysis between them. The mean-cross comparison uses KS-/WX-tests for a comparison between distributions of mean clusters density of all resamples from sample 1 and all individual density distributions of resamples from sample 2. Hence, an aggregation (t-norm AND operator) of the mean-cross KS/Wilcoxon-test results (p-values) for density and curvature for all cluster dimension gives a global p-value of similarity hypothesis. In parallel, in **the second level analysis** the K-/H-Ripley functions for all cluster dimensions are calculated. Hence, the mean-cross comparison on the K-/H-Ripley functions values, (same as for mean density/curvature distributions) is performed. The KS-/WX-Test results on comparison of the K-/H-Ripley function values are combined with t-norm AND, forming an additional set of parameters.
(TIF)

S3 Fig. Detailed statistical comparison of CD62p cluster distributions within two clots. CD62p was stained with Alexa647-labelled antibody. Both reconstructed images are depicted in (**a**) and (**b**) (samples include $> 93\,000$ and $>120\,000$ points, respectively). (**c**) shows an image of selected clusters (600 clusters per image) with a cluster dimension of 180 nm. For cluster representation, we used the Delaunay-triangulation method. (**d**) depicts two randomly chosen clusters.
(TIF)

S4 Fig. Detailed statistical comparison of CD62p cluster distributions within two clots. First level analysis is depicted in (**a-c**). (**a**) shows the detailed analysis of the full samples. Density and curvature distributions of all clusters for each cluster dimension were compared at one time using a KS-/WX-Test. The results indicate a similarity of clusters for all cluster dimensions. As an indicator, an aggregated p-value is determined using the weighting t-Norm-AND. The p-value (black dashed line) remains above the critical p-value area (orange bar) proving the similarity hypothesis for all cluster dimensions. The corresponding similarities are sim_M = 0.87/0.82 for density and curvature, respectively. (**b**) depicts the aggregated p-value calculated with the weighting t-Norm-AND (blue) and confidence interval (black dashed line). A value of sim_M = 0.82 is determined. The full-sample analysis does not give the full parameter range of the analysis, just a brief overview on cluster density and curvature similarity. (**d**) depicts 100 curves–representing relative density of 100-resamples each including 2000

points (green)–used for the bootstrap based comparison of the cluster/curvature density distribution for both samples. In black, the averaged values for all dimensions are represented. The detailed analysis for the bootstrap data shown in (**d**) was performed similarly to the analysis in (**a**). (**c**) shows the KS-/WX-test compared data regarding cluster density and curvature for all given cluster dimensions. As for the detailed analysis (**d**), the KS/WX-tests (blue/red) as well as the t-Norm-AND aggregated p-values are plotted (black). Additionally, the boundaries of the confidence interval are displayed (magenta). The comparative analysis of the bootstrap derived data shows a strong similarity between the samples (sim_M = 0.93 for cluster density, sim_M = 0.95 for curvature). (**e-i**) depict the **second level analysis**. (**e**) shows the generalized density/curvature p-values determined via a mean-cross comparison. Herein, p-values of the mean-cross comparison (blue) and lower/upper confidential boundaries (black dashed line) are shown. In general, a significance similarity between the samples is visible (sim_M = 0.92 for mean cluster density and sim_M = 0.94 for curvature distributions). (**h**) shows the aggregated p-values for cluster curvature and density distributions (blue). The aggregated p-values show high similarities sim_L = 1. (**f**) depicts the calculated Ripley's–K/-H function values for the boot-strapped data (green) for all cluster dimensions. Using H-Ripley´, the crucial dimension (representative for the largest difference (clustering-caused) between the sample and the Poisson distribution) can be determined (for the two images, the largest difference occurs for clusters sizes of 220 nm). (**g**) depicts the comparison of the K-/H-Ripley function values at a generalized level (second level statistics). The p-values of the mean-cross comparison (blue) and lower/upper confidential bounds (black dashed line) are shown. The cross-comparison of the statistical cluster-data analysis also indicates similarity of the samples. (**i**) shows the result of a pairwise KS-test on the distribution of average cluster density and distribution of average cluster curvature for both samples. We observe only a slight dissimilarity for cluster dimensions between 200 nm– 400 nm and 600 nm– 900 nm. This result confirms the similarity of both samples (sim_M = 0.58).
(TIF)

S5 Fig. Detailed statistical comparison of CD41 cluster distributions within two clots. In both samples, CD41 was stained with an Alexa488-labelled antibody. Both reconstructed images (include >158 000 and >142 000 points, respectively) are depicted in (a) and (b). (c) shows images of the clusters with the cluster dimension of 245 nm (600 clusters in each image). For cluster representation, we used the Delaunay-triangulation method. (d) depicts two randomly chosen clusters.
(TIF)

S6 Fig. Detailed statistical comparison of CD41 cluster distributions within two clots. First level analysis is displayed in the images (a-c). (**a**) shows the detailed analysis of the full samples (both samples reduced to 60 000 points) density (top) and curvature (bottom). In this case, density and curvature distributions of clusters for each cluster dimensions were compared at one time using the KS-/WX-test (blue/red). The results indicate a similarity of samples for all cluster dimensions. As an indicator, an aggregated p-value is determined using the weighting t-Norm-AND. The p-value (black dashed line) remains mostly above the critical p-value area (orange bar) proving the similarity hypothesis. The corresponding similarities are sim_M = 0.57/0.91 for the density and curvature distributions respectively. Remarkably, the density distribution shows a lower similarity compared to the curvature. A closer look at the comparison of the density distributions shows, that for small cluster dimensions between 10 nm and 150 nm as well as for large cluster dimensions ranging from approx. 1 400 nm– 1 800 nm, the distributions are within the critical p-value area. (**b**) depicts the aggregated p-value (density and curvature) calculated with the weighting t-Norm-AND (blue) and the confidence

interval (black dashed line). A sim_M = 0.71 is determined. For such large samples, a faster bootstrap-resampling is used. (**d**) depicts 100 curves–representing relative density of 100-resamples each including 2 000 points (green)–used for the bootstrap based comparison of the cluster/curvature density distribution for both samples. In black, the averaged curve is represented. The detailed analysis (first level statistics) of the bootstrapped samples (**d**) was performed using similar statistics as used in (**e**). (**c**) shows the detailed (first level statistic) comparison of the distributions of cluster density (top) and curvature (bottom) for all given cluster dimensions (sizes). For this analysis, the KS/WX- tests (blue/red) as well as the t-Norm-AND values are plotted (black). Additionally, the boundaries of the confidence interval are displayed (magenta). The bootstrap derived data shows a strong similarity between the samples, sim_M = 0.91 and 0.95 for cluster density and curvature distributions was determined. (**e-i**) depict the **second level analysis**. (**e**) shows the p-values determined by the mean-cross analysis of the average density (left)/curvature (right) values determined via bootstrapping. Herein p-values of the mean-cross comparison (blue) and lower/upper confidential boundaries (black dashed line) are shown. In general, as expected a huge similarity between the samples is visible, sim_M = 0.92 for the mean cluster density distribution and 0.97 for the mean curvature distribution was determined. (**h**) shows the aggregated p-values for the cluster mean cross comparison of curvature and the mean cross of density distributions (blue). The aggregated p-values show a high similarities; sim_M = 0.91 and sim_L = 1. (**f**) depicts the calculated K/-H-Ripley's-function values for the bootstrapped data (green) for all cluster dimensions. (**g**) depicts the comparison of the K-/H-Ripley function values (K-left, H-right). The p-values of the cross comparison (red), mean-cross comparison (blue) and lower/upper confidential bounds (black dashed line) are shown. This cross-comparison of the cluster-data also indicates a similarity of the samples for Ripley's function analysis. The aggregated p-value of the results of the K-/H-Ripley functions comparison (**i**), indicates a slight dissimilarity of the results for cluster dimensions (sizes) between 200 nm– 600 nm.
(TIF)

S7 Fig. Comparison of CD41 and CD62p cluster distributions within a clot. In one clot sample, CD41 was marked with an Alexa488-labelled antibody; in the other sample, CD62p was marked with an Alexa647-labelled antibody. We used our software platform to compare the two distributions of CD41 and CD62p molecules determined from the centres of two biological replicas of clots. Both reconstructed images are depicted in (**a**) and (**b**) (both reconstructed from approx. 300 000 localisation events). (**c**) shows the image of clusters with the cluster dimension of 235 nm (600 clusters in each image). For cluster representation, the Delaunay-triangulation method is used. (**d**) depicts two randomly chosen clusters.
(TIF)

S8 Fig. Comparison of CD41 and CD62p cluster distributions within a clot. First level analysis is displayed in the images (a-c). (**a**) shows the detailed analysis of the full samples. In this case, density (top) and curvature (bottom) distributions of all clusters for each cluster dimensions were compared at one time using a KS-/ WX-test (blue/red). The results indicate the dissimilarity of clusters for all cluster dimensions. As an indicator, an aggregated p-value of KS- and WX-test is determined using the weighting t-Norm-AND. The p-value (black dashed line) remains mostly below the critical p-value area (orange bar) disproving the similarity hypothesis. The corresponding values for (dis)similarity sim_M = 0.01/0.68 for the density and curvature distributions were determined respectively. A closer look at the KS-/WX-Test results on curvature comparison indicates that for cluster dimensions approx. 600 nm– 800 nm the distribution is above the critical p-value area (indicating similarity). (**b**) shows the aggregated p-value of density and curvature calculated with the weighting t-Norm-AND

(blue) and the confidence interval (black dashed line). A sim_M = 0.36 is determined. The full-sample analysis was only, additionally performed, in order to show the full software capabilities (results are typically not used for a multilayer analysis). For such large samples, the fast bootstrap resampling is used. The graphs (**c-d**) clearly show a general dissimilarity of the samples. (**d**) depicts 100 curves–representing relative density of 100-resamples each including 2000 points (green)–used for the bootstrap based comparison of the cluster/curvature density distribution for both samples. In black, the averaged curve is represented. The detailed analysis of the bootstrapped samples (**d**) was performed as described in (**a**). (**c**) shows the statistical comparison of the cluster density (top) and curvature data (bottom), determined from the bootstrap results. For such detailed analysis (**c**), KS/WX- tests (blue/red) as well as the t-Norm-AND values (black) are plotted. Additionally, the boundaries of the confidence interval are displayed (magenta). The statistical comparison of the bootstrap derived data shows a sim_M = 0.21/0.76 and sim_L = 0.11/0.4 for cluster density and curvature comparison, respectively. The data on cluster density as well as curvature however, shows a general dissimilarity of the samples. A similarity for cluster curvatures for the dimension ranges of approx. 200 nm– 400 nm and approx. 600 nm– 800 nm is observed. (**e-i**) depicts the **second level analysis**. (e) shows the p-values determined by the mean-cross analysis of the average density (left)/curvature (right) values determined via bootstrapping. Herein, p-values of the mean-cross comparison (blue) and lower/upper confidential boundaries (black dashed line) are shown. The sim_M = 0.01 and 0.61 and sim_L = 0.005/0.1 for cluster density and curvature comparison are determined respectively. In general, the data emphasizes the dissimilarity hypothesis, however, the data for curvature comparison indicates a significant similarity for approx. 400 nm– 500 nm and >900 nm cluster density ranges. (**h**) shows the aggregated p-values for cluster curvature and density comparison (blue). The aggregation of the p-values results in sim_L = 0.24, indicating a general dissimilarity. (**f**) depicts the calculated K-/H-Ripley function values for the bootstrapped data (green) for all cluster dimensions. Using H-Ripley as the crucial dimension, representative for the largest difference (clustering caused) between the sample and complete spatial randomness, can be determined (for the two images the largest difference occurs for clusters sizes of 210nm). (**g**) depicts the comparison of the K-/H-Ripley function (K-function left, H-function Right) values at the second statistical level. The p-values of the cross comparison (red), mean-cross comparison (blue) and lower/upper confidential boundaries (black dashed line) are shown. In contrast to all the data presented on single molecule clustering, the cross-comparison on the global analysis via Ripley's function indicates sample similarity (for clustering dimensions ranging between approx. 400 nm– 1 000 nm). Similar to the individual distributions, is the aggregation of the K-/H-Ripley functions results (**i**). The respective sim_M values for the Ripley's functions comparison are 0.86 (K-/H-Ripley) and 0.55 (aggregated). The values are contrary to the previously shown results obtained on direct cluster comparison, thus a similarity is indicated. The varying result emphasizes the importance of a multilevel statistical analysis.
(TIF)

S9 Fig. Detailed statistical comparison of interleukin-1β-treated and untreated platelets within a clot. Cells were labelled with Alexa647-labelled anti-CD62p-antibody. Images were taken at the edge of an artificial clot, where platelets are more sparsely distributed than within the clot. Therefore, segmentation (ROI extraction) is required. Here, we present a statistical comparative analysis of the full image, with sparsely distributed platelets and we compare the extracted regions. The full (not regionalized) sample analysis is depicted in the left column of the Fig (**a'-e'**), the ROI analysis on the right ((**a-e**); parts of the ROI analysis are included in Fig 3 in the main text). From the analysis, the advantage of segmentation (region extraction) is

clearly visible. The **first level analysis** of the comparison of the KS/WX- tests presented in (**a**) (and **Fig 3E**) and (**a'**) indicates a significant similarity for full images. For ROI-based comparison, density and curvature of the clusters shows similarity solely for cluster dimensions >700 nm (sim_M/sim_L = 0.47/0.31 and 0.45/0.24 for cluster density/curvature distributions, in contrast: sim_M/sim_L = 0.87/0.75 and 0.87/0.80 for a full sample). **Fig 3C** (main text) depicts two extracted regions of an untreated (upper) and IL-1β treated (lower) clot; a difference in the CD62p distribution can be observed. The divergence of the results between ROI and full image analysis is due to numerous small clusters, which are homogenously distributed in the images; in particular in the platelet-free area of the interleukin-1β treated clot. Not-cell-related signals add a significant additional cluster population, which is less significant within a ROI. For full image analysis, clusters for a specific cluster dimension originate from various regions due to hierarchical clustering, which influences the overall cluster density/curvature distribution. This is not the case for ROI-based analysis. Similar results can be observed for the **second level analysis**: the mean-cross comparison of the statistical data on cluster density and curvature show divergent results. As before, a dissimilarity for the ROI comparison is shown (sim_M/sim_L = 0.07/0.07 (**Fig 3F**) and 0.91/0.50 (**b, c**) for aggregated cluster density/curvature comparison, in contrast: sim_M/sim_L = 0.54/0.2 and 0.85/0.35 for cluster density/curvature comparison on a full sample (c')). The results are confirmed by the K-/H-Ripley's statistics. The mean-cross analysis of all values, shown in (**d, d'**), indicates that many platelets within the extracted clot regions are sparsely distributed. Again, solely K-/H-Ripley statistics determined for the extracted ROI's indicate a difference in CD62p protein secretion after interleukin 1β treatment (sim_M/sim_L = 0.03/0.01 and 0.04/0.01 for K-/H-Ripley comparison (ROI analysis), in contrast: sim_M/sim_L = 0.94/0.78 and 0.94/0.79 for K-/H-Ripley comparison on a full sample). (TIF)

S10 Fig. Filtering of 3D dSTORM images using DBSCAN, ROI extraction, graphical representation of protein clusters. Images are reconstructed from approx. 60 000 single localisations. Images are shown before (**a**) and after (**b**) filtering using DBSCAN. Reduction from 59 393 points to 51 323 points (red: negative z values, yellow: positive z values) was achieved by using ρ = 2 and $minP$ = 3. Points defined as outliers are filtered. (**c**) represents the sample image shown in (**a**) before region extraction (white box: large regions, red box: small regions). (**d**) shows the extracted region (region includes all points from original image). Cluster volume was calculated as sum of spheres (**e**), convex-hull volume (**f**) and box volume (**g**). (TIF)

S11 Fig. Comparison of different visualisation methods of clusters. Visualisation of clusters with a maximum size of 210 nm. (a) shows the 600 densest clusters of sample 1 and (b) the 600 densest clusters of sample 2. (c) depicts the triangulation-based representation of a cluster from the inset in (b). (d) shows the sphere packing-based representation of the chosen clusters. Visualisation of the primary clusters of sample 2, created with a neighbourhood radius of 250 nm. (e) depicts the largest primary clusters, (f) the triangulation-based representation of the largest cluster and (g) the sphere packing-based representation of the largest cluster. (h) shows the empirical probability density function (pdf) for density distribution of primary clusters. (i) shows the empirical pdf for curvature distribution of primary clusters. The red and blue curves in (h,i) represent the samples from (a) and (b), respectively. (TIF)

S12 Fig. Comparison of CD62p expression (mean cell intensity) of untreated and cytokine treated platelets. CD62p expression (detected as mean cell intensity (int.) of cells labelled with anti-CD62p-Alexa647) was significantly lower after 30 minutes of 10 ng/mL interleukin-1β

treatment (mean: 5219 +- 1856 counts; n = 88 compared to 3565 +- 1246 counts; n = 83; power: 0.94). These data show a statistically significant lower CD62p expression for IL1-β treated cells in 2D (i.e. on single spread platelets). The boxplot depicts the median and the first and third quantile and outliers.
(TIF)

S13 Fig. Comparison of randomly distributed (simulated) localisation events, platelets of different morphologies and the CD41 protein distribution in a reconstructed dSTORM image. (a) shows the distribution of CD62p labeled with Alexa647-antibody. (b) represents a randomly distributed point cloud (approx. 85 000 data points/image). (c) shows the comparison of the cluster densities distribution to Ripley's K-function distributions for all cluster dimensions between the simulated and CD62p datasets (black/blue line for cluster density/K-function, respectively). The lines depict the aggregated p-value of KS- and WX-test results. The test based on the Ripley's K-function classifies the samples as similar (similar for cluster sizes ranging from 5 nm to about 400 nm). In contrary, our classification estimates the samples as dissimilar, with the test based on the density distribution of clusters (similarity measure = 0). The MLP neural network classifies samples as dissimilar with a posteriori probability of 88%. (d) and (e) show a simulated polarized (randomly distributed) and unpolarised image respectively. (f) shows the comparison of clusters density/curvature distributions and Ripley's K-functions for all cluster dimensions between the simulated polarized and simulated unpolarized datasets (black/blue line for cluster density/K-function, respectively). The lines depict the aggregated p-value of KS- and WX-test results. The test based on the Ripley's K-function classifies the samples as dissimilar (similar for cluster sizes ranging from approx. 150 nm– 180 nm). Our classification estimates the samples as dissimilar, with the test based on the density distribution of clusters (similarity measure = 0). Three additional pairs of polarized and unpolarised samples have been compared, rendering a dissimilarity of 78.5%, 88.5% and 95.1%. (g) and (h) show reconstructed dSTORM images of Alexa647-phalloidin labelled actin skeleton of two individual platelets activated on a glass surface. The two platelets are comparable, in an early activation state. (i) depicts the comparison of the cluster densities and the Ripley's K-function distributions for all cluster dimensions between the datasets representing platelet cytoskeleton at a similar activation stage (black/blue line for cluster density/K-function respectively). The lines depict the aggregated p-value of KS- and WX-test results. The test based on Ripley's K-function classifies samples as strong dissimilar. Our analysis provides a correct classification of samples as similar, based on the density distribution of clusters (similarity measure = 0.86). The MLP neural network classifies samples as similar with a posteriori probability of 87%. (j) and (k) show reconstructed 3D dSTORM images of Alexa647-phalloidin labelled actin skeleton of two individual platelets activated on a glass surface. The two platelets are in two different activation states, (j) a late activation state and (k) an early activation stat. (l) shows the comparison of the cluster densities and of Ripley's K-function distributions for all cluster dimensions between the datasets representing localisation microscopy images of platelets in early and late activation state (black/blue line for cluster density/K-function respectively). In this case both tests based on the Ripley's K-function as well as on the cluster density distribution correctly classify the samples as dissimilar (similarity measure = 0.1). The MLP neural network classifies rather samples as dissimilar with a posteriori probability of 64%. The results clearly prove that our method is also capable to compare protein distributions that change over time induced by external factors at a single cell level. The axial range is represented by two colors: blue is below the focal plane and yellow above. The axial range is ± 500 nm.
(TIF)

S14 Fig. Comparison between the CD62p distribution in interleukin treated clots (large clot on the left side and a chosen region of interest on the right). First level statistics yields for the two samples similar cluster densities for all cluster dimensions ($sim_M = 0.85$) and for cluster curvatures ($sim_M = 0.32$). Similar values are obtained for a comparison of aggregated density and curvature values ($sim_M = 0.76$ and $sim_M = 0.85$). Dissimilarity for the H-/K-Ripley analysis can be observed ($sim_M < 0.2$). An MLP value of 0.66 proves the similarity of the samples. The detailed analysis directly shows the crucial dimensions and parameters, which best describe the differences between both samples. The results prove that the differences between large clusters as well as small ROIs (size ranges of individual cells) can be very precisely determined.
(TIF)

S1 Table. Statistical comparison (p-values) of CD41/CD62p pairwise comparisons. The table displays all statistical p-values determined from several chosen pairwise compared distributions of CD41/CD62p proteins in clots. Samples 1–4 are samples where CD41 has been stained with Alexa488-labelled anti-CD41-antibody and samples 5–6 are samples where CD62p was stained with Alexa647-labelled anti-CD62p-antibody.
(XLSX)

S2 Table. Statistical comparison (p-values) of CD62p upon IL-1β treatment. The table displays all statistical p-values determined from several chosen pairwise compared distributions of CD62p proteins in IL-1β treated/untreated clots. Samples 1–3 display the comparison of CD62p from IL-1β untreated samples (stained with Alexa488-labelled anti-CD41-antibody) and samples 4–5 show the comparison of CD62p from IL-1β treated samples.
(XLSX)

Author Contributions

Conceptualization: Markus Axmann, Janett Göhring, Jaroslaw Jacak.

Data curation: Sujitha Puthukodan.

Formal analysis: Sandra Mayr, Markus Axmann.

Funding acquisition: Jaroslaw Jacak.

Investigation: Sandra Mayr.

Methodology: Sandra Mayr, Fabian Hauser, Sujitha Puthukodan.

Project administration: Jaroslaw Jacak.

Software: Fabian Hauser, Jaroslaw Jacak.

Supervision: Markus Axmann, Janett Göhring, Jaroslaw Jacak.

Validation: Sandra Mayr, Fabian Hauser.

Visualization: Fabian Hauser.

Writing – original draft: Janett Göhring, Jaroslaw Jacak.

Writing – review & editing: Sandra Mayr, Fabian Hauser, Sujitha Puthukodan, Markus Axmann, Janett Göhring, Jaroslaw Jacak.

References

1. Sauer M. Localization microscopy coming of age: from concepts to biological impact. Journal of Cell Science. 2013; 126(16):3505–13. https://doi.org/10.1242/jcs.123612 PMID: 23950110

2. Stefan WH, Steffen JS, Mark B, Xiaowei Z, Rainer H, Martin JB, et al. The 2015 super-resolution microscopy roadmap. Journal of Physics D: Applied Physics. 2015; 48(44):443001.

3. Betzig E, Patterson GH, Sougrat R, Lindwasser OW, Olenych S, Bonifacino JS, et al. Imaging Intracellular Fluorescent Proteins at Nanometer Resolution. Science. 2006; 313(5793):1642–5. https://doi.org/10.1126/science.1127344 PMID: 16902090

4. GMG L. Surpassing the lateral resolution limit by a factor of two using structured illumination microscopy. Journal of Microscopy. 2000; 198(2):82–7. https://doi.org/10.1046/j.1365-2818.2000.00710.x PMID: 10810003

5. Klar TA, Hell SW. Subdiffraction resolution in far-field fluorescence microscopy. Optics letters. 1999; 24(14):954–6. Epub 2007/12/13. 62785 [pii]. https://doi.org/10.1364/ol.24.000954 PMID: 18073907.

6. Malkusch S, Heilemann M. Extracting quantitative information from single-molecule super-resolution imaging data with LAMA–LocAlization Microscopy Analyzer. Scientific Reports. 2016; 6:34486. https://doi.org/10.1038/srep34486 https://www.nature.com/articles/srep34486#supplementary-information. PMID: 27703238

7. Veeraraghavan R, Gourdie RG. Stochastic optical reconstruction microscopy–based relative localization analysis (STORM-RLA) for quantitative nanoscale assessment of spatial protein organization. Molecular Biology of the Cell. 2016; 27(22):3583–90. https://doi.org/10.1091/mbc.E16-02-0125 PMC5221590. PMID: 27307586

8. Lagache T, Grassart A, Dallongeville S, Faklaris O, Sauvonnet N, Dufour A, et al. Mapping molecular assemblies with fluorescence microscopy and object-based spatial statistics. Nature Communications. 2018; 9(1):698. https://doi.org/10.1038/s41467-018-03053-x PMID: 29449608

9. Borgmann DM, Mayr S, Polin H, Schaller S, Dorfer V, Obritzberger L, et al. Single Molecule Fluorescence Microscopy and Machine Learning for Rhesus D Antigen Classification. Scientific Reports. 2016; 6:32317. https://doi.org/10.1038/srep32317 https://www.nature.com/articles/srep32317#supplementary-information. PMID: 27580632

10. Dani A, Huang B, Bergan J, Dulac C, Zhuang X. Superresolution Imaging of Chemical Synapses in the Brain. Neuron. 2010; 68(5):843–56. https://doi.org/10.1016/j.neuron.2010.11.021 PMID: 21144999

11. Abdulreda MH, Rodriguez-Diaz R, Berggren P-O, Caicedo A. Three-dimensional colocalization analysis in immunostained sections of human pancreas. Nature Protocols. 2011.

12. Xu K, Zhong G, Zhuang X. Actin, Spectrin, and Associated Proteins Form a Periodic Cytoskeletal Structure in Axons. Science. 2013; 339(6118):452–6. https://doi.org/10.1126/science.1232251 PMID: 23239625

13. Ricci Maria A, Manzo C, García-Parajo MF, Lakadamyali M, Cosma Maria P. Chromatin Fibers Are Formed by Heterogeneous Groups of Nucleosomes In Vivo. Cell. 2015; 160(6):1145–58. https://doi.org/10.1016/j.cell.2015.01.054 PMID: 25768910

14. Spühler IA, Conley GM, Scheffold F, Sprecher SG. Super Resolution Imaging of Genetically Labeled Synapses in Drosophila Brain Tissue. Frontiers in Cellular Neuroscience. 2016; 10:142. https://doi.org/10.3389/fncel.2016.00142 PMC4880563. PMID: 27303270

15. Greenfield D, McEvoy AL, Shroff H, Crooks GE, Wingreen NS, Betzig E, et al. Self-Organization of the Escherichia coli Chemotaxis Network Imaged with Super-Resolution Light Microscopy. PLOS Biology. 2009; 7(6):e1000137. https://doi.org/10.1371/journal.pbio.1000137 PMID: 19547746

16. Foo YH, Spahn C, Zhang H, Heilemann M, Kenney LJ. Single cell super-resolution imaging of E. coli OmpR during environmental stress. Integr Biol (Camb). 2015; 7(10):1297–308. https://doi.org/10.1039/c5ib00077g PMID: 26156621.

17. Owen DM, Rentero C, Rossy J, Magenau A, Williamson D, Rodriguez M, et al. PALM imaging and cluster analysis of protein heterogeneity at the cell surface. Journal of Biophotonics. 2010; 3(7):446–54. https://doi.org/10.1002/jbio.200900089 PMID: 20148419

18. Levet F, Hosy E, Kechkar A, Butler C, Beghin A, Choquet D, et al. SR-Tesseler: a method to segment and quantify localization-based super-resolution microscopy data. Nature methods. 2015; 12 (11):1065–71. https://doi.org/10.1038/nmeth.3579 PMID: 26344046.

19. Andronov L, Orlov I, Lutz Y, Vonesch JL, Klaholz BP. ClusterViSu, a method for clustering of protein complexes by Voronoi tessellation in super-resolution microscopy. Sci Rep. 2016; 6:24084. https://doi.org/10.1038/srep24084 PMID: 27068792; PubMed Central PMCID: PMC4828638.

20. Lang T, Rizzoli SO. Membrane Protein Clusters at Nanoscale Resolution: More Than Pretty Pictures. Physiology. 2010; 25(2):116–24. https://doi.org/10.1152/physiol.00044.2009 PMID: 20430955.

21. Garcia-Parajo MF, Cambi A, Torreno-Pina JA, Thompson N, Jacobson K. Nanoclustering as a dominant feature of plasma membrane organization. Journal of Cell Science. 2014; 127(23):4995–5005. https://doi.org/10.1242/jcs.146340 PMID: 25453114

22. Jayo A, Conde I, Lastres P, Martínez C, Rivera J, Vicente V, et al. L718P mutation in the membrane-proximal cytoplasmic tail of beta 3 promotes abnormal alpha IIb beta 3 clustering and lipid microdomain coalescence, and associates with a thrombasthenia-like phenotype. Haematologica. 2010; 95 (7):1158–66. Epub 01/15. https://doi.org/10.3324/haematol.2009.018572 PMID: 20081061.

23. Calaminus SD, Thomas S, McCarty OJ, Machesky LM, Watson SP. Identification of a novel, actin-rich structure, the actin nodule, in the early stages of platelet spreading. Journal of thrombosis and haemostasis: JTH. 2008; 6(11):1944–52. https://doi.org/10.1111/j.1538-7836.2008.03141.x PMID: 18761725.

24. Höök P, Brito-Robinson T, Kim O, Narciso C, Goodson HV, Weisel JW, et al. Whole blood clot optical clearing for nondestructive 3D imaging and quantitative analysis. Biomed Opt Express. 2017; 8 (8):3671–86. https://doi.org/10.1364/BOE.8.003671 PMID: 28856043

25. Kita A, Sakurai Y, Myers DR, Rounsevell R, Huang JN, Seok TJ, et al. Microenvironmental Geometry Guides Platelet Adhesion and Spreading: A Quantitative Analysis at the Single Cell Level. PLOS ONE. 2011; 6(10):e26437. https://doi.org/10.1371/journal.pone.0026437 PMID: 22028878

26. Sakurai Y, Fitch-Tewfik JL, Qiu Y, Ahn B, Myers DR, Tran R, et al. Platelet geometry sensing spatially regulates α-granule secretion to enable matrix self-deposition. Blood. 2015; 126(4):531–8. https://doi.org/10.1182/blood-2014-11-607614 PMID: 25964667

27. Nguyen T-H, Palankar R, Bui V-C, Medvedev N, Greinacher A, Delcea M. Rupture Forces among Human Blood Platelets at different Degrees of Activation. Scientific Reports. 2016; 6:25402. https://doi.org/10.1038/srep25402 https://www.nature.com/articles/srep25402#supplementary-information. PMID: 27146004

28. Zhu S, Tomaiuolo M, Diamond SL. Minimum wound size for clotting: flowing blood coagulates on a single collagen fiber presenting tissue factor and von Willebrand factor. Integrative biology: quantitative biosciences from nano to macro. 2016; 8(8):813–20. https://doi.org/10.1039/c6ib00077k PMC4980166. PMID: 27339024

29. Kim OV, Litvinov RI, Alber MS, Weisel JW. Quantitative structural mechanobiology of platelet-driven blood clot contraction. Nature Communications. 2017; 8(1):1274. https://doi.org/10.1038/s41467-017-00885-x PMID: 29097692

30. Rönnlund D, Xu L, Perols A, Gad AKB, Eriksson Karlström A, Auer G, et al. Multicolor Fluorescence Nanoscopy by Photobleaching: Concept, Verification, and Its Application To Resolve Selective Storage of Proteins in Platelets. ACS Nano. 2014; 8(5):4358–65. https://doi.org/10.1021/nn406113m PMID: 24730587

31. Poulter NS, Pollitt AY, Davies A, Malinova D, Nash GB, Hannon MJ, et al. Platelet actin nodules are podosome-like structures dependent on Wiskott–Aldrich syndrome protein and ARP2/3 complex. Nature Communications. 2015; 6:7254. https://doi.org/10.1038/ncomms8254 https://www.nature.com/articles/ncomms8254#supplementary-information. PMID: 26028144

32. Mayr S, Hauser F, Peterbauer A, Tauscher A, Naderer C, Axmann M, et al. Localization Microscopy of Actin Cytoskeleton in Human Platelets. International Journal of Molecular Sciences. 2018; 19(4):1150. https://doi.org/10.3390/ijms19041150 PMID: 29641438

33. Poulter NS, Pollitt AY, Owen DM, Gardiner EE, Andrews RK, Shimizu H, et al. Clustering of glycoprotein VI (GPVI) dimers upon adhesion to collagen as a mechanism to regulate GPVI signaling in platelets. Journal of thrombosis and haemostasis: JTH. 2017; 15(3):549–64. Epub 02/16. https://doi.org/10.1111/jth.13613 PMID: 28058806.

34. Lickert S, Sorrentino S, Studt JD, Medalia O, Vogel V, Schoen I. Morphometric analysis of spread platelets identifies integrin alphaIIbbeta3-specific contractile phenotype. Sci Rep. 2018; 8(1):5428. https://doi.org/10.1038/s41598-018-23684-w PMID: 29615672; PubMed Central PMCID: PMC5882949.

35. Maturana D, Scherer S, editors. VoxNet: A 3D Convolutional Neural Network for real-time object recognition. 2015 IEEE/RSJ International Conference on Intelligent Robots and Systems (IROS); 2015 28 Sept.-2 Oct. 2015.

36. Zhirong W, Song S, Khosla A, Fisher Y, Linguang Z, Xiaoou T, et al., editors. 3D ShapeNets: A deep representation for volumetric shapes. 2015 IEEE Conference on Computer Vision and Pattern Recognition (CVPR); 2015 7–12 June 2015.

37. Brock A, Lim T, Ritchie JM, Weston N. Generative and Discriminative Voxel Modeling with Convolutional Neural Networks. arXiv e-prints [Internet]. 2016 August 01, 2016. Available from: https://ui.adsabs.harvard.edu/\#abs/2016arXiv160804236B.

38. Mitjavila-Garcia MT, Cailleret M, Godin I, Nogueira MM, Cohen-Solal K, Schiavon V, et al. Expression of CD41 on hematopoietic progenitors derived from embryonic hematopoietic cells. Development. 2002; 129(8):2003–13. PMID: 11934866

39. Frenette PS, Johnson RC, Hynes RO, Wagner DD. Platelets roll on stimulated endothelium in vivo: an interaction mediated by endothelial P-selectin. Proceedings of the National Academy of Sciences of the United States of America. 1995; 92(16):7450–4. https://doi.org/10.1073/pnas.92.16.7450 PMID: 7543682.

40. Zarbock A, Polanowska-Grabowska RK, Ley K. Platelet-neutrophil-interactions: Linking hemostasis and inflammation. Blood Reviews. 2007; 21(2):99–111. https://doi.org/10.1016/j.blre.2006.06.001 PMID: 16987572

41. Golebiewska EM, Poole AW. Platelet secretion: From haemostasis to wound healing and beyond. Blood reviews. 2015; 29(3):153–62. https://doi.org/10.1016/j.blre.2014.10.003 PMID: 25468720.

42. Merten M, Thiagarajan P. P-selectin in arterial thrombosis. Zeitschrift für Kardiologie. 2004; 93 (11):855–63. https://doi.org/10.1007/s00392-004-0146-5 PMID: 15568145

43. Blann AD, Nadar SK, Lip GYH. The adhesion molecule P-selectin and cardiovascular disease. European Heart Journal. 2003; 24(24):2166–79. https://doi.org/10.1016/j.ehj.2003.08.021 PMID: 14659768

44. Kim H-J, Kim P-K, Bae SM, Son H-N, Thoudam DS, Kim J-E, et al. Transforming growth factor-β–induced protein (TGFBIp/β ig-h3) activates platelets and promotes thrombogenesis. Blood. 2009; 114 (25):5206–15. https://doi.org/10.1182/blood-2009-03-212415 PMID: 19738031

45. Toyoda T, Isobe K, Tsujino T, Koyata Y, Ohyagi F, Watanabe T, et al. Direct activation of platelets by addition of CaCl2 leads coagulation of platelet-rich plasma. International Journal of Implant Dentistry. 2018; 4(1):23. https://doi.org/10.1186/s40729-018-0134-6 PMID: 30066050

46. Pluthero FG, Kahr WHA. Imaging Platelets and Megakaryocytes by High-Resolution Laser Fluorescence Microscopy. In: Gibbins JM, Mahaut-Smith M, editors. Platelets and Megakaryocytes: Volume 4, Advanced Protocols and Perspectives. New York, NY: Springer New York; 2018. p. 13–31.

47. Beaulieu LM, Lin E, Mick E, Koupenova M, Weinberg EO, Kramer CD, et al. Interleukin 1 Receptor 1 and Interleukin 1β Regulate Megakaryocyte Maturation, Platelet Activation, and Transcript Profile During Inflammation in Mice and Humans. Arteriosclerosis, thrombosis, and vascular biology. 2014; 34 (3):552–64. https://doi.org/10.1161/ATVBAHA.113.302700 PMC4070375. PMID: 24458711

48. Bester J, Pretorius E. Effects of IL-1β, IL-6 and IL-8 on erythrocytes, platelets and clot viscoelasticity. Scientific Reports. 2016; 6:32188. https://doi.org/10.1038/srep32188 PMID: 27561337

49. Gower JC. A Comparison of Some Methods of Cluster Analysis. Biometrics. 1967; 23(4):623–37. https://doi.org/10.2307/2528417 PMID: 6080200

50. Defays D. An efficient algorithm for a complete link method. The Computer Journal. 1977; 20(4):364–6. https://doi.org/10.1093/comjnl/20.4.364

51. Murtagh F. A Survey of Recent Advances in Hierarchical Clustering Algorithms. The Computer Journal. 1983; 26(4):354–9. https://doi.org/10.1093/comjnl/26.4.354

52. Day WHE, Edelsbrunner H. Efficient algorithms for agglomerative hierarchical clustering methods. Journal of Classification. 1984; 1(1):7–24. https://doi.org/10.1007/BF01890115

53. Rohringer S, Hofbauer P, Schneider KH, Husa A-M, Feichtinger G, Peterbauer-Scherb A, et al. Mechanisms of vasculogenesis in 3D fibrin matrices mediated by the interaction of adipose-derived stem cells and endothelial cells. Angiogenesis. 2014; 17(4):921–33. https://doi.org/10.1007/s10456-014-9439-0 PMID: 25086616

54. Heilemann M, van de Linde S, Schüttpelz M, Kasper R, Seefeldt B, Mukherjee A, et al. Subdiffraction-Resolution Fluorescence Imaging with Conventional Fluorescent Probes. Angewandte Chemie International Edition. 2008; 47(33):6172–6. https://doi.org/10.1002/anie.200802376 PMID: 18646237

55. Nahidiazar L, Agronskaia AV, Broertjes J, van den Broek B, Jalink K. Optimizing Imaging Conditions for Demanding Multi-Color Super Resolution Localization Microscopy. PLOS ONE. 2016; 11(7): e0158884. https://doi.org/10.1371/journal.pone.0158884 PMID: 27391487

56. Wolter S, Löschberger A, Holm T, Aufmkolk S, Dabauvalle M-C, van de Linde S, et al. rapidSTORM: accurate, fast open-source software for localization microscopy. Nature methods. 2012; 9:1040.

https://doi.org/10.1038/nmeth.2224 https://www.nature.com/articles/nmeth.2224#supplementary-information. PMID: 23132113

57. Mlodzianoski MJ, Schreiner JM, Callahan SP, Smolková K, Dlasková A, Šantorová J, et al. Sample drift correction in 3D fluorescence photoactivation localization microscopy. Optics express. 2011; 19 (16):15009–19. https://doi.org/10.1364/OE.19.015009 PMID: 21934862

58. Wang Y, Schnitzbauer J, Hu Z, Li X, Cheng Y, Huang Z-L, et al. Localization events-based sample drift correction for localization microscopy with redundant cross-correlation algorithm. Optics express. 2014; 22(13):15982–91. https://doi.org/10.1364/OE.22.015982 PMID: 24977854

59. Kanchanawong P, Waterman CM. Localization-based super-resolution imaging of cellular structures. Methods in molecular biology (Clifton, NJ). 2013; 1046:59–84. https://doi.org/10.1007/978-1-62703-538-5_4 PMID: 23868582.

60. Zessin PJ, Krüger CL, Malkusch S, Endesfelder U, Heilemann M. A hydrophilic gel matrix for single-molecule super-resolution microscopy. Optical Nanoscopy. 2013; 2(1):4. https://doi.org/10.1186/2192-2853-2-4

61. Huang B, Wang W, Bates M, Zhuang X. Three-dimensional super-resolution imaging by stochastic optical reconstruction microscopy. Science (New York, NY). 2008; 319(5864):810–3. Epub 01/03. https://doi.org/10.1126/science.1153529 PMID: 18174397.

62. Ester M, Kriegel H-P, Sander J, Xu X. A density-based algorithm for discovering clusters a density-based algorithm for discovering clusters in large spatial databases with noise. Proceedings of the Second International Conference on Knowledge Discovery and Data Mining; Portland, Oregon. 3001507: AAAI Press; 1996. p. 226–31.

63. Sander J. Generalized Density-Based Clustering for Spatial Data Mining: Herbert Utz Verlag, München; 1998.

64. Sander J, Ester M, Kriegel H-P, Xu X. Density-Based Clustering in Spatial Databases: The Algorithm GDBSCAN and Its Applications. Data Mining and Knowledge Discovery. 1998; 2(2):169–94. https://doi.org/10.1023/a:1009745219419

65. Deschout H, Shivanandan A, Annibale P, Scarselli M, Radenovic A. Progress in quantitative single-molecule localization microscopy. Histochemistry and cell biology. 2014; 142(1):5–17. Epub 04/20. https://doi.org/10.1007/s00418-014-1217-y PMID: 24748502.

66. Veeraraghavan R, Gourdie RG. Stochastic optical reconstruction microscopy-based relative localization analysis (STORM-RLA) for quantitative nanoscale assessment of spatial protein organization. Molecular biology of the cell. 2016; 27(22):3583–90. https://doi.org/10.1091/mbc.E16-02-0125 PMID: 27307586.

67. Ferguson TS. A Course in Large Sample Theory: New York: Routledge; 1996.

68. Sprent P, Smeeton NC. Applied Nonparametric Statistical Methods: CRC Press; 2007.

69. Hox JJ, Moerbeek Ma, van de Schoot Ra. Multilevel analysis: techniques and applications. 3rd ed. ed: New York: Routledge; 2017.

70. Ripley BD. Spatial statistics / Brian D. Ripley. New York: Wiley; 2005.

71. Ripley BD. Pattern Recognition and Neural Networks. Cambridge: Cambridge University Press; 2007.

72. Massey FJ. The Kolmogorov-Smirnov Test for Goodness of Fit. Journal of the American Statistical Association. 1951; 46(253):68–78. https://doi.org/10.2307/2280095

73. Sheskin DJ. Handbook of Parametric and Nonparametric Statistical Procedures: Chapman \& Hall/ CRC; 2003. 1776 p.

74. D.I. F, G.W. C. Nonparametric Statistics: A Step-by-Step Approach: John Wiley & Sons; 2014.

75. Wilcoxon F. Individual Comparisons by Ranking Methods. Biometrics Bulletin. 1945; 1(6):80–3. https://doi.org/10.2307/3001968

76. Fay MP, Proschan MA. Wilcoxon-Mann-Whitney or t-test? On assumptions for hypothesis tests and multiple interpretations of decision rules. Statistics surveys. 2010; 4:1–39. https://doi.org/10.1214/09-SS051 PMID: 20414472.

77. Klement EP, Mesiar R, Pap E. Triangular Norms: Dordrecht: Kluwer; 2000.

78. Beg I, Ashraf S. Similarity measures for fuzzy sets. Applied and computational mathematics. 2009; 8 (2)(2):192–202.

79. Looney CG. Pattern recognition using neural networks: theory and algorithms for engineers and scientists: Oxford University Press, Inc.; 1997. 458 p.

80. Windeatt T. Accuracy/Diversity and Ensemble MLP Classifier Design. IEEE Transactions on Neural Networks. 2006; 17(5):1194–211. https://doi.org/10.1109/TNN.2006.875979 PMID: 17001981

81. Ben-Shabat Y, Lindenbaum M, Fischer A. 3D Point Cloud Classification and Segmentation using 3D Modified Fisher Vector Representation for Convolutional Neural Networks. CoRR. 2017.

82. He Y, Liang B, Yang J, Li S, He J. An Iterative Closest Points Algorithm for Registration of 3D Laser Scanner Point Clouds with Geometric Features. Sensors (Basel, Switzerland). 2017; 17(8):1862. https://doi.org/10.3390/s17081862 PMID: 28800096.

83. Boissonnat J-D, Geiger B, editors. Three-dimensional reconstruction of complex shapes based on the Delaunay triangulation. IS&T/SPIE's Symposium on Electronic Imaging: Science and Technology; 1993: SPIE.

84. Golias NA, Dutton RW. Delaunay triangulation and 3D adaptive mesh generation. Finite Elements in Analysis and Design. 1997; 25(3):331–41. https://doi.org/10.1016/S0168-874X(96)00054-6.

85. Conway JH, Sloane NJA, Bannai E. Sphere-packings, lattices, and groups: Springer-Verlag; 1993.

86. Jafari-Mamaghani M, Andersson M, Krieger P. Spatial Point Pattern Analysis of Neurons Using Ripley's K-Function in 3D. Frontiers in Neuroinformatics. 2010; 4(9). https://doi.org/10.3389/fninf.2010.00009 PMID: 20577588.

87. Hansson K, Jafari-Mamaghani M, Krieger P. RipleyGUI: software for analyzing spatial patterns in 3D cell distributions. Frontiers in Neuroinformatics. 2013; 7(5). https://doi.org/10.3389/fninf.2013.00005 PMID: 23658544

88. Kolmogorov AN. On the empirical determination of a distribution function. Giornale dell'Instituto Italiano degli Attuari. 1933; 4:83–91.

89. Nishimura S, Manabe I, Nagasaki M, Kakuta S, Iwakura Y, Takayama N, et al. In vivo imaging visualizes discoid platelet aggregations without endothelium disruption and implicates contribution of inflammatory cytokine and integrin signaling. Blood. 2012; 119(8):e45–e56. https://doi.org/10.1182/blood-2011-09-381400 PMID: 22096246.

90. Stalker TJ, Traxler EA, Wu J, Wannemacher KM, Cermignano SL, Voronov R, et al. Hierarchical organization in the hemostatic response and its relationship to the platelet-signaling network. Blood. 2013; 121(10):1875–85. https://doi.org/10.1182/blood-2012-09-457739 PMID: 23303817.

91. Heijnen HFG, Schiel AE, Fijnheer R, Geuze HJ, Sixma JJ. Activated Platelets Release Two Types of Membrane Vesicles: Microvesicles by Surface Shedding and Exosomes Derived From Exocytosis of Multivesicular Bodies and · -Granules. Blood. 1999; 94(11):3791–9. PMID: 10572093

92. Erlandsen SL, Bittermann AG, White J, Leith A, Marko M. High-resolution CryoFESEM of Individual Cell Adhesion Molecules (CAMs) in the Glycocalyx of Human Platelets: Detection of P-selectin (CD62P), GPI-IX Complex (CD42a/CD42bα,bβ), and Integrin GPIIbIIIa (CD41/CD61) by Immunogold Labeling and Stereo Imaging. Journal of Histochemistry & Cytochemistry. 2001; 49(7):809–19. https://doi.org/10.1177/002215540104900702 PMID: 11410606

93. Fatisson J, Mansouri S, Yacoub D, Merhi Y, Tabrizian M. Determination of surface-induced platelet activation by applying time-dependency dissipation factor versus frequency using quartz crystal microbalance with dissipation. Journal of The Royal Society Interface. 2011; 8(60):988–97. https://doi.org/10.1098/rsif.2010.0617 PMID: 21247945

94. Brown GT, Narayanan P, Li W, Silverstein RL, McIntyre TM. Lipopolysaccharide stimulates platelets through an IL-1β autocrine loop. Journal of immunology (Baltimore, Md: 1950). 2013; 191(10):5196–203. Epub 09/30. https://doi.org/10.4049/jimmunol.1300354 PMID: 24081990.

95. Charles RQ, Su H, Kaichun M, Guibas LJ, editors. PointNet: Deep Learning on Point Sets for 3D Classification and Segmentation. 2017 IEEE Conference on Computer Vision and Pattern Recognition (CVPR); 2017 21–26 July 2017.

96. Burguet J, Andrey P. Statistical comparison of spatial point patterns in biological imaging. PLoS One. 2014; 9(2):e87759. https://doi.org/10.1371/journal.pone.0087759 PMID: 24505311; PubMed Central PMCID: PMC3914854.

97. Syrjala SE. A Statistical Test for a Difference between the Spatial Distributions of Two Populations. Ecology. 1996; 77(1):75–80. https://doi.org/10.2307/2265656

98. Efron B, Tibshirani R. Bootstrap Methods for Standard Errors, Confidence Intervals, and Other Measures of Statistical Accuracy. Statist Sci. 1986; 1(1). https://doi.org/10.1214/ss/1177013817

99. DiCiccio TJ, Efron B. Bootstrap confidence intervals. Statist Sci. 1996; 11(3):189–228. https://doi.org/10.1214/ss/1032280214

100. Hjorth J. Computer Intensive Statistical Methods: New York: Routledge; 1994.

101. Hollander M, Wolfe D. Nonparametric Statistical Methods, 2nd Edition: Wiley-Interscience; 1999.

102. Carpenter J, Bithell J. Bootstrap confidence intervals: when, which, what? A practical guide for medical statisticians. Statistics in Medicine. 2000; 19(9):1141–64. https://doi.org/10.1002/(sici)1097-0258(20000515)19:9<1141::aid-sim479>3.0.co;2-f PMID: 10797513

103. Chaubey YP. Resampling-Based Multiple Testing: Examples and Methods for p-Value Adjustment. Technometrics. 2012; 35(4):450–1.

104. Williams DJ, Shah M. A Fast algorithm for active contours and curvature estimation. CVGIP: Image Understanding. 1992; 55(1):14–26. https://doi.org/10.1016/1049-9660(92)90003-L.

105. Yang W, Yan H, Li J. Formula for calculating spatial similarity degrees between point clouds on multi-scale maps taking map scale change as the only independent variable. Geodesy and Geodynamics. 2015; 6(2):113–25. https://doi.org/10.1016/j.geog.2015.03.002.

106. Sengupta P, Van Engelenburg S, Lippincott-Schwartz J. Visualizing cell structure and function with point-localization superresolution imaging. Developmental cell. 2012; 23(6):1092–102. https://doi.org/10.1016/j.devcel.2012.09.022 PMID: 23237943.

107. Deschout H, Zanacchi FC, Mlodzianoski M, Diaspro A, Bewersdorf J, Hess ST, et al. Precisely and accurately localizing single emitters in fluorescence microscopy. Nature methods. 2014; 11:253. https://doi.org/10.1038/nmeth.2843 https://www.nature.com/articles/nmeth.2843#supplementary-information. PMID: 24577276

Real-time 3D single-molecule localization microscopy analysis using lookup tables

Fabian Hauser[1,2,*] and Jaroslaw Jacak[1,2]

[1] *University of Applied Sciences, Upper Austria School of Medical Engineering and Applied Social Sciences, Garnisonstraße 21, 4020 Linz, Austria*
[2] *Austrian Cluster for Tissue Regeneration, Vienna 1200, Austria*
[*] *fabian.hauser@fh-linz.at*

Abstract: Herein, we present a new algorithm for real-time analysis of 3D single molecule localization microscopy images with a small impact on fitting accuracy using lookup-tables with discrete xyz-positions. The algorithm realizes real-time visualization during acquisition. We demonstrate its performance on simulated and measured data. Additionally, combining real-time fitting with a feedback loop controlling the activation laser pulse keeps the number of emitters per image frame constant.

1. Introduction

In recent years, Single Molecule Localization Microscopy (SMLM) has gained popularity due to commercially available whole-packaged systems and a wide range of freely available analysis software. In particular, direct Stochastic Optical Reconstruction Microscopy (dSTORM [1]) using photoswitching of fluorophores with a single laser wavelength and allowing modulation of the Point Spread Function (PSF), enables 3D applications by extracting the axial position from the signal's shape [2–5].

Typically, tens of thousands of images are required to reconstruct a single super-resolved image. Only a random subpopulation of sparsely distributed fluorophores is observable in each frame. Sparsity is needed to distinguish among emitters to enable precise localization. During the analysis, each frame is post-processed to obtain subpixel position of the fluorescence signal. Nevertheless, there are disadvantages if the images are analyzed after acquisition: (i) analysis of image stacks is time-consuming and can take up to tens of minutes depending on the amount of frames and emitters per frame, (ii) several parameters such as illumination time, laser power, pH-value, density of active fluorophores, and photo-switching cycle times influence blinking quality [6–8]. The impact of these parameters can only be evaluated after experimental data is analyzed. In contrast, using real-time SMLM analysis, some of these parameters can be adjusted during the acquisition phase to obtain an optimal emitter density per frame, e.g. by using an additional ultraviolet (UV) laser pulse which reactivates fluorophores from their dark-state. Many software packages already offer real-time analysis of SMLM data through the use of either multiple central processing unit (CPU) cores/threads [9], graphics card acceleration (using graphics processing unit (GPU)) [10–14] or experimental PSFs [15] in combination with a CPU and GPU. However, high-end CPUs/GPUs are expensive and/or are often not available on the computer used for the measurement.

In this paper, we present a real-time SMLM algorithm, which only requires a single CPU core to perform fitting of up to 600 astigmatic single emitters within 9.8 ± 0.5 milliseconds (ms) per frame – achieved by using a lookup table generated prior to the experiment. We verified our algorithm with simulated data, tested it on tubulin-like simulations from the SMLM challenge 2016 [16] and compared it to published results of the challenge. Our algorithm scored

at mid-field with an efficiency of 61%. We further tested our algorithm on simulations of 3D Siemens star-shaped test patterns [10]. Likewise, our algorithm localizes emitters at different axial positions; only extremely fine structures with axial positions below z < −400 nm were not detectable. Additionally, we tested the algorithm on data obtained from fixed biological samples and imaged the actin distribution in human endothelial cells and human platelets. Finally, we compared the spatial and temporal performance of our algorithm with our continuous least-squares fitting algorithm (3D STORM Tools [17]) as well as the optical resolution of the rendered localization microscopy images using Fourier Ring Correlation (FRC). Our real-time lookup table algorithm only requires on average 2.5 ± 0.6 ms to analyze an image frame while at the same time using only a single CPU core. This short analysis time allows for rendering of the SMLM image in real-time and for control of the number of active fluorophores per frame using an activation laser pulse.

2. Materials and methods

2.1. Real-time fitting of diffraction limited signal of fluorescent emitters

Our algorithm is based on a lookup table generated prior to the experiment. First, the lookup table is populated with template images of a PSF model at discrete lateral/axial positions and their derivatives $\partial PSF(x, y, z)/\partial x$, $\partial PSF(x, y, z)/\partial y$, $\partial PSF(x, y, z)/\partial z$ needed for fitting (see Visualization 1 for a movie of a populated lookup table). Hereby, any PSF model can be chosen as long as the PSF and first derivatives exist. For example, we use a 2D elliptical Gaussian function (Eqs. 1 & S1-S2 in Supplement 1). Here, φ is the clockwise rotation of the 2D Gaussian model, $\sigma_x(z)$ and $\sigma_y(z)$ are values of the fitted calibration using cubic B-spline [18]. The parameters *x*- and *y-position* are varied over a range of $r_{xy} = 4$ pixels around the center of the template image using $\Delta xy = 0.1$ pixels steps. Next, the elliptical Gaussian shapes (retrieved from calibration) representing axial positions of emitters are varied over a range of $r_z = 1000$ nm in $\Delta z = 25$ nm steps. At each discrete position of the lookup table, the PSF model and derivatives are calculated at each ith and jth pixel inside a 9×9 pixels template image. A lookup table with the parameters *window size* = 9 pixels, $\Delta xy = 0.1$ pixels, $r_{xy} = 4$ pixels, $\Delta z = 25$ nm, $r_z = 1000$ nm uses 263 MB of RAM with double precision values and 106 641 unique template images (each 4-dimensional pixel of the template image contains the PSF and their first derivatives of xyz).

$$PSF_{i,j}(x, y, z, \varphi) = \exp\left(-\frac{[(i-x)\cos(\varphi) + (j-y)\sin(\varphi)]^2}{2\sigma_x(z)^2} - \frac{[-(i-x)\sin(\varphi) + (j-y)\cos(\varphi)]^2}{2\sigma_y(z)^2}\right) \quad (1)$$

In order to find localization candidates, a modified Non-Maximum Suppression (NMS) algorithm [19] is used. The NMS algorithm is modified in a way that a mean of nine pixels which surround an identified maxima was used to suppress non-maxima, and not as usually a single pixel [19]. Next, the local background is calculated by averaging the pixel intensities along a square boundary line of a predefined window (e.g. 10×10 pixels). By comparing these values with a predefined intensity threshold, the chance of finding a wrong maximum is further decreased. Each fit is performed in a window surrounding the identified candidate, the window size matched the template images from the lookup table. Our recent NMS implementation is not suited for overlapping emitters. Therefore, our experiments are designed to have the smallest possible amount of overlapping emitters.

For fitting, we use an iterative Gauss-Newton algorithm to minimize the parameters of our discrete model: the parameters θ_{bg} (mean background signal), θ_p (maximum intensity) are unconstrained and the parameters $\theta_x, \theta_y, \theta_z$ are constrained by the discrete positions used by

the lookup table. The least-square (LS) minimization method is chosen instead of maximum-likelihood estimator (MLE) [20], since only the first derivatives are required. In order to find the best fit for a single emitter, we first define a window around the candidate's position matching the window size of the lookup table's template. Next, we calculate the Jacobian matrix elements $J_{i,j}$ (Eq. (2)) at every position within the window based on the template at the proposed position from the initial vector $\overrightarrow{\theta} = (\theta_{bg}, \theta_p, \theta_x, \theta_y, \theta_z)$. The initial values of θ_{bg} and θ_p are derived from the candidate search of the modified NMS algorithm and $\theta_x, \theta_y, \theta_z$ are initialized to fixed values (θ_x, θ_y to the center of the fitting window and θ_z to the focal plane with maximum focus found during calibration).

$$J_{i,j}(\overrightarrow{\theta}, k) = \begin{pmatrix} 1 \\ PFA_{i,j}^{(LUT)}(k) \\ \theta_p \frac{\partial PFA_{i,j}^{(LUT)}(k)}{\partial \theta_x} \\ \theta_p \frac{\partial PFA_{i,j}^{(LUT)}(k)}{\partial \theta_y} \\ \theta_p \frac{\partial PFA_{i,j}^{(LUT)}(k)}{\partial \theta_z} \end{pmatrix} \tag{2}$$

We calculate the index $k(\theta_x, \theta_y, \theta_z)$ of the template image in the lookup table using positions $\theta_x, \theta_y, \theta_z$. Based on the obtained index, we subtract the scaled and offset model from the observed data ($I_{i,j}$) within the candidate window to get the residual vector $r_{i,j}$:

$$r_{i,j}(\overrightarrow{\theta}, k) = I_{i,j} - (\theta_{bg} + \theta_p \cdot PFA_{i,j}^{(LUT)}(k)) \tag{3}$$

We use the LAPACK (Linear Algebra Package) library [21] to speed up calculation for finding the next parameters (Eq. (4)), especially **syrk** (symmetrical rank-k matrix multiplication) for $J^T J$ and **trsv** (solves for a triangular system of equations) to solve the equation system for $(J^T J)^{-1} Jr$.

$$\overrightarrow{\theta}^{(s+1)} = \overrightarrow{\theta}^{(s)} + (J_{i,j}^T J_{i,j})^{-1} J_{i,j} r_{i,j} \tag{4}$$

Since $J^T J$ is a symmetrical matrix, it is faster to solve the equation system directly from the triangular matrix rather than to perform a Cholesky decomposition [22] with consequently solving the equation system. Next, the parameters $\overrightarrow{\theta}^{(s+1)}$ are tested for convergence. For further iterations, the parameters $\theta_x, \theta_y, \theta_z$ are rounded to the next valid step based on the lookup table parameters Δxy and Δz, hence the index $k(\theta_x, \theta_y, \theta_z)$ is updated. These calculations (Eq. (4)) are repeated until either the maximum number of iterations is reached, θ_x, θ_y are outside of r_{xy}, θ_z is outside of r_z, or convergence is reached.

2.2. Human platelet concentrates

All human blood samples were collected during routine plateletpheresis in accordance with the strict policies of the Red Cross Transfusion Service, Linz, Austria. All blood donors signed informed consents stating that residual blood material could be used for research and development purposes. All experimental protocols were approved by and carried out in collaboration with the Red Cross Blood Transfusion Service. Single donor platelet concentrates were provided by the Red Cross Blood Transfusion Service. Platelet concentrates were prepared by apheresis with an automated cell separator (Trima Accel Automated Blood Collection System, TerumoBCT, Lakewood, CA, USA) during routine plateletpheresis: platelets were separated from whole blood by centrifugation and diluted in 35% plasma, 65% platelet additive solution SSP+ (Macopharma, Mouvaux, France), and ACD-A anticoagulant (Haemonetics anticoagulant citrate dextrose solution, Haemonetics, Braintree, MA, USA) during the transfer into Trima Accel storage bags. Two milliliters of the platelet concentrate (typically containing 1×10^6 platelets/µL) were

transferred to a new storage bag and immediately transported to the laboratory. Transportation within a polystyrene box minimized temperature variations. Platelets were used for experiments within 24 h after preparation and stored under constant agitation in a climatic chamber that was set to 22 °C.

2.3. Platelet staining

Platelets were diluted to a final concentration of 2×10^4 cells/mL in cell culture medium (DMEM, Sigma-Aldrich, Vienna, Austria) and were allowed to settle on a glass slide for 15 min. Non-adherent cells were washed away with Phosphate-Buffered Saline (PBS). Actin cytoskeleton was visualized using Alexa Fluor 647 phalloidin (Cell Signaling Technology, Leiden, The Netherlands) in a Cytoskeleton Buffer with Sucrose (CBS) containing 10 mM MES pH 6.1, 138 mM KCl, 3 mM $MgCl_2$, 2 mM EGTA, and 0.32 M sucrose according to a protocol from Louise Cramer [23] (MRC Laboratory for Molecular Cell Biology, UCL, London, UK). Briefly, platelets were fixed using 4% paraformaldehyde in CBS for 20 min at room temperature, then permeabilized using 0.5% Triton X-100 with CBS, blocked in 10% chicken-egg-white-albumin (Sigma-Aldrich, Vienna, Austria) and stained for 20 min with 66 nM Alexa Fluor 647 conjugated to phalloidin.

2.4. Human endothelial cells CD34$^+$-EC

Primary human Endothelial cells (phECs) were differentiated from CD34$^+$ cells isolated from human cord blood as previously described [24] and were provided in frozen aliquots of 1 million cells at passage 5 by Prof. Gosselet, Université d´Artois, France. After thawing, cells were seeded onto gelatine (0.2% in PBS) coated 10 cm-dishes in ECM-5 medium (ECM from Sciencell with 5 mL of Endothelial cell growth supplement (ECGS), 2.5 mL of Gentamycin 10 mg/mL (BiochromAG, Ref. A-2712) and 25 mL of pre-selected, heat-inactivated FBS; and cultivated at 37 °C, 5% CO_2. When cells reached confluency, they were washed three times with PBS, detached with Trypsin/EDTA solution, counted and re-seeded at a concentration of ~20 000 cells/cm^2. Expression of EC marker CD31 was confirmed by flow cytometry and immunofluorescence.

2.5. Endothelial cell staining

Cells were split and seeded at approximately 20 000 cells/cm^2 into Nunc Lab-Tek II Chambered Coverglasses (Thermo Fisher Scientific Inc, MA, USA). Next, cells were washed with pre-warmed HBSS (containing Mg^{2+} and Ca^{2+}) at 37 °C. The actin cytoskeleton was visualized using Alexa Fluor 647 phalloidin (Cell Signaling Technology, Leiden, Netherlands). Staining of the cells was conducted in CBS as described in the platelet staining section.

2.6. Fluorescence microscope

Images were acquired using a modified Olympus IX81 inverted epifluorescence microscope with an oil-immersion objective (PlanApo N 60x/1.42 NA, Olympus, Vienna, Austria) as well as an additional tube-lens with a magnification of 1.6x. The sample was positioned on a XYZ piezo stage (200 μm x 200 μm x 200 μm range, P-562.3CD, Physical Instruments) on top of a motorized stage with a range of approximately 1 cm × 1 cm (HybridStage, JPK Instruments, Berlin, Germany). Fluorescent signals were detected using an Andor iXonEM+ 897 (back-illuminated) electron multiplying charge coupled device (EMCCD) camera (16 μm pixel size, Andor Technology, Belfast, Northern Ireland). This results in an image pixel-size of 166.7 nm/pixel and a total magnification of 96x. Fluorescently labeled samples were excited using a 640 nm solid-state laser (diode-pumped, iBeam Smart, Toptica Photonics Gräfelfing, Germany); and under certain conditions fluorophores were additionally recovered from dark-state with a 405 nm diode laser pulse (iPulse, Toptica Photonics Gräfelfing, Germany). An additional cylindrical lens (f = 500 mm, Thorlabs, Newton, NJ) was introduced in the pathway between camera and the

microscope's side port for 3D single-molecule localization microscopy. Fluorescence emission was additionally filtered with a 700/50 nm emission bandpass filter (AHF, Tübingen, Germany).

2.7. dSTORM

3D dSTORM experiments were performed in a medium containing 50 mM β-mercapto-ethylamine (MEA), 30% glycerine and PBS, a region of interest (ROI) of 256×256 pixels and 10 000 frames were acquired. Fluorophores were illuminated for 20 ms at each frame and an optional 20 ms UV illumination pulse during the readout time of the CCD camera. Prior to each experiment, a calibration for the emitter's axial position localization (compensating the axial PSF distortion) was performed using TetraSpeck (0.1 μm, Thermo Fisher Scientific) microspheres. Experiments were analyzed using the presented real-time lookup table algorithms or by fitting a constrained (σ_x & σ_y) continuous elliptical Gaussian function as previously reported [17]. Typically, position fits were continuous, whereas the lookup table algorithm utilized quantified steps (e.g. 0.1 pixels depending on the parameters for the lookup table generation).

2.8. Computation system architecture

Computations for simulated datasets were performed on a notebook (CPU: Intel Core i7-8650U with 4 cores at 1.9 GHz, 32 GB RAM, Window 10 Education operating system 64 bit) and cell measurements were performed at a workstation (CPU: Intel Xeon CPU E3-1271 with 4 cores at 3.6 GHz, 16 GB RAM, Window 7 Professional operating system 64 bit) equipped with the hardware to control a 405 nm laser and the EMCCD camera.

3. Results

Here, we present a 3D real-time SMLM algorithm not depending on GPU acceleration nor multithreading. We show that lookup tables of pre-calculated 2D elliptical Gaussian signals which approximate the PSF for various lateral positions and shapes (width and height of 2D elliptical Gaussian functions) can be used to accelerate the fitting of fluorescent emitters (approximately 10 times faster compared to 3D STORM Tools [17]).

3.1. Analysis of simulated data

In order to evaluate the performance of our lookup-based algorithm, simulations were generated and analyzed to determine axial and lateral precisions. As a reliable source for SMLM simulations, the 3D microtubule-like datasets [16] from the single-molecule localization microscopy symposium (SMLMS) challenge 2016 organized by École Polytechnique Fédérale de Lausanne (EPFL) were chosen. One modality of the challenge was 3D astigmatism (http://bigwww.epfl.ch/smlm/challenge2016/datasets), which we used for evaluation (see Fig. 1(a)). The analysis of the training dataset *MT0.Nx.LD* by our lookup table algorithm required 12 seconds to complete on a single CPU core. The lookup table was populated with templates of 2D elliptical Gaussian functions that approximate the PSF. A window size of 11 pixels was chosen and the lateral positions were varied over a range of $r_{xy} = 4$ pixels around the center in both directions at $\Delta xy = 0.1$ pixel steps (equals 10 nm steps for an image pixel size of 100 nm). In addition to the lateral position variation, different shapes of the PSF corresponding to axial positions over a range of $r_z = 1000$ nm in $\Delta z = 25$ nm steps were generated. In total 106 641 unique template images were generated. We compared the temporal performance to the continuous least-squares fitting algorithm of our 3D STORM Tools software [17], which needed 20 seconds to fit 20 000 frames on four (+4 virtual) CPU cores. Next, we evaluated the spatial performance of the lookup table algorithm by comparing the ground truth and analyzed dataset. We used the software provided by the SMLM challenge (*CompareLocalization*) to extract the evaluation values as previously described [16]. Furthermore, we compared the lateral and axial

root mean squared localization error (RMSE) over the axial range (see Fig. 1(b)). We scored a Jaccard index [25] of 65% for the high Signal-to-Noise-Ratio (SNR) and 50% for the low SNR, lateral RMSE of 45 nm for the high SNR and 56 nm for the low SNR, axial RMSE of 76 nm for the high SNR and 92 nm for the low SNR, an intersection of 14 899 molecules for the high SNR and 11 451 for the low SNR with an overall efficiency of 61% (40% for the high SNR and 21% for low the SNR).

Additionally, we calculated the Cramér-Rao lower bound (CRLB) for each fitted single emitter signal (see Fig. 1(d)). The CRLB is the "fundamental theoretical limit of localization precisions obtained by unbiased estimator" as previously stated [26]. This lower limit for localization precision can be reached by using maximum-likelihood estimator (MLE) due to the Poisson noise distribution of photon emission. However, we used a least-square estimation for emitter fitting and only calculate the CRLB as measure for lowest possible positional accuracy. In Fig. S1 we present the fitting accuracy over multiple frames and CRLB values for imaged fluorescent beads in different axial positions.

Next, we tested the influence of lower lateral and axial step sizes for the lookup table. Here, we chose a lateral step size of $\Delta xy = 0.05$ pixel (corresponding to 5 nm steps) and an axial step size of $\Delta z = 10$ nm and a window size of 9 pixel. The lateral RMSE decreased by 1.26% (-0.64 nm absolute), the axial RSME by 2.89% (-2.53 nm absolute) and the overall efficiency increased by 2% to 61%. These small incremental changes were not sufficient to justify the greatly increased RAM usage which went from 264 MB to 2.49 GB for the lookup table.

Furthermore, we tested a PSF model, which takes into account pixelation of the EMCCD camera. This model is based on integration of a 2D elliptical Gaussian function [20,27]. The only changes to the model were introduction of our cubic B-spline values for $\sigma_x(z)$ and $\sigma_y(z)$ instead of the polynomials. Furthermore, we multiplied the values of the model with $2\pi\sigma_x(z)\sigma_y(z)$ to convert the integrated intensities to maximum peak intensities (equations S3, S4). We analyzed the SMLMS challenge 2016 dataset (low and high SNR) and compared it to our default 2D elliptical Gaussian model (window size 9 pixels, $\Delta xy = 0.1$ pixels, $r_{xy} = 4$ pixels, $\Delta z = 25$ nm, $r_z = 1000$ nm). The lateral RMSE decreased by -1.26% (-0.14 nm absolute) whereas the axial RSME increased by +1.02% (+0.89 nm absolute) and the overall efficiency increased only by 1% to 60%. Furthermore, our default 2D elliptical Gaussian model needed 14.3 ms ± 1.1 ms (N = 1000 repeats) to generate the lookup table model, the integrated Gaussian model needed 44.2 ms ± 3.0 ms (N = 1000 repeats).

Some defocused emitters near the axial boundaries (see Fig. 1(b)) of the challenge dataset could not be detected. We further investigated these boundary cases with an additional simulated dataset. We simulated a 3D Siemens star-shaped test pattern [10] with discrete axial steps of 45 nm starting from -450 nm to 450 nm (see Fig. 1(c)). The axial position of each emitter was normally distributed around each step with a standard deviation of 25 nm. The pattern was made up of 40 spokes consisting of 20 circle sectors of increasing axial position and 20 blank sectors in between. Simulated emitters were rendered using a 2D elliptical Gaussian function to approximate real PSFs and an ellipticity depending on the axial position (gained from the calibration experiment). Furthermore, noise was added to each simulated frame including readout noise, electron-multiplying noise, and clock-induced charges (baseline: 100 counts, mean peak intensity: 2000 counts, background: 0 counts, EM gain: 300, quantum efficiency: 0.9, readout noise: 74.4, spurious charge: 2×10^{-4}). We simulated 225 000 emitters distributed distrusted over 5000 frames with a minimum distance of 7.5 pixels from each other and an image pixel size of 100 nm. Using our lookup table algorithm, we localized 192 287 (85.5%) of the simulated emitters within nine seconds using our lookup table algorithm, whereas the continuous least-squares fitting algorithm (3D STORM Tools) took 204 seconds to detect 206 976 emitters (92.0%). Localizations around the focus (z-position = 0 nm) had sharper-edged spokes compared to spokes further away from the focus. The reason for this is that photons originating from
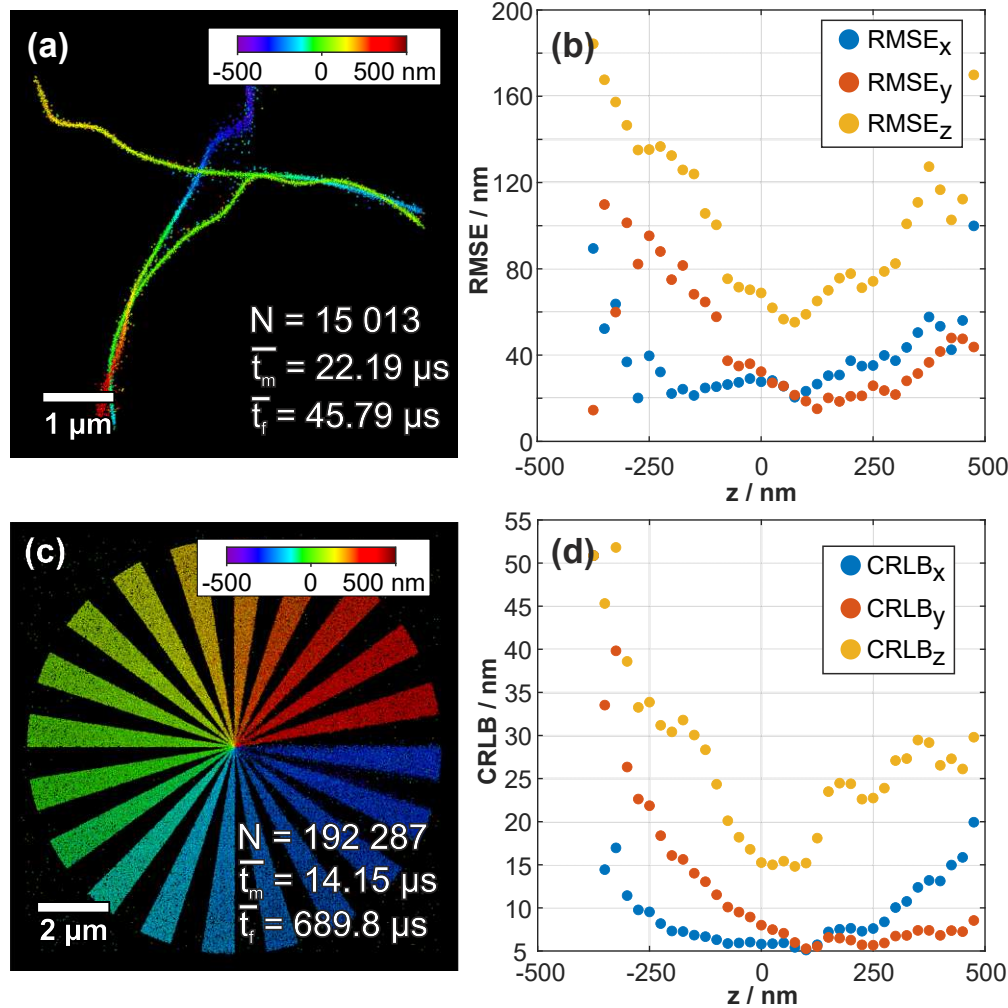
Fig. 1. Lookup table algorithm application on simulated SMLM datasets. The lookup table was populated with templates of 2D elliptical Gaussian functions which approximate the PSF with a window size of 11 pixels and 9 pixels for (**a**) and (**c**) respectively with different lateral positions at 0.1 pixel steps (equals 10 nm steps) and different shapes depending on the axial position over a range of 1000 nm in 25 nm steps. In total, 106 641 different templates were generated. (a) Three-dimensional simulation of microtubules from the single-molecule localization microscopy symposium challenge. The training dataset *MT0.N1.LD* was used to test the lookup table algorithm and determine the 3D position of emitters, where on average a single emitter intensity fit need $t_m = 22.19$ μs, a frame including fitting needed on average $t_f = 45.79$ μs and a total of $N = 15\,013$ emitters was fitted. A comparison of fitted positions with the ground truth dataset, using the comparison tool provided by the challenge, resulted in a Jaccard index of 65%, lateral and axial RMSE of 45 nm and 76 nm respectively, an intersection of 14 899 molecules and an efficiency of 40%. (b) shows the comparison of lateral and axial RMSE to the axial position retrieved from the comparison tool provided by the SMLMS challenge 2016. Our fitted positions are compared to the ground truth of the challenge simulated dataset in (**a**). (c) Simulation of a 3D test pattern made up of 20 circle sectors of increasing axial position and 20 blank circle sectors in between. The axial spoke steps reach from -450 nm to 450 nm in 45 nm steps size. Emitter axial positions are normally distributed for each axial steps with a sigma = 25 nm. The analysis using our lookup table algorithm resulted in an average time to fit a single emitter signal of $t_m = 14.15$ μs, a frame including fitting needed on average $t_f = 680.8$ μs and a total of N = 192 287 emitters was fitted. (**d**) Mean values of the Cramér–Rao lower bound (CRLB) values determined from the discrete z-position (25 nm steps) of the fitted SMLMS 2016 challenge dataset positions.

fluorophores are distributed over a larger pixel area, which results in a lower SNR. Therefore, defocused signals were more challenging to fit because subpixel-determination accuracy is linked directly to the SNR of a signal [28]. However, our lookup table algorithm could handle most of these low SNR signals.

3.2. Real-time SMLM

Here, we show the performance of our lookup table algorithm on fixed biological samples. We imaged the actin cytoskeleton of human platelets and human endothelial cells. Real-time localization allowed us to control the 405 nm UV activation laser pulse intensity to regulate the number of active emitters per frame.

Platelets, upon activation, reorganize their actin cytoskeleton and thereby change their overall shape. SMLM allows for imagining of the actin cytoskeleton with a resolution of 15–30 nm laterally [29,30 6], which additionally can be extended to the third dimension by using a cylindrical lens introducing astigmatism. We observed the distribution of actin labeled with Alexa Fluor 647, on partial activated and fixed human platelets seeded on a glass surface using 3D dSTORM (see Fig. 2(a)). Thereby, we recorded 10 000 frames with an ROI of 256×256 pixels at 25 frames per second and an illumination time of 20 ms. The lookup table for the real-time analysis was populated with templates of 9×9 pixels containing 2D elliptical Gaussian functions approximating the PSF. Lateral positions of the elliptical Gaussian functions were varied over a range of four pixels in both directions around the center (in 0.059 pixel steps which equals 10 nm steps) and in the axial direction we generated different shapes corresponding to axial positions over a range of 1000 nm in 25 nm z-steps. In total 106 641 different templates were generated consuming 264 MB of RAM (including the derivations). Our lookup table algorithm detected 399 252 emitters during the acquisition of the experiment and performed the analysis on average in 1.3 ± 0.2 ms per frame. Since one frame is acquired in 40 ms, we had sufficient time to additionally render the SMLM image and apply an automatic feedback control for the activation laser pulse in order to increase the number of active fluorophores. Figure 2(b) illustrates the timeline of the dSTORM experiment, showing the number of localized emitters (blue curve) and the activation laser power (violet curve). If the number of localized emitters falls below a threshold (here we used 25 localizations) over five consecutive frames, we increased the laser power by 5 mW. Only for the first occurrence of this trigger (indicated with a green triangle with back border in Fig. 2(b)), we turned on the UV laser.

We compared the result of our lookup table algorithm with a continuous least-squares fitting algorithm (3D STORM tools). The continuous algorithm needed 269 seconds to analyze 10 000 frames and detected 574 899 localizations by utilizing four (+4 virtual) CPU cores, whereas our lookup table algorithm required only 45 seconds (loading times of the sequences are not included and are dependent on the file format and hard drive speed). Furthermore, we compared the achieved image resolution by calculation of the FRC on the reconstructed localization microscopy image. The FRC (or spectral SNR) is a measurement for image-resolution of diffraction-unlimited images that take both localization precision and the density of rendered localizations into account [30]. In order to calculate the FRC, we rendered two images using 2D symmetrical Gaussian functions with a sigma of 25 nm and a pixel size of 16.67 nm. For each algorithm, we split the localization microscopy dataset into even and odd frames and analyzed the FRC from these two images using the ImageJ plugin FIRE (Fourier Image REsolution) from [30]. The FRC for the lookup table algorithm was 110 nm and 59 nm for the continuous least-squares fitting algorithm (using the thresholding method of "1 over 7" and smoothed FRC curves).

In a second experiment, we analyzed the actin cytoskeleton of fixed human endothelial cells via labeling with Alexa Fluor 647. The actin cytoskeleton in ECs is much denser and scattered with small F-actin fibers and therefore challenging to observe with 3D dSTORM [31]. We recorded a 3D dSTORM experiment of endothelial cells' actin consisting of 10 000 frames with an ROI of
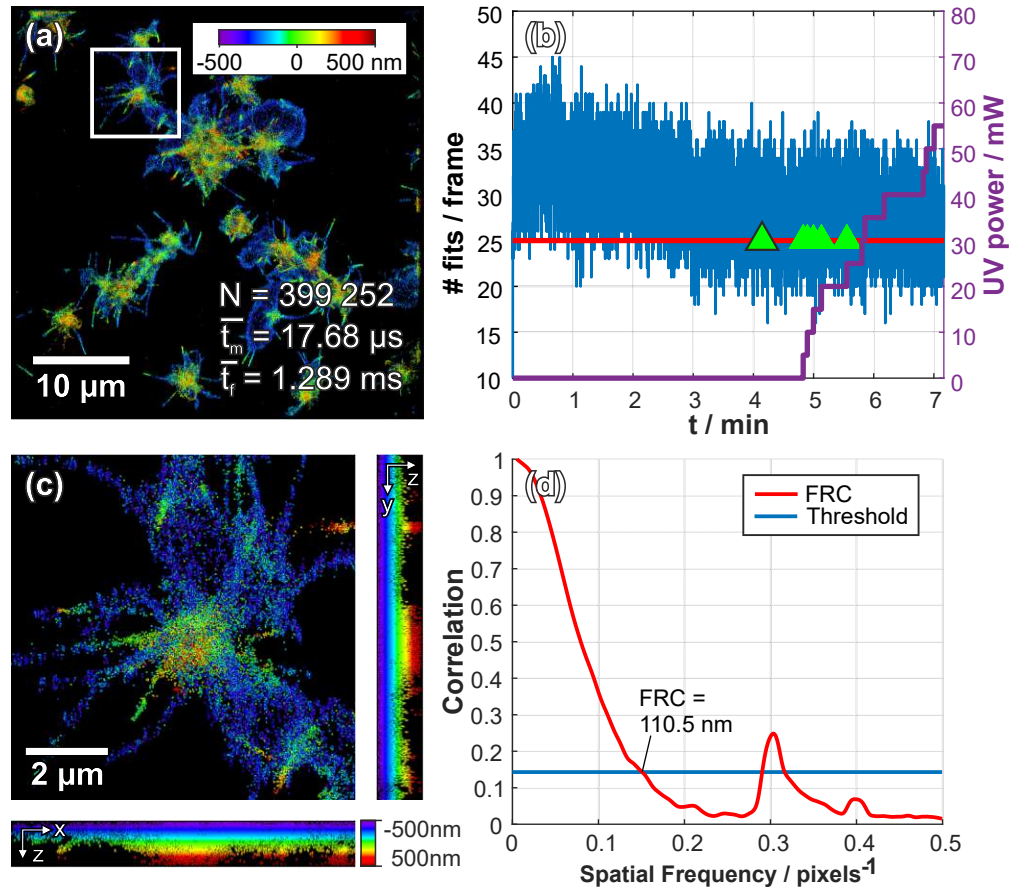
Fig. 2. 3D single molecule localization microscopy data of actin cytoskeleton distribution in human platelets analyzed using our real time lookup table algorithm. The lookup table was populated with templates of 2D elliptical Gaussian functions to approximate the PSF (window size of 9×9 pixels). Various lateral positions within the generated template are placed at 0.059 pixel steps (equivalent to 10 nm) in both directions within a range of 4×4 pixels around the center. Different shapes of the 2D Gaussian function are generated over a range of 1 000 nm in axial steps of 25 nm. For each combination of the 3D positions, unique template images are calculated. In total 289 296 templates were generated. (a) shows an image of the actin cytoskeleton of fixed human platelets labelled with Phalloidin conjugated Alexa 647 visualized using 3D dSTORM. The emitters of the individual fluorophores were fitted in real-time using the lookup table, where the average time to fit a single emitter signal was $t_m = 17.68$ µs, a frame including fitting needed on average $t_f = 1.289$ ms and a total of N = 399 255 emitters was fitted. The experiment consists of 10 000 frames with an ROI of 256×256 pixels. (b) The density of active fluorophores is controlled using a 405 nm activation laser pulse. As soon as the number of detected and fitted emitters falls below 25 pre frame, the UV laser power is increased. At the first occurrence, the laser is turned on (indicated by the green triangle with the black border), next, the laser power is increased by 5 mW. (c) shows a magnified area from (**a**) with side projections in XZ and YZ. (**d**) shows a graph of the smoothed Fourier Ring Correlation (FRC) values calculated from two rendered images including localizations of even and odd frames respectively. A FRC of 110.5 nm was calculated by selecting a threshold of "1 over 7" (14.29% correlation). A second crossing of the FRC-threshold can be observed for 57 nm (at 0.292 pixels^{-1}).

256 × 256 pixels, acquiring 25 frames per second with an illumination time of 20 ms. Using our real-time lookup table algorithm to analyze the SMLM experiment data, we detected 1 232 530 signals (see Fig. 2(c)) with an average localization time of 2.6 ± 1.1 ms per frame. Since the overall density of emitters was very high (mean localization events per frame was 120), the UV laser pulse was only turned on during minute 4 of the acquisition (indicated with a green triangle with back border in Fig. 2(d)) and there was no need to further increase the laser power.

During post-processing, we compared our lookup table algorithm with a continuous least-squares fitting algorithm (3D STORM Tools [17]) for spatial and temporal performance. Our lookup table algorithm required only 58 seconds to analyze 10 000 frames on a single CPU core, whereas the continuous least-squares algorithm needed 269 seconds on four (+4 virtual) CPU cores and detected 1 287 725 emitters (loading times of the sequences are not included and are dependent on the file format and hard drive speed). Again, we compared the spatial image resolution using FRC for both algorithms. The FRC for the lookup table algorithm was 40 nm, whereas the continuous least-squares SMLM fitting algorithm FRC was 59 nm (using the thresholding method of "1 over 7" and smoothed FRC curves).

Real-time SMLM image rendering was achieved by an improved histogram rendering approach. Newly fitted emitters were binned in a 2D image histogram (e.g. an image is by default 10 times the size of the input frame) and the corresponding pixel was assigned the value of the axial position (the histogram image is initialized with all zeros). If the pixel value of that position was not zero, the highest axial position was kept. In a second step, the histogram image is rendered every 10 frames, because rendering is computationally expensive (rendering time: 23.3 ± 5.7 ms for 2560 × 2560 pixels). The axial positions were color-coded (e.g. rainbow color table) and a Gaussian gradient was drawn around the every non-zero pixels. If the current pixel to render contained no localization (i.e. is zero), the surrounding eight pixels were checked for localizations. If any surrounding pixel contained a localization – depending on the position of current pixel (corner or next to the surrounding pixel) – the color mapped to the axial positon of the localization of the surrounding nonzero pixel is drawn with a Gaussian gradient (e.g. sigma of 0.5 or 1 pixel).

4. Discussion

We present a 3D real-time SMLM fitting algorithm that accelerates emitter localization (>10 times) compared to our previously published fitting algorithms [17]. The previously published method uses an unconstrained least-square minimization algorithm for 3D single emitter localization (Double Dogleg optimization [32]) to directly fit a 2D elliptical Gaussian model. However, the algorithm proposed in this paper can only fit the emitter 3D position at discrete steps based on the parameter used for lookup table generation.

Our algorithm is independent from GPU acceleration or multithreading and runs on a single CPU thread. This is possible by using lookup tables containing template images that approximate the PSF of single molecule emitters. The discrete axial and lateral positions at which the different templates are generated stabilizes the fitting procedure. This discretization allows us to only calculate five iterations to find the best fit and avoid local minima. Additionally, we show that decreasing the step size of 3D positions for template generation does not have a major impact on fitting accuracy. Our default step sizes of 10 nm laterally and 25 nm axially are below the Nyquist theorem limit. Typical position accuracies of ~30 nm laterally and ~60 nm axially of a 3D SMLM experiment are more than twice the size of our default step sizes. The discrete spacing can only be observed if the render pixel size is less than the lateral step size used for the positions of the generated template images.

In Fig. 3(d) we calculated a spatial image resolution of 40.7 nm using FRC, however the FRC curve shows a prior local minimum at 61 nm (at 0.273 pixels^{-1}) which is slightly above the threshold. Moreover, in Fig. 2(d) the FRC curve shows a local minimum, which drops below

the threshold. Since both curves follow this course, we assume that the found spatial image resolution in Fig. 3(d) is rather 61 nm instead of the 40.7 nm, which is closer to the real FRC value. The additional peaks in Fig. 2(d) and Fig. 3(d) could be a result of pixilation due to our discrete emitter fitting algorithm.

Next, UV-light modulation enables to control the photochemical properties of the fluorophores [6,10], inducing changes in the on/off state duration. A feedback loop, which allows real-time adaptation of the UV-laser power dependent on the number of emitters detected in an imaged frame helps to keep the numbers of emitters constant. Adjustment of emitter numbers is crucial in terms of multi-emitter fitting, optimization of acquisition time or fluorophore blinking properties, etc.

We want to discuss some improvement on how the lookup table algorithm could be extended in the future: 3D emitter PSFs modulated by a cylindrical lens are not the only PSFs localizable by our methods. The flexibility of our lookup table template image generation allows for arbitrary PSFs. For example, PSFs modeled by a phase mask could be used to fill the lookup table. Fitting of phase mask modeled PSFs is computationally demanding (Fourier transformation) even with GPU parallelization [33]. Therefore, our lookup table algorithm could be used to fit emitters in real-time with an improved model if the phase mask is known. Parameters needed for the phase mask model could be calculated from a phase retrieval calibration using Zernike polynomials from a z-stack of fluorescent beads. These parameters can then be used to populate our lookup table with phase mask modeled PSFs at discrete 3D steps.

The temporal performance of our algorithm for real-time emitter localization allows us to use the dwell time until the next image is acquired for additional tasks. Automated control of the number of on-state fluorophores using a UV activation laser pulse and a real-time rendering system, all running in the dwell time of image acquisition, is doable. Furthermore, FRC can be used to determine the SMLM image-resolution and stop image acquisition if the detail density does not continue to increase. FRC allows for the calculation of image-resolution which also takes emitter density into account. FRC requires two rendered SMLM images for image-resolution calculations [31]. This can be implemented by rendering two additional SMLM images, where newly localized emitters are distributed between these two SMLM images and subsequent calculation of the FRC; our algorithm is capable of performing this action in real-time.

Additionally, image quality can be improved by actively controlling the excitation laser power and imaging frame rate based on the real-time localization information of newly analyzed frames. Fluorophore blinking kinetics as well as the initial switch-off phase (in which fluorophores transition to their dark-state) are crucial for (d)STORM experiment's SMLM image quality. Our real-time algorithm could be used to determine the duration of the initial switch-off phase. As previously stated [6], the excitation laser intensity should be as low as possible to prevent fluorophore bleaching. Only if fluorophores blink uniformly and single emitters be distinguished from each other, then the excitation laser power can be increased to enhance fluorophore blinking. The excitation laser power and the imaging frame rate can be adapted to optimize the photon emission of fluorophores so that their reappearance in subsequent images is minimized – emitter reappearance can be examined by real-time localization information over consecutive frames.

A major challenge in SMLM is the differentiation between true emitters and falsely identified ones. One possibility to distinguish between true emitters and background noise is to use an intensity threshold. However, selecting an intensity threshold is subjective and can vary between experiments and fluorophores. Our algorithm allows for threshold adaptation via user input during the experiment. Thus, threshold selection is subjective. An automated threshold algorithm would be an improvement – e.g. Bayesian thresholding [34]. For Bayesian thresholding a histogram of localized emitter intensities from a defined number of images is calculated. To adapt the threshold, the histogram is analyzed using a Generalized Minimum Error Thresholding
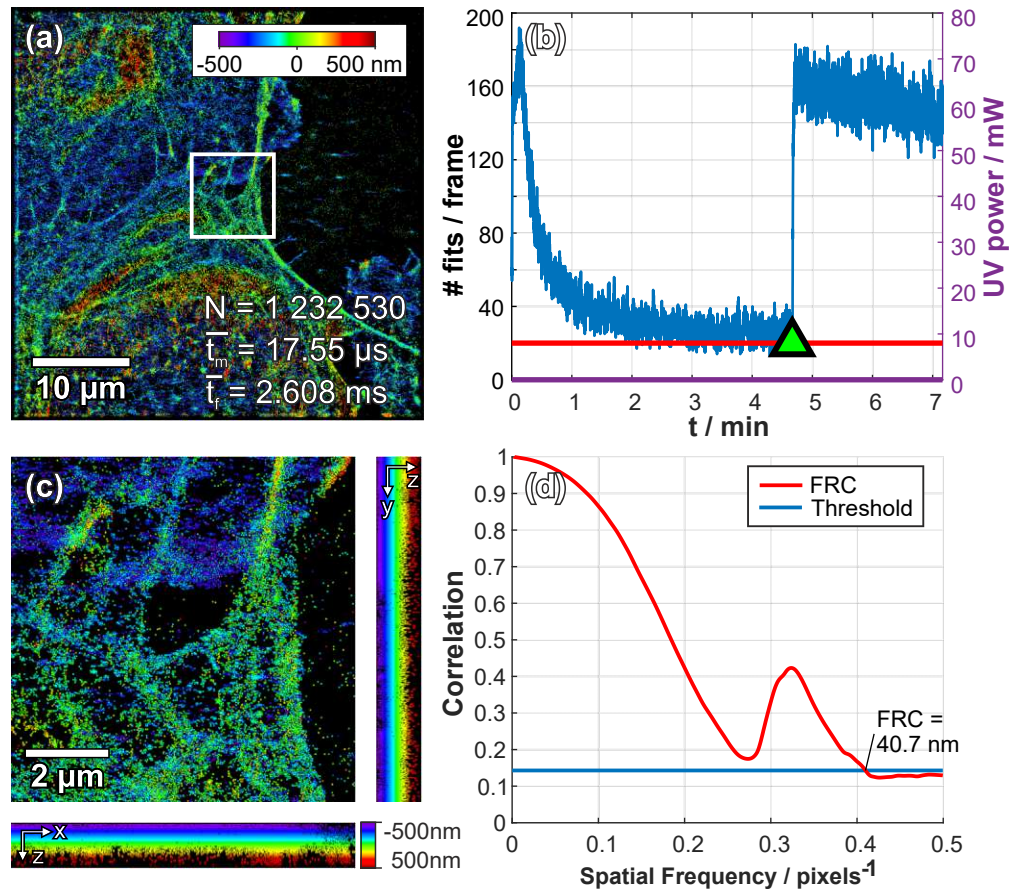
Fig. 3. **3D single molecule localization microscopy data of the actin cytoskeleton labeled in human endothelial cells analyzed using our real time lookup table algorithm**. The lookup table was populated with templates of 2D elliptical Gaussian functions which approximate the PSF, with a window size of 9 pixels. Different lateral positions within the generated template are placed at 0.059 pixel steps (equivalent to 10 nm) in both directions within a range of 4×4 pixels around the center. Different shapes of the 2D Gaussian function are generated over a range of 1 000 nm in axial steps of 25 nm. For each combination of the 3D positions, unique template images are calculated. In total 289 296 templates were generated. (a) shows an image of the actin cytoskeleton of primary human endothelial cells (phEC) on a gelatine coated glass slide labelled with Phalloidin conjugated Alexa 647. The lookup table algorithm was used to determine emitter positions in real-time, where an average time to fit a single emitter signal was $t_m = 1.55\,\mu s$, a frame including fitting needed on average $t_f = 2.609$ ms and a total of N = 1 232 530 emitters was fitted. The experiment consisted of 10 000 frames with an ROI of 256×256 pixels. (b) The number of detected emitters per frame was used to control the UV activation laser pulse. Here, the density of fitted localizations was overall high (compared to the platelet experiment), thus the laser pulse was only turned on (indicated by the green triangle with the black border) to keep the number of active fluorophores above 25 per frame. The increase of the active fluorophores after laser activation is caused by UV laser emission even at 0-power adjustment. (c) shows a magnified box area in (**a**) with side projections in XZ and YZ. (**d**) shows a graph of the smoothed Fourier Ring Correlation (FRC) values calculated from two rendered images consisting of localizations of even and odd frames respectively. A FRC of 40.7 nm was calculated by selecting a threshold of "1 over 7" (14.29% correlation). A prior local minimum is visible at 61 nm (at 0.273 pixels^{-1}) in (**d**), which is slightly above the threshold. This might indicate the real image resolution and would be consistent with the FRC behavior observed in the previous sample (see Fig. 2(d)).

algorithm (GMET). This can all be done in real-time since intensities for localized emitters are continuously available during the acquisition.

Another effect influencing SMLM image quality is sample drift introduced by the excitation laser, temperature changes, mechanical relaxation, objective oil expansion/relaxation, or electrical noise. The mechanical displacement accumulates over the long acquisition time of SMLM experiments and impairs the SMLM's image quality [35]. Currently, two main drift correction/estimation methods are used: The first uses fiducial markers or special hardware to measure the drift directly [36]. The second uses the fitted emitter localizations to directly calculate the drift. The majority of these algorithms use cross-correlation on substacks of SMLM images binned into time intervals of equal length. An alternative to cross-correlation is the direct calculation of the drift from the positions of fitted emitters, avoiding the rendering of multiple SMLM images. As stated [37], drift correction equations can be solved numerically based on distance matrices consisting of fitted emitter positions at different time intervals. However, only a few of these algorithms allow for real-time drift correction. Our algorithm can be used to calculate either the SMLM images used for cross-correlation or directly supply a drift correction algorithm with the currently fitted localizations. Furthermore, these drift estimates can be used to counteract the drift by controlling a 3D piezo positioning stage parallel to the SMLM experiment acquisition.

In conclusion, our algorithm can be used for feedback-controlled real-time SMLM experiments and allows to improve the experiment's image quality based on real-time localization information. Therefore we supply an example implementation for ImageJ [38] that uses a CPP library for the time-critical algorithms and an easy to extend java interface for expansion and custom lookup table templates.

Disclosures. The authors declare no conflicts of interest.

Data availability. Data and source code underlying the results presented in this paper are available at [38].

Supplemental document. See Supplement 1 for supporting content.

References

1. M. Heilemann, S. van de Linde, M. Schüttpelz, R. Kasper, B. Seefeldt, A. Mukherjee, P. Tinnefeld, and M. Sauer, "Subdiffraction-resolution fluorescence imaging with conventional fluorescent probes," Angew. Chem. Int. Ed. **47**(33), 6172–6176 (2008).
2. B. Huang, W. Wang, M. Bates, and X. Zhuang, "Three-dimensional super-resolution imaging by stochastic optical reconstruction microscopy," Science **319**(5864), 810–813 (2008).
3. Y. Shechtman, S. J. Sahl, A. S. Backer, and W. E. Moerner, "Optimal point spread function design for 3D imaging," Phys. Rev. Lett. **113**(13), 133902 (2014).
4. S. R. P. Pavani, M. a Thompson, J. S. Biteen, S. J. Lord, N. Liu, R. J. Twieg, R. Piestun, and W. E. Moerner, "Three-dimensional, single-molecule fluorescence imaging beyond the diffraction limit by using a double-helix point spread function," Proc. Natl. Acad. Sci. **106**(9), 2995–2999 (2009).
5. L. Li, B. Xin, W. Kuang, Z. Zhou, and Z.-L. Huang, "Divide and conquer: real-time maximum likelihood fitting of multiple emitters for super-resolution localization microscopy," Opt. Express **27**(15), 21029 (2019).
6. R. Diekmann, M. Kahnwald, A. Schoenit, J. Deschamps, U. Matti, and J. Ries, "Optimizing imaging speed and excitation intensity for single-molecule localization microscopy," Nat. Methods **17**(9), 909–912 (2020).
7. L. Nahidiazar, A. V. Agronskaia, J. Broertjes, B. Den Van Broek, and K. Jalink, "Optimizing imaging conditions for demanding multi-color super resolution localization microscopy," PLoS One **11**(7), e0158884 (2016).
8. N. Olivier, D. Keller, P. Gönczy, and S. Manley, "Resolution doubling in 3D-STORM imaging through improved buffers," PLoS One **8**(7), e69004 (2013).
9. S. Wolter, M. Schüttpelz, M. Tscherepanow, S. Van De Linde, M. Heilemann, and M. Sauer, "Real-time computation of subdiffraction-resolution fluorescence images," J. Microsc. **237**(1), 12–22 (2010).
10. A. Kechkar, D. Nair, M. Heilemann, D. Choquet, and J. Sibarita, "Real-time analysis and visualization for single-molecule based super-resolution microscopy," PLoS One **8**(4), e62918 (2013).
11. N. Brede and M. Lakadamyali, "GraspJ: an open source, real-time analysis package for super-resolution imaging," Opt. Nanoscopy **1**(1), 11 (2012).

12. Y. Tang, L. Dai, X. Zhang, J. Li, J. Hendriks, X. Fan, N. Gruteser, A. Meisenberg, A. Baumann, A. Katranidis, and T. Gensch, "SNSMIL, a real-time single molecule identification and localization algorithm for super-resolution fluorescence microscopy," Sci. Rep. **5**(1), 11073 (2015).

13. R. Henriques, M. Lelek, E. F. Fornasiero, F. Valtorta, C. Zimmer, and M. M. Mhlanga, "QuickPALM: 3D real-time photoactivation nanoscopy image processing in ImageJ," Nat. Methods **7**(5), 339–340 (2010).

14. C. S. Smith, N. Joseph, B. Rieger, and K. A. Lidke, "Fast, single-molecule localization that achieves theoretically minimum uncertainty," Nat. Methods **7**(5), 373–375 (2010).

15. Y. Li, M. Mund, P. Hoess, J. Deschamps, U. Matti, B. Nijmeijer, V. J. Sabinina, J. Ellenberg, I. Schoen, and J. Ries, "Real-time 3D single-molecule localization using experimental point spread functions," Nat. Methods **15**(5), 367–369 (2018).

16. D. Sage, T.-A. Pham, H. Babcock, T. Lukes, T. Pengo, J. Chao, R. Velmurugan, A. Herbert, A. Agrawal, S. Colabrese, A. Wheeler, A. Archetti, B. Rieger, R. Ober, G. M. Hagen, J.-B. Sibarita, J. Ries, R. Henriques, M. Unser, and S. Holden, "Super-resolution fight club: assessment of 2D and 3D single-molecule localization microscopy software," Nat. Methods **16**(5), 387–395 (2019).

17. S. Mayr, F. Hauser, S. Puthukodan, M. Axmann, J. Göhring, and J. Jacak, "Statistical analysis of 3D localisation microscopy images for quantification of membrane protein distributions in a platelet clot model," PLOS Comput. Biol. **16**(6), e1007902 (2020).

18. S. Proppert, S. Wolter, T. Holm, T. Klein, S. van de Linde, and M. Sauer, "Cubic B-spline calibration for 3D super-resolution measurements using astigmatic imaging," Opt. Express **22**(9), 10304–16 (2014).

19. A. Neubeck and L. Van Gool, "Efficient non-maximum suppression," in *18th International Conference on Pattern Recognition (ICPR'06)* (IEEE, 2006), 3, pp. 850–855.

20. S. Liu, E. B. Kromann, W. D. Krueger, J. Bewersdorf, and K. A. Lidke, "Three dimensional single molecule localization using a phase retrieved pupil function," Opt. Express **21**(24), 29462 (2013).

21. R. C. Whaley and J. J. Dongarra, "Automatically tuned linear algebra software," in *Proceedings of the IEEE/ACM SC98 Conference* (IEEE, 1998), pp. 38.

22. M. Agarwal and R. Mehra, "Review of matrix decomposition techniques for signal processing applications," J. Eng. Res. Appl. **4**(1), 90–93 (2014).

23. M. H. Symons and T. J. Mitchison, "Control of actin polymerization in live and permeabilized fibroblasts," J. Cell Biol. **114**(3), 503–513 (1991).

24. D. C. S. Pedroso, A. Tellechea, L. Moura, I. Fidalgo-Carvalho, J. Duarte, E. Carvalho, and L. Ferreira, "Improved survival, vascular differentiation and wound healing potential of stem cells co-cultured with endothelial cells," PLoS One **6**(1), e16114 (2011).

25. N. C. Chung, B. Miasojedow, M. Startek, and A. Gambin, "Jaccard/Tanimoto similarity test and estimation methods for biological presence-absence data," BMC Bioinformatics **20**(S15), 644 (2019).

26. Y. Sun, "Localization precision of stochastic optical localization nanoscopy using single frames," J. Biomed. Opt. **18**(11), 111418 (2013).

27. F. Huang, S. L. Schwartz, J. M. Byars, and K. A. Lidke, "Simultaneous multiple-emitter fitting for single molecule super-resolution imaging," Biomed. Opt. Express **2**(5), 1377 (2011).

28. B. Rieger and S. Stallinga, "The lateral and axial localization uncertainty in super-resolution light microscopy," ChemPhysChem **15**(4), 664–670 (2014).

29. S. Mayr, F. Hauser, A. Peterbauer, A. Tauscher, C. Naderer, M. Axmann, B. Plochberger, and J. Jacak, "Localization microscopy of actin cytoskeleton in human platelets," Int. J. Mol. Sci. **19**(4), 1150 (2018).

30. R. P. J. Nieuwenhuizen, K. A. Lidke, M. Bates, D. L. Puig, D. Grünwald, S. Stallinga, and B. Rieger, "Measuring image resolution in optical nanoscopy," Nat. Methods **10**(6), 557–562 (2013).

31. K. Xu, H. P. Babcock, and X. Zhuang, "Dual-objective STORM reveals three-dimensional filament organization in the actin cytoskeleton," Nat. Methods **9**(2), 185–188 (2012).

32. J. E. Dennis and H. H. W. Mei, "Two new unconstrained optimization algorithms which use function and gradient values," J. Optim. Theory Appl. **28**(4), 453–482 (1979).

33. A. Aristov, B. Lelandais, E. Rensen, and C. Zimmer, "ZOLA-3D allows flexible 3D localization microscopy over an adjustable axial range," Nat. Commun. **9**(1), 2409 (2018).

34. Y. Tang, J. Hendriks, T. Gensch, L. Dai, and J. Li, "Automatic Bayesian single molecule identification for localization microscopy," Sci. Rep. **6**(1), 33521 (2016).

35. M. J. Mlodzianoski, J. M. Schreiner, S. P. Callahan, K. Smolková, A. Dlasková, J. Šantorová, P. Ježek, J. Bewersdorf, and P. Je, "Sample drift correction in 3D fluorescence photoactivation localization microscopy," Opt. Express **19**(16), 15009–15019 (2011).

36. S. Coelho, J. Baek, M. S. Graus, J. M. Halstead, P. R. Nicovich, K. Feher, H. Gandhi, J. J. Gooding, and K. Gaus, "Ultraprecise single-molecule localization microscopy enables in situ distance measurements in intact cells," Sci. Adv. **6**(16), eaay8271 (2020).

37. R. Han, L. Wang, F. Xu, Y. Zhang, M. Zhang, Z. Liu, F. Ren, and F. Zhang, "Drift correction for single-molecule imaging by molecular constraint field, a distance minimum metric," BMC Biophys **8**(1), 1 (2015).

38. F. Hauser and J. Jacak, "Data and source code," Github (2021), https://github.com/CURTLab/IJLookUpSTORM.

(Under revision) Platelet activation studies via 3D localization microscopy and machine learning on a blood vessel chip

Fabian Hauser[1,2], Christoph Naderer[1], Sandra Milic1[1], Eleni Priglinger[2,4], Boris Buchroithner[1], Anja Peterbauer[3], Michael B. Fischer[5], Heinz Redl[4,2], Jaroslaw Jacak[1,2*]

1 University of Applied Sciences, Upper Austria School of Medical Engineering and Applied Social Sciences, Garnisonstraße 21, 4020 Linz, Austria
2 Austrian Cluster for Tissue Regeneration, Vienna 1200, Austria
3 Red Cross Blood Transfusion Service for Upper Austria, Krankenhausstr. 7, 4017 Linz, Austria
4 Ludwig Boltzmann Institute for Traumatology in Cooperation with the AUVA, 1200 Vienna, Austria
5 Department for Biomedical Research, Center of Experimental Medicine, Danube University Krems, Krems an der Donau, Austria

* corresponding jaroslaw.jacak@fh-linz.at

Abstract

We present a platform consisting of microfluidics, two-colour 3D nanoscopy, and advanced image processing methods for studying platelet activation on a single-cell level. An inner blood vessel wall was mimicked by primary human CD34$^+$ endothelial cells (ECs) grown in our custom microfluidic chip. Firstly, we investigate the platelets activation (indicated by CD62P expression) on ECs with various stress levels. To additionally stress individual ECs we treated their nucleus with a femtosecond pulsed laser outside the incubation chamber. For the ECs' stress level quantification, mitochondrial structures were examined via 3D single-molecule localization microscopy and classified using machine learning. Laser-treated and stress-prone ECs showed pathological mitochondrial morphology with fragmented networks in contrast to stress-resistant ECs. Activated platelets were predominantly found in proximity to stressed-prone ECs under static and dynamic conditions. Secondly, based on the CD62P distribution of activated platelets we quantitatively analysed their volumes. We show that platelets activated under flow conditions exhibit 8-9 times larger volumes compared to platelets activated under static conditions. Our platform allows quantitative analysis of platelet activation on ECs dependent on mitochondria-based stress level determination.

Author summary

There is a lack of systems for quantification of early-stage thrombus formation under flow conditions at a nanoscale level. Single-molecule localization microscopy (SMLM) allows imaging small subcellular structures and biomolecules with nanometre precision, which is highly relevant for medicine and biology. In this context, we present a platform combining microfluidics, software tools, and two-colour 3-dimensional SMLM to study mitochondria of endothelial cells and platelet activation under flow conditions. Our studies were performed in a microfluidic device modelling small blood vessels.

Mitochondria, which supply cells with energy, change morphology depending on the cellular stress level. Herein, we applied machine learning-assisted algorithms to quantify mitochondria morphology, allowing us to determine individual endothelial cells' stress levels. Platelets are blood cells and contribute significantly to hemostasis to seal injured blood vessels during activation. Thus, we compared the distribution of activated platelets with endothelial cells in the surrounding area. Using our microfluidic platform, we were able to show a link between stressed endothelial cells and activated platelets. We believe that our platform could be helpful to further investigate interactions of endothelial cells with other blood cells or drugs and link treatments with cellular stress.

Introduction

In vitro modelling of blood vessels under flow conditions has been performed for quantifying platelet adhesion, microvascular occlusion, haemostasis, and thrombus formation [1–6]. Platelet adhesion to healthy endothelium is inhibited by an intact glycocalyx [7] and mediators released by endothelial cells [8]. However, injured endothelium exposing pro-thrombotic surfaces initiates platelet adhesion, where the glycoprotein (GP)Ib-IX-V receptor binds to van Willebrand Factor (vWF) protein. In addition, GPIb-IX binding by platelets can also occur following thrombin binding or be induced by integrin binding (e.g., $\alpha m\beta 2$). Platelet aggregation, in contrast, is mediated by the interaction of the CD41/CD61 complex (GPIIb/IIIa) with fibrinogen [9] or the binding of extracellular matrix components such as collagen, laminin and fibronectin to GPVI. Signals via these GPs depend on shear stress which affects platelet morphology. At low shear stress values (<40 dyne/cm^2), platelets are spherical shaped and form filopodia; at higher values, platelets are more discoid shaped and can form additional tethers [10].

Binding of exposed collagen with GPVI receptor and integrin $\alpha 2\beta 1$ enables platelet activation on injured endothelium. Platelet activation triggers thrombus formation, repair, and closure of the affected blood vessel [11]. In addition to facilitating haemostasis, platelets respond to local dangers [12] and can modulate inflammatory reactions by supporting the recruitment of leukocytes to inflamed or damaged blood vessels. Platelet activation can be triggered by high shear stress [13], by chemical or physical agonists [14] and by infections [12]. Also, cellular stressors disturb haemostasis and can trigger platelet activation [15]: increased production of reactive oxygen species (ROS), increased level of ROS originating extracellular (e.g., ultraviolet light), DNA damage, laser injury [16], mechanical damage, toxins [17], or changes in temperature [18]. The cell's adaptive capacity helps to survive introduced stress and escape the programmed cell death [17]. One possibility to assess cellular stress is to investigate changes in mitochondrial network formation. Mitochondria constantly undergo fusion into highly branched networks and fission into smaller punctate and rod-like structures [19]. Long mitochondria networks indicate healthy and stress-resistant cells; a high number of short networks or punctate indicate the presence of cellular stressors [17]. Quantitative imaging of the mitochondrial morphology enables 2D and 3D classification of cellular health and disease [20–24]. Platelet activation depending on EC physiology within a microfluidic system has not yet been addressed in detail on the molecular level.

In this work, we implemented a customized microfluidic system with primary human CD34$^+$ ECs [25]. ECs were cultured in the microfluidic chip until confluency was achieved. The confluent layer was perfused until more than 65% of the ECs were flow-oriented. A femtosecond pulsed laser was used to treat selected single ECs within the layer. Changes in the environmental conditions during the laser treatment induced stress in all cultured ECs. Stress-prone (spECs) and laser-treated ECs (ltECs) showed mitochondrial network fragmentation, while stress-resistant ECs (srECs) maintained

their typically long and branched mitochondrial networks. 3D single-molecule ₄₂
localization microscopy (SMLM) was used to assess the mitochondrial network integrity ₄₃
using a custom software tool for the segmentation of puncta, rod and network ₄₄
structures. This allowed for the classification of ECs based on their mitochondria ₄₅
morphology: srECs, spECs, and ltECs. Two-colour 3D SMLM enabled the simultaneous ₄₆
observation of the EC's mitochondria and platelet activation. Activated platelets ₄₇
stained with anti-CD62P (P-selectin) antibodies were used to observe platelet adhesion ₄₈
to ECs with different stress levels. SMLM data of CD62P signals enabled the ₄₉
comparison of platelet volumes and densities under static or flow conditions. With these ₅₀
experiments, we have shown the applicability of our developed platform to analyse ₅₁
platelet activation on a blood vessel wall model at a single cell level. ₅₂

Results ₅₃

Blood vessel chip ₅₄

We designed a microfluidic chip to mimic the flow conditions within a blood vessel. ₅₅
Fig 1a shows a schematic drawing of the developed microfluidic system (including chip, ₅₆
tubes, medium reservoir, injection port, and peristaltic pump). The bottom consists of ₅₇
a 0.15 mm thick coverslip enabling high NA (NA > 1.4 objective lens, working distance ₅₈
 0.3 mm) imaging. A channel (1.5 x 36 mm, 335 µm thick, aspect ratio 4.5, cross area ₅₉
0.5 mm^2) was cut into a sandwiched polymer foil with a final channel volume of 17 µL. ₆₀
The Navier-Stokes equation in 3D for rectangular channels according to [26] was used to ₆₁
calculate the shear stress acting on the ECs. A viscosity value of $\eta = 0.875 \ mPa \cdot s$ ₆₂
(99% RPMI + 5% FBS [27] + 1% whole blood [28] to account for the platelets), as well ₆₃
as the given channel length of 34 mm (excluding the inlet size) and a flow rate of ₆₄
119 µL/min, was used. Additionally considered was the hydraulic resistance of the ₆₅
290 cm long tube. The calculated values for pressure, flow velocity and wall shear stress ₆₆
were 51 Pa, 3.95 mm/s and 0.62 dyne/cm^2, respectively. In comparison, typical blood ₆₇
vessel wall shear stress values of 1-20 dyne/cm^2 have been reported [28]. ₆₈

The microfluidic chip was seeded with CD34$^+$ ECs (provided by Prof. Fabien ₆₉
Gosselet, Université d'Artois, France) [25], which have previously shown an improved ₇₀
wound healing- and vascular differentiation potential [29–32]. In our experiments, ₇₁
CD34$^+$ ECs had tighter intercellular junctions compared to HUVEC/Tert2 (S1 Fig). ₇₂
The delivery of ECs into the channel was applied using a 3-way stopcock with a septum ₇₃
and a syringe. A peristaltic pump delivered 595 µL of medium from a reservoir into the ₇₄
channel every 4 hours at a flow rate of 119 µL/min. Every 24 hours, ECs' morphology ₇₅
and confluency were observed with phase-contrast imaging. An automated cell counting ₇₆
software was applied to quantify EC proliferation (red dots indicate detected nuclei of ₇₇
Fig 1b). Values above 500 cells/mm^2 were considered confluent. Once confluency was ₇₈
reached, the delay time of the peristaltic pump was gradually decreased (3 h, 2 h, 1 h, ₇₉
0.5 h and 0.25 h). Simultaneously, the active pump time was increased (5 min, 10 min, ₈₀
20 min, 30 min) until continuous pumping was reached. ECs were cultured under ₈₁
constant flow conditions at 0.62 dyne/cm^2 until at least 65% of them aligned with the ₈₂
flow direction. Fig. 1b shows the microfluidic chip seeded with ECs after 2 days of ₈₃
continuous flow, where ECs already align with the flow direction. Live cell platelet ₈₄
interaction experiments under flow conditions were tested on a confluent EC monolayer ₈₅
seeded in the blood vessel chip. We tracked individual platelets (S2 Fig a, S1 Video) ₈₆
flowing over the EC monolayer and confirmed platelet adhesion and activation using ₈₇
CD41 (S2 Fig b, S2 Video) and CD62P (S2 Fig b), respectively. ₈₈
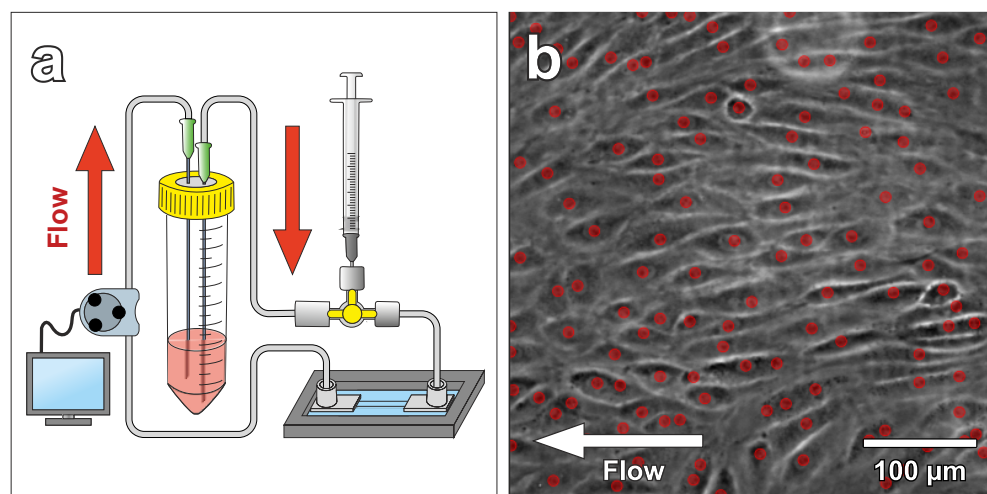
Fig 1. Microfluidic system design, cell seeding and platelet interactions. a) shows a schematic drawing of the microfluidic system. The system was connected to a 3-way stopcock with a septum to allow injecting media containing suspended CD34$^+$ endothelial cells (ECs). A peristaltic pump was used to dispense cell culture medium from the reservoir with a variable flow rate. b) shows a phase-contrast image of CD34$^+$ adherent ECs within the microfluidic chip after 2 days under constant flow (most ECs aligned with the flow direction). The red dots indicate automatically detected nuclei. Number of detected nuclei in the image: 111 on 0.19 mm^2.

Laser-treatment of endothelial cells

Only single platelets adhered sparsely distributed on a tight and flow orientated monolayer of CD34$^+$ ECs. More precisely, platelets preferably adhered to disrupted intercellular junctions (S1 Fig) or to ECs with signs of stress that occurred presumably due to stress manipulating cells outside the incubator. To gain spatio-temporal control of cellular stress, single EC nuclei were treated with a femtosecond pulsed laser. Experiments (N = 11, 3-5 ECs treated each) targeting single ECs were carried out using a 515 nm laser (290 fs pulse duration, 1 MHz repetition rate) with a peak power of 1600 W/µm^3 and an air objective lens (50x, NA = 0.42). During laser treatment, ltECs exhibited morphological changes, nucleoplasm leakage, as well as occasionally nuclear bleb formation (Fig 2b). Bleb formation was comparable to experiments with laser treatment of NIH3T3 cells [33]. Recent works have also proven that laser irradiation can lead to increased levels of ROS, induced membrane or DNA damage and frequently lead to cell death [17, 34, 35]. Cell death of ltECs has been confirmed using LIVE/DEAD™ Red Dead Cell Stain (Fig 2c,d) and ECs showed signs of cell death within <1h after laser treatment.

Cellular stress classification

The 3D distribution of mitochondria has been used to analyse cellular stress levels of individual CD34$^+$ ECs within the perfused layer (dead cells confirmed via LIVE/DEAD assay). Three to five individual ECs in the centre of the microfluidic chip were selected and subsequently treated using fs-laser pulses (<60 min outside the incubator). The microfluidic chip was placed back into the incubator for 15 minutes to allow ECs to recover. Subsequently, ECs were fixed and stained for imaging.To analyse the 3D mitochondria morphology, single-molecule positions of anti-mitochondria antibodies
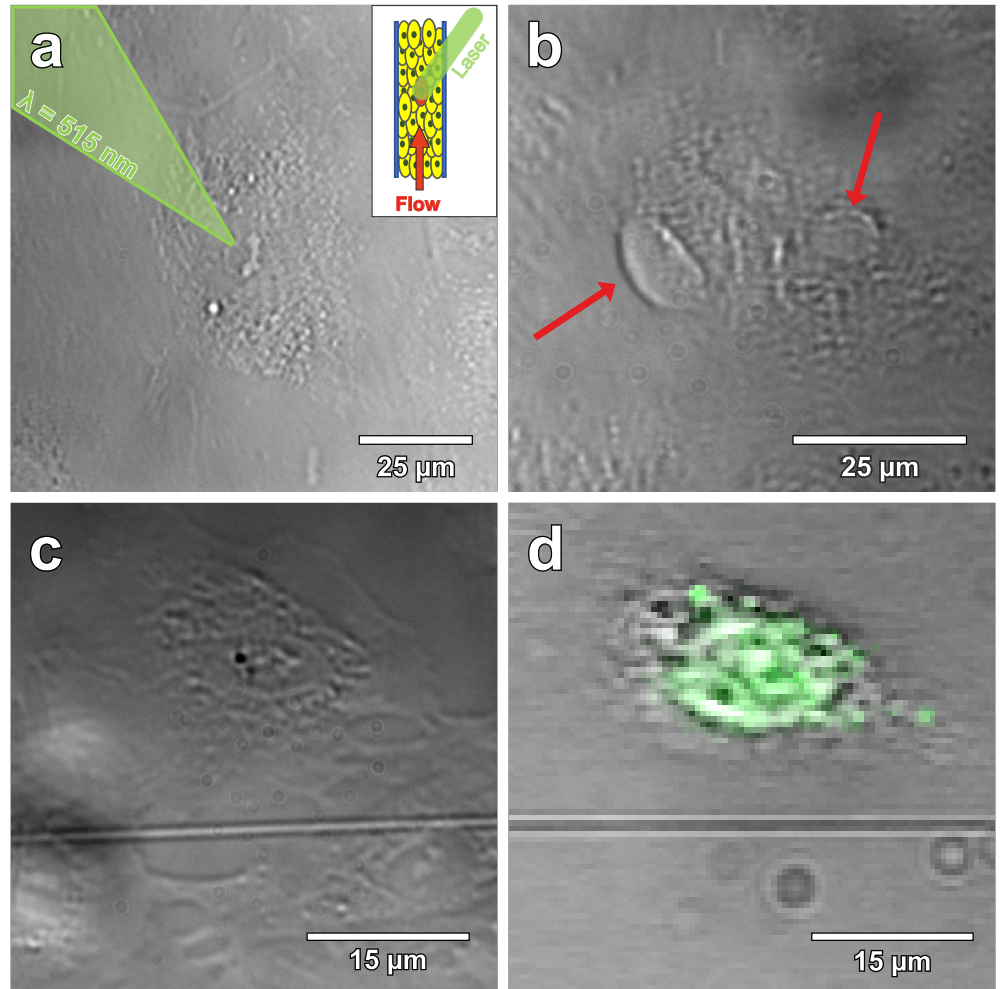
Fig 2. Bright-field microscopy images of laser-treated endothelial cells (ltECs). a) shows an image during the laser treatment process. A femtosecond pulsed laser was used to stress selected cells within the developed microfluidic chip under flow conditions. b) depicts an image of a ltEC forming blebs (red arrows) under flow conditions. c) shows a bright-field microscopy image of a ltEC under static conditions. d) displays an image of the same cell as shown in c) after fixation and overlayed with a LIVE/DEAD® Red Dead Cell Stain in green, which indicates that ltEC dies within <1h after laser treatment.

were converted into a 3D volume and analysed. Volumes with a voxel size of 85 nm x 85 nm x 25 nm were rendered from the single-molecule signals. as a 3D Gaussian function. These mitochondria volumes determined from the 3D localization positions were subsequently smoothed, thresholded, segmented and skeletonized to quantify their spatial orientation [36]. Based on the resulting 3D skeletonized image, parameters like segment voxels, number and length of branches were calculated. These parameters were used to classify mitochondria segments into puncta, rod, and network categories using machine learning (random forest classification [37]). A 3D surface reconstruction (marching cube algorithm [38]) of the classified mitochondria structures is shown in Fig 3e. The colours green, cyan, and blue indicate the categories puncta, rod and network, respectively. The overall results of the classification are presented in
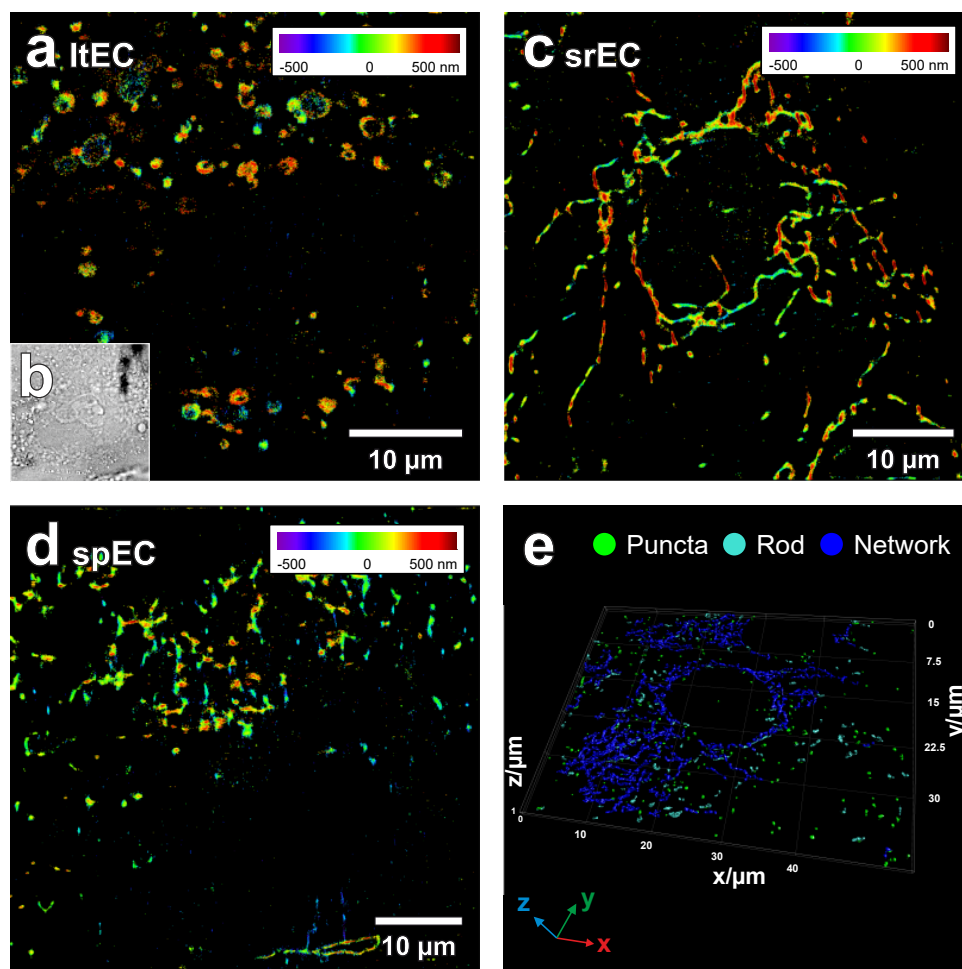
Fig 3. 3D single-molecule localization microscopy (SMLM) images of endothelial cells (ECs) mitochondria within the microfluidic chip under flow conditions. a) shows a SMLM rendering of mitochondria (positional accuracy of 46 nm lateral and 53 nm axial) of a laser-treated EC (ltEC) stained with anti-mitochondria antibody conjugated to Alexa Fluor$^{©}$ 488. Axial positions are represented using rainbow colours from violet (below focus) to dark red (above focus). 3D SMLM data were converted into a volume image and each mitochondria segment produced by skeleton analysis was classified using random forest classification. Mitochondria morphology classification of a) resulted in 33% puncta, 23% rods and 44% networks. b) shows a bright-field microscopy image of the same EC as in a). In c) a reconstructed 3D SMLM image of a stress-resistant EC (srEC) with a continuous mitochondria network (positional accuracy of 51 nm lateral, 80 nm axial, 20% puncta, 20% rods and 60% networks) is displayed. d) depicts a reconstructed 3D SMLM image of a stress-prone EC (spEC) (positional accuracy of 52 nm lateral, 66 nm axial, 29% puncta, 32% rods and 39% networks). e) visualizes a 3D surface reconstruction of a volume rendering from 3D SMLM localizations (positional accuracy of 22 nm lateral and 125 nm axial). The results of mitochondrial classification were colour-coded and indicate the categories: puncta (green), rod (cyan) and network (blue) with 10%, 15% and 75% of voxels in each category, respectively.

Table 1. Based on the distribution of classified voxels in each category, the stress level of single ECs can be determined [20, 39]. Large, interconnected mitochondrial networks were observed in srECs [35], while puncta and rod-like mitochondria arrangements were highly represented in spECs.

Table 1. Statistics of cellular mitochondria morphology classification of endothelial cells (ECs) under different conditions.

State	# ECs	Mean puncta	Median puncta	Mean rods	Median rods	Mean networks	Media networks	shown in
Static	27	24.9±2.8%	24%	31.9±3%	28%	43.1±5.1%	48%	Fig 3a
Dynamic	16	28.1±3.5%	25.5%	32.8±3.6%	28.5%	39.1±5.3%	36%	Fig 3c
Laser treated	4	33.5±6.5%	31.5%	37.5±5%	38%	29.25±10%	37.5%	Fig 3d

Mitochondria segments of whole and partial ECs were extracted and classified. The percentage of voxels found in each category was then compared to the total number of voxels found within each extracted EC. Median, mean, and standard error were calculated for each experimental condition: static cultivation, dynamic cultivation within the microfluidic chip under flow conditions and laser-treated ECs under dynamic conditions.

## Analysis of platelet activation

Experiments were either conducted under static (SC) or dynamic (DC) conditions. In SC experiments, ECs were cultivated and incubated with platelets under static conditions. In DC experiments, ECs were cultivated within the microfluidic system under flow conditions (119 µL/min) and platelets were added into the flow. For SMLM imaging, the activated platelets were stained with anti-CD62P antibodies conjugated to Alexa Fluor© 647 and mitochondria were stained with anti-mitochondria antibodies conjugated to Alexa Fluor© 488. 3D SMLM images were subsequently corrected for spatial drift [40] and fluorescent bleed-through (custom software) and the mitochondria morphology was classified. Table 2 shows the voxel classification of mitochondria morphology for each image in Fig 4. Mitochondria of platelets were discarded due to their smaller size during analysis. On average 1.32±1.3 and 1.63±1.4 activated platelets per EC were determined in SC and DC experiments, respectively. We were able to show that CD62P$^+$ platelets adhered only in the space between spEC within the EC layer. No CD62P signals could be observed in proximity to ltECs. Moreover, more CD62P$^+$ platelets were bound to the EC layer under SC than DC ones, indicating that shear force affects the binding of platelets to the spEC within the endothelial layer.

Table 2. Voxel classification results of the cellular mitochondria segments analysed from all ECs in each image of Fig 4.

State	Puncta	Rod	Networks	# Platelets	shown in
Static	31%	30%	39%	13	Fig 4a
	7%	18%	75%	4	Fig 4b
Dynamic	41%	32%	27%	5	Fig 4c
	14%	15%	71%	1	Fig 4d
Laser treated	22%	34%	44%	0	Fig 4e
	26%	27%	47%	0	Fig 4f

The percentage of voxels found in each class compared to the total number of voxels is presented in the column's "puncta", "rod" and "networks". The number of identified platelets for each image is presented in the column "# Platelets".
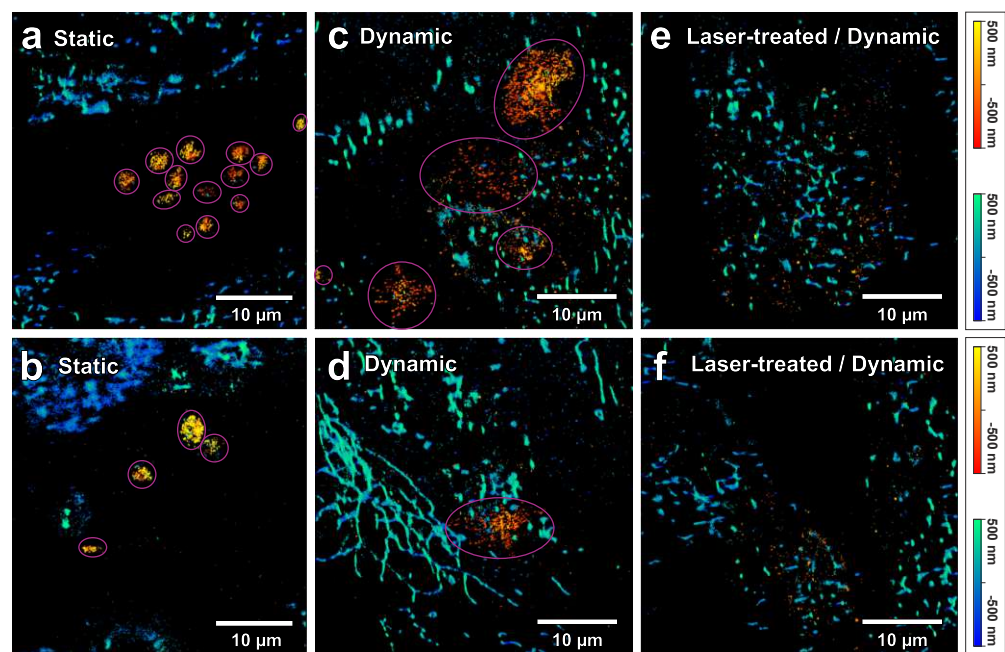
Fig 4. Two-colour 3D single-molecule localization microscopy (SMLM) images of activated platelets on an endothelial cell (EC) layer and mitochondrial networks. a) and b) show SMLM images of activated platelets and mitochondria under static conditions. The pink circles indicate identified single platelets. The "autumn" colour map (sequential increasing shades of red-orange-yellow) represents the axial position of platelets stained using anti-CD62P antibodies (conjugated to Alexa Fluor[©] 647). The positional accuracy of SMLM signals in a) was 24 nm lateral and 55 nm axial for the red channel and 39 nm lateral and 107 nm axial for the blue channel. For b) a positional accuracy of 31 nm/36 nm lateral and 69 nm/99 nm axial was calculated for the red/blue colour channel, respectively. The "winter" colour map (shades of blue to green) represents the axial positions of mitochondria (anti-Mitochondria marker conjugated to Alexa Fluor[©] 488). c) and d) display 3D two-colour SMLM reconstructions of two selected images from a dynamic experiment. Likewise, mitochondria were indicated by "winter" and platelets by "autumn" colour maps. Additionally, identified platelets are indicated by pink circles. For c) a positional accuracy of 30 nm/47 nm lateral and 46 nm/75 nm axial and for d) 28 nm/45 nm lateral and 44 nm/75 nm axial were calculated for the red/blue colour channel, respectively. e) and f) show 3D two-colour SMLM reconstructions of a region in proximity of laser-treated ECs (ltECs) under flow conditions. However, the "autumn" colour channel representing activated platelets shows only single-molecule background signals, without any indication of platelets around ltECs. For e) a positional accuracy of 30 nm/49 nm lateral and 46 nm/79 nm axial and for f) 40 nm/49 nm lateral and 63 nm/78 nm axial was calculated for the red/blue colour channel, respectively.

3D single-molecule fluorescence signals of the labelled CD62P were used to approximate the volume of individual platelets via the alpha-shapes concave hull algorithm (alpha shapes). The number of identified platelets in each image in Fig 4 is presented in Table 2. A total of 13 and 4 round-shaped platelets are displayed in Fig 4a and Fig 4b, respectively. Fig 4c shows 4 single platelets spread between spECs. Platelets under SC (N = 31 platelets) showed a spherical shape with certain aggregate formation (Fig 4a,b) presumably in the intercellular space of the EC layer. Since

platelets have to withstand shear force while interacting with spECs, larger activated platelets were observed under DC compared to SC. Only 27% of platelets activated under DC (total N = 37 platelets) had a similar volume range compared to platelets activated under SC. The statistics on volumes determined from 3D CD62P localizations are represented in Table 3. We observed 8 - 9 times larger volumes of CD62P$^+$ platelets adhering to spECs under DC (compared to SC) and a higher expression level of CD62P signals under DC (see Table 3). More precisely, 24% and 12% of total CD62P signals under SC and DC, respectively were localizations in the platelet's membrane proximity, determined via alpha shapes. Moreover, no activated platelets could be identified adherent to ltECs under DC as exemplified by Fig 4e,f. The inability of platelets to adhere suggests that these ltECs were unable to express adhesion molecules to facilitate platelet binding, presumably due to nuclear damage.

Table 3. Comparison of activated platelet volumes and densities from 3D single-molecule signals of CD62P under static and dynamic conditions.

State	# Platelets	Mean signal density per µm^3	Median platelet volume	Mean platelet volume	Platelet volume 25% quantile	Platelet volume 75% quantile
Static	31	352±30	1.4	1.6±0.22 µm^3	0.67 µm^3	1.9 µm^3
Dynamic	37	333±27	6.6	9.4±1.5 µm^3	3 µm^3	12 µm^3

Conclusion

Single-molecule localization microscopy (SMLM) enables imaging of subcellular structures and proteins with nanometre precision. Next to image reconstruction, SMLM coordinate data can be directly used to extract relevant information in a post-processing step. Thus, challenging image analysis for standard discrete images can be avoided [41]. Furthermore, the larger dataset provided by SMLM localizations allow for better statistics which can be useful for machine learning. We have previously shown that the nanometre resolution and coordinate-based analysis of 3D SMLM is well suited for statistical comparison of two-colour localization datasets [42].

In this work, we applied simultaneous two-colour 3D SMLM to study the interaction of platelets with endothelial cells (EC, indicated by mitochondria morphology). Our newly developed platform comprising microfluidics, nanoscale imaging and software tools has been applied to study platelet activation on the endothelial monolayer. In particular, we applied this platform to a blood vessel model under flow conditions. Our results showed a link between activated platelets and stressed endothelial cells determined via machine learning assisted mitochondrial morphology analysis. Filtering of outliers, background signals and residual fluorescent bleed-through was applied directly to the localized positions. 3D volume reconstruction from SMLM mitochondria localizations allowed us to use well-established algorithms for mitochondria morphology analysis while still preserving the localization data. The higher resolution of 3D mitochondria images helped to segment the mitochondrial network and reduced the complexity of pre-processing steps compared to confocal volume analysis. Based on the determined mitochondrial segments and parameters from 3D skeletonization we were able to quantify cellular stress levels of individual ECs. In addition, simultaneous two-colour SMLM has proven its utility in linking nanoscale protein distributions of CD62P (platelet activation marker) with the macroscopic mitochondria structures in 3D. Based on CD62P SMLM data we compared volumes and densities of activated platelets under static and dynamic conditions. In the future, our platform could be useful for studying thrombus formation [1], pharmacological effects [43], pathogens,

toxins [44], and other treatments at the single-cell level and provide additional insight ₁₉₃ into cellular stress. ₁₉₄

Materials and methods ₁₉₅

Microfluidics fabrication ₁₉₆

A 175 μm thick PET foil (Optimont 501, Bleher Folientechnik GmbH) was sandwiched ₁₉₇ between two double-sided adhesive tapes (Adhesive Research Arcare 90445, thickness ₁₉₈ 80 μm) for a total thickness of 335 μm. A single straight microfluidic channel ₁₉₉ (36 mm x 1.5 mm) was cut from this foil using a craft cutter (Silhouette Portrait 2) [45]. ₂₀₀ The top was sealed by an impermeable 30 μm thick PET foil (Bleher Folientechnik ₂₀₁ GmbH). Two tube connectors (EV Group) were fixed on top using double-sided ₂₀₂ adhesive tape. The bottom layer was a microscope coverslip (Menzel 24 mm x 50 mm, ₂₀₃ #1 SPEZIAL, Thermo Scientific). The coverslip enabled observation of the sample area ₂₀₄ with a high magnification/high NA objective lens. To give the chip the required rigidity, ₂₀₅ a 3 mm acrylic glass frame was fixed on top using double-sided adhesive tape. After ₂₀₆ assembly, the microfluidic chip was baked at 60 °C for 1 h. Tubing and the microfluidics ₂₀₇ chip were placed into a petri dish and properly sealed using parafilm for UV ₂₀₈ sterilization. Each side was exposed to UV light for 2 minutes (Dymax ECE, USA). ₂₀₉ Tubing, tube connectors, and acrylic frame were reused after proper washing with 1% ₂₁₀ sodium dodecyl sulfate, 70% 2-propanol and deionized water. ₂₁₁

Automated cell counting using deep learning ₂₁₂

A convolution neuronal network (CNN) was trained for the automatic segmentation of ₂₁₃ cell nuclei. The centres of nuclei were indicated by normalized 2D symmetrical Gaussian ₂₁₄ functions with a sigma of 5 pixels. The network was trained using phase-contrast ₂₁₅ images of cultivated ECs in which each nuclei centre was labelled by hand (N = 364). ₂₁₆ Images with varying EC densities and illumination settings were acquired. A standard ₂₁₇ inverted microscope (Axiovert 135, Carl Zeiss) using a 10x air phase contrast objective ₂₁₈ lens and microscopy camera (AxioCam MRc5, Carl Zeiss) was used. The architecture of ₂₁₉ our CNN is based on the residual neuronal network [46] combined with a U-Net [47,48] ₂₂₀ (4 layers deep, S3 Fig). Full-size grayscale phase contrast images (1292 x 968 pixels, ₂₂₁ 0.68 μm pixel size) and target images containing the nuclei centres were cut into smaller ₂₂₂ 128 x 128 sub-images with 50% overlap. The training was performed on a NVidia RTX ₂₂₃ 3060 graphics card (12 GB VRAM) using the Keras (TensorFlow v2.10.1) [49] backend, ₂₂₄ binary cross entropy loss function and ADAM optimizer [50]. Our CNN converged after ₂₂₅ about 9 epochs (batch size: 128, training images: 45360, validation images 5040). ₂₂₆ Full-size images (1292 x 968 pixels) were reconstructed from overlapping smooth ₂₂₇ blended predicted images (128 x 128 pixels). We used a second-order spline window ₂₂₈ function for blending with 50% overlap [51]. Positions of nuclei centres from predicted ₂₂₉ full-size images were determined by non-maximum suppression [52] (window size: ₂₃₀ 19 pixels) of the predicted Gaussian centres. Peak values also showed how certain the ₂₃₁ network was about detected cell nuclei. Based on this CNN we build a graphical user ₂₃₂ interface which allows the user to approximate the cell density during cultivation ₂₃₃ without detaching the cells. The approximate cell count can be calculated by ₂₃₄ multiplying the density with the area of the used cell culture dish. ₂₃₅

EC seeding inside a microfluidic chip ₂₃₆

Primary human ECs were differentiated from CD34$^+$ cells isolated from human cord ₂₃₇ blood [25] and were provided in frozen aliquots of 1x10^6 cells at passage five by Prof. ₂₃₈

Fabien Gosselet, Université d'Artois, France. After thawing, cells were seeded onto gelatine (0.1% in PBS)-coated 10 cm-dishes (Treated, 100×20 mm, Corning) in ECM-5 (ECM, Sciencell) supplemented with 1% endothelial cell growth supplement (Sciencell), gentamycin (50 µg/mL, Biochrom AG, ref A-2712), and 5% of preselected, heat-inactivated FBS and cultivated at 37 °C, 5% CO_2. After reaching confluency, ECs were washed 3 times with prewarmed PBS, detached with a trypsin/EDTA solution, counted, and seeded at approximately 5×10^5 cells/cm^2. Expression of the EC marker CD31/PECAM-1 was confirmed by flow cytometry (data not shown) and immunofluorescence (S4 Fig).

The UV-sterilized microfluidic chip was coated using 0.1% gelatine solution for 15 minutes at 37 °C. Next, the tubing (1.52/3.22 mm inner/outer diameter respectively, Roth) with a length of 290 cm, a peristaltic pump (Ismatec, ISM930, 4 Channel) and long needles (Sterican®, 0.80 mm $\times$ 120 mm, B. Braun) which were inserted into a sterile bioreactor tube (Tubespin® Bioreactor 50 with a septum, TPP, #86050) were attached to the microfluidic chip forming a closed loop. The tubing was filled up to the 3-way stopcock (Discofix® 3SC, B. Braun) using prewarmed ECM-5. Suspended cells (1.6×10^5 cells/mL) were transferred into the microfluidic chip via a septum connected to the perpendicular connector of the 3-way stopcock utilizing a 1 mL syringe (Omnifix®-F, B. Braun) with 0.70 mm $\times$ 30 mm needle (Sterican®, B. Braun). Next, the microfluidic chip and bioreactor tube containing the ECM-5 (5 mL) was placed into the incubator with tubing still connected to the peristaltic pump outside. The peristaltic pump was connected to a computer controlling the perfusion using custom-written software. For the first few days, the pump was active (119 µL/min) for 5 minutes every 4 h until confluence was reached. After confluence, the perfusion time was gradually increased (5 min, 10 min, 20 min, 30 min) whereas the delay time was stepwise decreased (3 h, 2 h, 1 h, 0.5 h and 0.25 h) until constant flow was reached. Cells were kept under constant flow (up to 7 days). ECM-5 within the bioreactor reservoir was changed every 2 days. Every day, cell morphology was observed by an inverted microscope (Axiovert 135, Carl Zeiss). The EC density was determined using an automated cell counting CNN from acquired phase-contrast images (as described above). Experiments were performed, in case >65% of cells orientated into flow directions (after two to seven days). EC tight junction formation was validated using fluorescent markers against CD144/VE-cadherin (S1 Fig c,d) and CD31/PECAM-1 (S4 Fig d-f).

Static cultivation of ECs

CD34$^+$ ECs were prepared as mentioned above. After confluence, ECs were washed 3 times with prewarmed PBS, detached from the 10 cm dish with trypsin/EDTA solution and counted. The middle 2 chambers of a Lab-Tek™ chambered coverglass (155382, 4 chambers, Nunc, Thermo Scientific) were coated with 0.1% gelatine solution for 15 minutes at 37 °C. ECs were seeded at approximately 3×10^5 cells/cm^2 and incubated in 900 µL ECM-5 for 4 days, the medium was exchanged every 24 h.

Human platelet concentrate

Single donor platelet concentrates were provided by the Red Cross Blood Transfusion Service (Linz, Upper Austria). All samples were collected during routine thrombocyte apheresis in accordance with the policies of the Red Cross Transfusion Service, Linz. All blood donors signed their informed consent that residual blood material can be used for research and development purposes. All experimental protocols were approved by and carried out in collaboration with the Red Cross Blood Transfusion Service, Linz.

Platelet concentrates were generated by single platelet apheresis using an automated cell separator (Trima Accel Automated Blood Collection System, TerumoBCT) at the

Red Cross Blood Transfusion Service (Linz, Upper Austria). All blood donors signed an informed consent that blood material can be used for research and the study was conducted in accordance with the policies of the Red Cross Transfusion Service. Platelets were finally stored in SSP+ (Macopharma) and ACD-A (acid citrate dextrose + adenosine, Haemonetics® anticoagulant citrate dextrose solution, Haemonetics®, Braintree) was used as an anticoagulant. 2 mL of the platelet concentrate (containing 1×10^6 platelets/µL) were aseptically transferred into a separate storage bag and experiments were carried out within 24 h after donation.

Laser-induced cell injury

A Workshop of Photonics (WOP) multiphoton lithography instrument equipped with an ultrashort pulsed laser (CARBIDE, 1 MHz repetition rate, 290 fs pulse duration, Light Conversion) with two available wavelengths (1030 nm and 515 nm) was used for cell treatment. The laser beam was focused with a $50\times$ magnification air objective lens (NA = 0.42, Mitutoyo). A 3-axis stage (AEROTECH Nanopositioner) was used for sample motion.

The medium reservoir within the bioreactor tube was exchanged with a mixture of 10% human platelet concentrate and ECM-5. The whole microfluidic chip was taken out of the incubator. Since the microfluidic chip and tubing formed a closed system, no further precautions to keep a sterile environment were necessary. After the microfluidic chip was placed within the WOP imaging chamber, flow was applied (119 µL/min) which allowed the platelets to interact with the ECs during the laser treatment. Depending on the duration of the laser experiment (max 1h), up to 5 single cells within the centre of the channel were selected and subsequently, laser treated using the 515 nm laser at 25 – 30% power 1.22 – 1.38 mW peak power in the focal plane). The ECs' nuclei were focused during the laser treatment procedure until a visual change within the cell's cytoplasm was observable or blebs formed (nuclei were treated for several seconds each). Each ltEC's position was marked on both edges of the microfluidic channel using 100% laser power. The treatment time was limited to one hour to limit the stress of all ECs due to the environmental change (temperature, gas). Afterwards, the microfluidic chip was put into the incubator at 37 °C/5% CO_2 for 15 min under flow conditions with platelets to recover.

Fluorescent labelling of P-selectin and mitochondria

For immunostaining, cells were rinsed in pre-warmed HBSS containing Ca^{2+} and Mg^{2+}. Cells were then fixed with 4% paraformaldehyde in cytoskeleton buffer with sucrose (CBS, according to a protocol of Louise Cramer [53]) for 20 min at room temperature. Cells were permeabilized in 0.5% Triton X-100 with CBS for 10 min and blocked in 10% albumin from chicken egg white (Sigma-Aldrich, Vienna, Austria) in CBS for 30 – 60 min. P-selectin (CD62P, 100 µg/mL, BioLegend) conjugated Alexa Fluor© 647 was used to stain activated platelets. Mitochondria of cells were stained using an anti-mitochondria monoclonal antibody (500 µg/mL, Sigma-Aldrich) conjugated Alexa Fluor© 488. For co-staining CD62P and mitochondria, a solution of 1:150 anti-CD62P and 1:100 anti-mitochondria antibody diluted in CBS was used to stain ECs and platelets for 1h and washed 10 times using PBS.

Fluorescence microscopy

Images were acquired using a modified Olympus IX81 inverted epi-fluorescent microscope with an oil-immersion objective lens (PlanApo N, $60\times$, NA 1.42, Olympus). Samples were mounted on a XYZ piezo stage (PI Mars; P-562.3CD, Physical

Instruments) which has nanometre accuracy, combined with a coarse mechanical stage ₃₃₅
with a travel range of 1 cm × 1 cm (Hybrid, JPK Instruments). A tube lens with an ₃₃₆
additional magnification of 1.6 was used to achieve a final imaging magnification of 96 ₃₃₇
(corresponding to a pixel size of 167 nm). Cells were illuminated with a 640 nm ₃₃₈
solid-state laser (diode-pumped, iBeam Smart, Toptica Photonics) and a 488 nm laser ₃₃₉
(diode-pumped, iBeam Smart, Toptica Photonics). Signals were collected using an ₃₄₀
Andor iXonEM+ 897 (back-illuminated) EMCCD camera (16 µm pixel size). The ₃₄₁
following filter sets were used: dichroic filter (ZT405/488/561/ 640rpc, Chroma ₃₄₂
Technology GmbH), emission filter (446/523/600/677 nm BrightLine quad-band ₃₄₃
band-pass filter, Semrock, Rochester), and additional emission filters: ET 700/75 M, ₃₄₄
Chroma Technology GmbH; ET 525/50 M, Chroma Technology GmbH. For 3D ₃₄₅
measurements, a cylindrical lens (f = 1000 mm, Thorlabs) was placed into the optical ₃₄₆
detection pathway of the microscope. ₃₄₇

Two-colour 3D SMLM imaging ₃₄₈

Simultaneous imaging of the cell's mitochondria, as well as the activation of platelets, ₃₄₉
were measured using a two-colour beam splitter (OptoSplit II; Cairn Research) with a ₃₅₀
filter cube for 675 nm and 525 nm (ET 525/50, H568LPXR, HC 675/67, AHF). Both ₃₅₁
colour channels were projected onto the same camera chip but spatially separated into ₃₅₂
two non-overlapping spectral channels. To achieve nanometre accuracy, we applied ₃₅₃
direct stochastic optical reconstruction microscopy (dSTORM) [54]. A cylindrical lens ₃₅₄
in the optical detection pathway of the microscope introduced astigmatism and allowed ₃₅₅
for 3D imaging. Axial-depended deformation of the point spread function (PSF) was ₃₅₆
calibrated using a sample of homogeneous distrusted TetraSpeck™ beads (0.1 µm, ₃₅₇
Invitrogen) that were moved along the axial axis at defended steps (10 nm) over a range ₃₅₈
of 200 frames. Since astigmatism depends on the wavelength, both colour channels were ₃₅₉
simultaneously acquired but calibration curves were separately calculated. For imaging, ₃₆₀
samples were illuminated for 20 ms using both 640 nm and 488 nm lasers at a frame ₃₆₁
rate of 20 images/s. All illumination protocols were controlled using custom-written ₃₆₂
acquisition software. For image reconstruction, a sequence of 10 000 – 20 000 images ₃₆₃
were recorded, and the single-molecule signals were analysed using custom-written ₃₆₄
software [42]. The two-colour channel regions provided from the calibration images were ₃₆₅
roughly overlaid. These regions were further used for analysis of each subsequent ₃₆₆
dSTORM experiment and were the bases for combining the channels. After all ₃₆₇
single-molecule signals were localized, both channels are combined into one dataset ₃₆₈
without subpixel chromatic correction. Single-molecule signals with intensities below ₃₆₉
500 photons as well as a lateral positional accuracy above 75 nm were discarded. The ₃₇₀
datasets were drift-corrected using the redundancy cross-correlation (RCC) method [40]. ₃₇₁
Due to a small overlap of the Alexa Fluor© 488 emission and the 675/67 nm filter, ₃₇₂
fluorescent bleed-through had to be corrected. Therefore, random forest ₃₇₃
classification [39]; to identify single-molecule signals in the Alexa Fluor© 647 channel ₃₇₄
that were emitted from Alexa Fluor© 488 signals were utilized. A custom-written ₃₇₅
software enabled the categorization of rendered Alexa Fluor© 647 SMLM images using ₃₇₆
a brush tool into two classes – certain signals coming from Alexa Fluor© 647 and Alexa ₃₇₇
Fluor© 488 signals from bleed-through. Features used for the random forest ₃₇₈
classification included frame number, intensity, background, background error, sigma x ₃₇₉
& y and a 3×3 pixel grid of intensity values from the original image around the signal's ₃₈₀
position in both colour channels. Random forest classification was then trained and ₃₈₁
fluorescence data that were not classified as originating from Alexa Fluor© 647 channel ₃₈₂
were discarded. Finally, the two-colour images were rendered using "autumn" and ₃₈₃
"winter" colour maps (adapted from MATLAB©) illustrating the axial positions. Each ₃₈₄
signal was rendered as a symmetrical Gaussian function. ₃₈₅

Mitochondria classification

To classify mitochondrial morphology into puncture, rod and network structures, localizations from 3D SMLM had to be converted into 3D volumes. Localizations with lateral and axial positional accuracies of 100 nm and 150 nm, respectively, were filtered. Furthermore, background localizations with insufficient neighbours (density: 0.65 signals/µm³) within a radius of 250 nm were also filtered out. For volume reconstruction, image stacks with a voxel size of 85 nm x 85 nm x 25 nm and 8-bit grayscale colour depth were chosen. A lower axial voxel size was used to compensate for higher axial positional accuracies and the maximum depth (1000 nm) archivable of 3D astigmatism SMLM. Each localization was rendered using an anisotropic 3D Gaussian function, with its sigma dependent on the calculated positional accuracy. Next, the volume data was smoothed using a symmetrical 3D Gaussian filter with a sigma of 1.5 and a window size of 7. These smoothed volumes were then thresholded using a GPU (Cuda, NVIDIA) accelerated adaptive local threshold approach. Herein, for each voxel, the histogram within a box of $11 \times 11 \times 11$ voxels was calculated and the threshold for this voxel was determined by the intermeans (also called iso-data) algorithm [55]. Based on the work of Lee et al. [56] and the ImageJ plugin "Skeletonize3D" by Ignacio Arganda-Carreras et al., a C++ implementation was created and used to calculate the 3D medial axis or also call "skeleton" from the threshold volumes. The skeleton was analysed and segmented using a C++ implementation of the ImageJ plugin "AnalyzeSkeleton" from [36]. Additionally, the volume of each mitochondria segment was reconstructed from the threshold volume using the flood-fill method and volumes with less than 50 detected voxels (originating from mitochondria signals) were discarded. Furthermore, each segment which represents either the skeleton of a single mitochondrion or a cluster of mitochondria was classified into puncture, rod, and networks using random forest classification (parameters: number of branches, number of endpoints, number of junctions, number of slabs, number of triples, number of quadruples, average branch length, maximum branch length, the shortest path, number of voxels, width, height, depth). Training data was generated by manual classification of 2 123 segments. During training, the selected sample size was enough for a reliable classification of unseen mitochondrial segments. In a final step, the percentage of voxels in each class was calculated for each EC or cluster of ECs.

Platelet's volume and density determination

Platelet's volume and density were determined from 3D SMLM data of CD62P signals. The membrane of individual platelets was approximated via alpha-shapes concave hull algorithm using a MATLAB© script (release 2020b). An alpha value of 1 µm was chosen, and the single-molecule signal densities were calculated from the CD62P signals found within the calculated volume. To determine the number of CD62P signals in the proximity of the platelet's membrane, the alpha shape hull was shrunken by 60 nm and the number of signals within the shrunken volume was determined. The percentages of CD62P signals in membrane proximity (with a 30 nm radius) were calculated by subtracting the signals within the shrunken hull from the total number of determined CD62P signals (N) and normalized by N.

Supporting information

S1 Fig. Simultaneous two-colour 3D single-molecule localization microscopy images of adherence junctions of endothelial cells (ECs) and platelets on an endothelial monolayer The "autumn" colour map visualizes the

axial positions (yellow above focus, red below focus) of adherence junctions labelled with anti-CD144 (VE-cadherin) conjugated to Alexa Fluor© 647. The "winter" colour map visualizes the axial positions (green above focus, blue below focus) of the surface protein CD41 with anti-CD41 conjugated to Alexa Fluor© 488. Colour channels are pixelwise aligned and single-molecules were rendered with a width of 30 nm. a), b) shows a HUVEC/Tert2 and c), d) CD34$^+$ endothelial cell, both cultivated within a microfluidic chip under flow conditions (flow rate 119 µL/min) for 48h. Platelets were incubated under flow conditions for 15 min at 37°C.

S2 Fig.   Platelet test experiments under flow conditions. a) displays a bright-field microscopy image of an EC monolayer and platelets flowing above. The arrows indicate the movement of single platelets over 4 frames (start: orange, end: red). The positions of platelets were tracked using trackpy. In b) an overlay of two fluorescent images of platelets on CD34$^+$ ECs under flow conditions co-stained with anti-CD41 antibodies conjugated to Alexa Fluor© 488 (blue) and anti-CD62P antibodies conjugated to Alexa Fluor© 647 (red) is shown.

S3 Fig.   General approach for cell nuclei segmentation and UNet architecture. a) The network receives a 128x128 sub image of endothelial cells imaged using phase contrast microscopy. Its output is the predicted cell nuclei as 2D symmetrical Gaussian function (sigma 5 pixels). Based on these predicted Gaussian functions positions are calculated via non-maximum suppression. b) shows the network architecture which is a combination of residual neuronal networks and U-Net. The network consists of 2 030 817 trainable parameters.

S4 Fig.   Fluorescent images of the endothelial cell-cell adhesion protein PECAM-1 stained with anti-CD31 conjugated to Alexa Fluor© 647. a)-c) shows a HUVEC/Tert2 and d)-f) shows CD34$^+$ primary human endothelial cell, both cultivated within a microfluidic chip under flow conditions (flow rate 119 µL/min) for 48h.

S1 Video.   Bright-field microscopy image sequence of platelet added to the flow of the developed microfluidic chip seeded with a HUVEC/Tert2 monolayer. Images were acquired at 0.48 Hz and platelets were propelled by hydrostatic force by filling only one tube connector with 1:10 diluted platelet concentrate with HUVEC/Tert2 medium. The platelet positions of the first 30 frames were analysed using trackpy and a mean platelet velocity of 5.8 µm/s was calculated.

S2 Video.   Fluorescence image sequence of platelet flowing above a HUVEC/Tert2 monolayer within the developed microfluidic chip. The image sequence was acquired at 0.1 Hz. Platelets were propelled by hydrostatic force by filling only one tube connector with 1:10 diluted platelet concentrate with HUVEC/Tert2 medium. Additionally, the medium is stained using 1:100 diluted Anit-CD41 antibodies (conjugated to Alexa Fluor© 488).

Acknowledgments

Conflicts of interest

There are no conflicts to declare.

Data availability statement

All code files are available from the NanoMito3D-Platform Github repository at `https://github.com/CURTLab/NanoMito3D-Platform`. All localization data files and machine learning models are available from the Github release.

Author Contributions

Conceptualization: Jaroslaw Jacak, Fabian Hauser.
Data curation: Fabian Hauser.
Formal analysis: Fabian Hauser.
Funding acquisition: Jaroslaw Jacak.
Investigation: Fabian Hauser, Sandra Milic, Christoph Naderer, Boris Buchroithner.
Methodology: Fabian Hauser, Jaroslaw Jacak, Eleni Priglinger.
Project administration: Jaroslaw Jacak.
Resources: Anja Peterbauer, Eleni Priglinger.
Software: Fabian Hauser.
Supervision: Jaroslaw Jacak, Heinz Redl.
Validation: Fabian Hauser, Jaroslaw Jacak, Eleni Priglinger, Michael B. Fischer.
Visualization: Fabian Hauser.
Writing – original draft: Fabian Hauser.
Writing – Review & Editing: Fabian Hauser, Jaroslaw Jacak, Eleni Priglinger, Michael B. Fischer, Heinz Redl.

References

1. Tsai M, Kita A, Leach J, Rounsevell R, Huang JN, Moake J, et al. In vitro modeling of the microvascular occlusion and thrombosis that occur in hematologic diseases using microfluidic technology. Journal of Clinical Investigation. 2012;122(1):408–418. doi:10.1172/JCI58753.

2. Brass LF, Tomaiuolo M, Welsh J, Poventud-Fuentes I, Zhu L, Diamond SL, et al. Hemostatic Thrombus Formation in Flowing Blood. 4th ed. Elsevier Inc.; 2019.

3. Oshinowo O, Lambert T, Sakurai Y, Copeland R, Hansen CE, Lam WA, et al. Getting a good view: in vitro imaging of platelets under flow. Platelets. 2020;00(00):570–579. doi:10.1080/09537104.2020.1732320.

4. Buchegger B, Tanzer A, Posch S, Gabriel C, Klar TA, Jacak J. STED lithography in microfluidics for 3D thrombocyte aggregation testing. Journal of Nanobiotechnology. 2021;19(1):23. doi:10.1186/s12951-020-00762-8.

5. Dupuy A, Hagimola L, Mgaieth NSA, Houlahan CB, Preketes-Tardiani RE, Coleman PR, et al. Thromboinflammation model-on-a-chip by whole blood microfluidics on fixed human endothelium. Diagnostics. 2021;11(2):1–14. doi:10.3390/diagnostics11020203.

6. Jain A, Graveline A, Waterhouse A, Vernet A, Flaumenhaft R, Ingber DE. A shear gradient-activated microfluidic device for automated monitoring of whole

blood haemostasis and platelet function. Nature Communications. 2016;7:1–10. doi:10.1038/ncomms10176.

7. Vink H, Constantinescu AA, Spaan JAE. Oxidized Lipoproteins Degrade the Endothelial Surface Layer. Circulation. 2000;101(13):1500–1502. doi:10.1161/01.CIR.101.13.1500.

8. Neubauer K, Zieger B. Endothelial cells and coagulation. Cell and Tissue Research. 2021;(0123456789). doi:10.1007/s00441-021-03471-2.

9. Sebastian B, Dittrich PS. Microfluidics to Mimic Blood Flow in Health and Disease. Annual Review of Fluid Mechanics. 2018;50(October 2017):483–504. doi:10.1146/annurev-fluid-010816-060246.

10. Jackson SP. The growing complexity of platelet aggregation. Blood. 2007;109(12):5087–5095. doi:10.1182/blood-2006-12-027698.

11. Montague SJ, Lim YJ, Lee WM, Gardiner EE. Imaging Platelet Processes and Function—Current and Emerging Approaches for Imaging in vitro and in vivo. Frontiers in Immunology. 2020;11(January). doi:10.3389/fimmu.2020.00078.

12. Cognasse F, Laradi S, Berthelot P, Bourlet T, Marotte H, Mismetti P, et al. Platelet inflammatory response to stress. Frontiers in Immunology. 2019;10(JUN):1–10. doi:10.3389/fimmu.2019.01478.

13. Wootton DM, Ku DN. Fluid Mechanics of Vascular Systems, Diseases, and Thrombosis. Annual Review of Biomedical Engineering. 1999;1(1):299–329. doi:10.1146/annurev.bioeng.1.1.299.

14. Furie B, Furie BC. Mechanisms of Thrombus Formation. New England Journal of Medicine. 2008;359(9):938–949. doi:10.1056/NEJMra0801082.

15. Yau JW, Teoh H, Verma S. Endothelial cell control of thrombosis. BMC Cardiovascular Disorders. 2015;15(1):1–11. doi:10.1186/s12872-015-0124-z.

16. Li Y, Montague SJ, Brüstle A, He X, Gillespie C, Gaus K, et al. High contrast imaging and flexible photomanipulation for quantitative in vivo multiphoton imaging with polygon scanning microscope. Journal of Biophotonics. 2018;11(7):303–325. doi:10.1002/jbio.201700341.

17. Eisner V, Picard M, Hajnóczky G. Mitochondrial dynamics in adaptive and maladaptive cellular stress responses. Nature Cell Biology. 2018;20(7):755–765. doi:10.1038/s41556-018-0133-0.

18. Neutelings T, Lambert CA, Nusgens BV, Colige AC. Effects of Mild Cold Shock (25°C) Followed by Warming Up at 37°C on the Cellular Stress Response. PLoS ONE. 2013;8(7):1–15. doi:10.1371/journal.pone.0069687.

19. Valente AJ, Fonseca J, Moradi F, Foran G, Necakov A, Stuart JA. Quantification of Mitochondrial Network Characteristics in Health and Disease. vol. 1158 of Advances in Experimental Medicine and Biology. Singapore: Springer Singapore; 2019. p. 183–196.

20. Zahedi A, On V, Phandthong R, Chaili A, Remark G, Bhanu B, et al. Deep Analysis of Mitochondria and Cell Health Using Machine Learning. Scientific Reports. 2018;8(1):1–15. doi:10.1038/s41598-018-34455-y.

21. Chu CH, Tseng WW, Hsu CM, Wei AC. Image Analysis of the Mitochondrial Network Morphology With Applications in Cancer Research. Frontiers in Physics. 2022;10(April):1–16. doi:10.3389/fphy.2022.855775.

22. Valente AJ, Maddalena LA, Robb EL, Moradi F, Stuart JA. A simple ImageJ macro tool for analyzing mitochondrial network morphology in mammalian cell culture. Acta Histochemica. 2017;119(3):315–326. doi:10.1016/j.acthis.2017.03.001.

23. Chaudhry A, Shi R, Luciani DS. A pipeline for multidimensional confocal analysis of mitochondrial morphology, function, and dynamics in pancreatic β-cells. American Journal of Physiology-Endocrinology and Metabolism. 2020;318(2):E87–E101. doi:10.1152/ajpendo.00457.2019.

24. Harwig MC, Viana MP, Egner JM, Harwig JJ, Widlansky ME, Rafelski SM, et al. Methods for imaging mammalian mitochondrial morphology: A prospective on MitoGraph. Analytical Biochemistry. 2018;552:81–99. doi:10.1016/j.ab.2018.02.022.

25. Cecchelli R, Aday S, Sevin E, Almeida C, Culot M, Dehouck L, et al. A Stable and Reproducible Human Blood-Brain Barrier Model Derived from Hematopoietic Stem Cells. PLoS ONE. 2014;9(6):e99733. doi:10.1371/journal.pone.0099733.

26. Pisapia F, Balachandran W, Rasekh M. Organ-on-a-Chip: Design and Simulation of Various Microfluidic Channel Geometries for the Influence of Fluid Dynamic Parameters. Applied Sciences. 2022;12(8):3829. doi:10.3390/app12083829.

27. Poon C. Measuring the density and viscosity of culture media for optimized computational fluid dynamics analysis of in vitro devices. Journal of the Mechanical Behavior of Biomedical Materials. 2022;126(December 2021):105024. doi:10.1016/j.jmbbm.2021.105024.

28. Roux E, Bougaran P, Dufourcq P, Couffinhal T. Fluid Shear Stress Sensing by the Endothelial Layer. Frontiers in Physiology. 2020;11(July):1–17. doi:10.3389/fphys.2020.00861.

29. Pedroso DCS, Tellechea A, Moura L, Fidalgo-Carvalho I, Duarte J, Carvalho E, et al. Improved Survival, Vascular Differentiation and Wound Healing Potential of Stem Cells Co-Cultured with Endothelial Cells. PLoS ONE. 2011;6(1):e16114. doi:10.1371/journal.pone.0016114.

30. Fina L, Molgaard H, Robertson D, Bradley N, Monaghan P, Delia D, et al. Expression of the CD34 gene in vascular endothelial cells. Blood. 1990;75(12):2417–2426. doi:10.1182/blood.v75.12.2417.2417.

31. Yang J, Ii M, Kamei N, Alev C, Kwon SM, Kawamoto A, et al. CD34+ Cells Represent Highly Functional Endothelial Progenitor Cells in Murine Bone Marrow. PLoS ONE. 2011;6(5):e20219. doi:10.1371/journal.pone.0020219.

32. Buchroithner B, Mayr S, Hauser F, Priglinger E, Stangl H, Santa-Maria AR, et al. Dual Channel Microfluidics for Mimicking the Blood–Brain Barrier. ACS Nano. 2021;15(2):2984–2993. doi:10.1021/acsnano.0c09263.

33. Wickman GR, Julian L, Mardilovich K, Schumacher S, Munro J, Rath N, et al. Blebs produced by actin-myosin contraction during apoptosis release damage-associated molecular pattern proteins before secondary necrosis occurs. Cell Death and Differentiation. 2013;20(10):1293–1305. doi:10.1038/cdd.2013.69.

34. Davidson SM, Duchen MR. Endothelial mitochondria: Contributing to vascular function and disease. Circulation Research. 2007;100(8):1128–1141. doi:10.1161/01.RES.0000261970.18328.1d.

35. Tang X, Luo YX, Chen HZ, Liu DP. Mitochondria, endothelial cell function, and vascular diseases. Frontiers in Physiology. 2014;5 MAY(May):1–17. doi:10.3389/fphys.2014.00175.

36. Arganda-Carreras I, Fernández-González R, Muñoz-Barrutia A, Ortiz-De-Solorzano C. 3D reconstruction of histological sections: Application to mammary gland tissue. Microscopy Research and Technique. 2010;73(11):1019–1029. doi:10.1002/jemt.20829.

37. Leo Breiman. Random Forests. Machine Learning. 2001;45:5–32. doi:10.1023/A:1010933404324.

38. Lorensen WE, Cline HE. Marching cubes: A high resolution 3D surface construction algorithm. In: Proceedings of the 14th annual conference on Computer graphics and interactive techniques - SIGGRAPH '87. May. New York, New York, USA: ACM Press; 1987. p. 163–169.

39. Leonard AP, Cameron RB, Speiser JL, Wolf BJ, Peterson YK, Schnellmann RG, et al. Quantitative analysis of mitochondrial morphology and membrane potential in living cells using high-content imaging, machine learning, and morphological binning. Biochimica et Biophysica Acta - Molecular Cell Research. 2015;1853(2):348–360. doi:10.1016/j.bbamcr.2014.11.002.

40. Wang KN, Shao X, Tian Z, Liu LY, Zhang C, Tan CP, et al. A Continuous Add-On Probe Reveals the Nonlinear Enlargement of Mitochondria in Light-Activated Oncosis. Advanced Science. 2021;8(17):1–11. doi:10.1002/advs.202004566.

41. Strohmeier K, Hofmann M, Jacak J, Narzt MS, Wahlmueller M, Mairhofer M, et al. Multi-Level Analysis of Adipose Tissue Reveals the Relevance of Perivascular Subpopulations and an Increased Endothelial Permeability in Early-Stage Lipedema. Biomedicines. 2022;10(5). doi:10.3390/biomedicines10051163.

42. Mayr S, Hauser F, Puthukodan S, Axmann M, Göhring J, Jacak J. Statistical analysis of 3D localisation microscopy images for quantification of membrane protein distributions in a platelet clot model. PLOS Computational Biology. 2020;16(6):e1007902. doi:10.1371/journal.pcbi.1007902.

43. Bieberich AA, Rajwa B, Irvine A, Fatig RO, Fekete A, Jin H, et al. Acute cell stress screen with supervised machine learning predicts cytotoxicity of excipients. Journal of Pharmacological and Toxicological Methods. 2021;111(May):107088. doi:10.1016/j.vascn.2021.107088.

44. Fulda S, Gorman AM, Hori O, Samali A. Cellular Stress Responses: Cell Survival and Cell Death. International Journal of Cell Biology. 2010;2010:1–23. doi:10.1155/2010/214074.

45. Kokalj T, Park Y, Vencelj M, Jenko M, Lee LP. Self-powered Imbibing Microfluidic Pump by Liquid Encapsulation: SIMPLE. Lab Chip. 2014;14(22):4329–4333. doi:10.1039/C4LC00920G.

46. Hesh CA, Qiu Y, Lam WA. Vascularized microfluidics and the blood-endothelium interface. Micromachines. 2020;11(1):1–27. doi:10.3390/mi11010018.

47. Falk T, Mai D, Bensch R, Çiçek Ö, Abdulkadir A, Marrakchi Y, et al. U-Net: deep learning for cell counting, detection, and morphometry. Nature Methods. 2019;16(1):67–70. doi:10.1038/s41592-018-0261-2.

48. Xie W, Noble JA, Zisserman A. Microscopy cell counting and detection with fully convolutional regression networks. Computer Methods in Biomechanics and Biomedical Engineering: Imaging and Visualization. 2018;6(3):283–292. doi:10.1080/21681163.2016.1149104.

49. Chollet F. Keras; 2015. Available from: `https://keras.io`.

50. Kingma DP, Ba JL. Adam: A method for stochastic optimization. 3rd International Conference on Learning Representations, ICLR 2015 - Conference Track Proceedings. 2015; p. 1–15.

51. Chevalier G. Vooban/Smoothly-Blend-Image-Patches: Using a U-Net for image segmentation, blending predicted patches smoothly is a must to please the human eye.; 2017. Available from: `https://github.com/Vooban/Smoothly-Blend-Image-Patches`.

52. Neubeck A, Van Gool L. Efficient Non-Maximum Suppression. In: 18th International Conference on Pattern Recognition (ICPR'06). vol. 3. IEEE; 2006. p. 850–855.

53. Symons MH, Mitchison TJ. Control of actin polymerization in live and permeabilized fibroblasts. Journal of Cell Biology. 1991;114(3):503–513. doi:10.1083/jcb.114.3.503.

54. Heilemann M, van de Linde S, Schüttpelz M, Kasper R, Seefeldt B, Mukherjee A, et al. Subdiffraction-Resolution Fluorescence Imaging with Conventional Fluorescent Probes. Angewandte Chemie International Edition. 2008;47(33):6172–6176. doi:10.1002/anie.200802376.

55. Ridler TW, Calvard S. Picture Thresholding Using an Iterative Selection Method. IEEE Transactions on Systems, Man, and Cybernetics. 1978;8(8):630–632. doi:10.1109/TSMC.1978.4310039.

56. Lee TC, Kashyap RL, Chu CN. Building Skeleton Models via 3-D Medial Surface Axis Thinning Algorithms. CVGIP: Graphical Models and Image Processing. 1994;56(6):462–478. doi:10.1006/cgip.1994.1042.

List of References

1.   E. Abbe: "Beiträge zur Theorie des Mikroskops und der mikroskopischen Wahrnehmung." *Arch. für Mikroskopische Anat.* vol. 9, no. 1, pp. 413–418, 1873.

2.   K. Greger, J. Swoger, and E.H.K. Stelzer: "Basic building units and properties of a fluorescence single plane illumination microscope." *Rev. Sci. Instrum.* vol. 78, no. 2, 2007.

3.   K.N. Fish: "Total Internal Reflection Fluorescence (TIRF) Microscopy." *Curr. Protoc. Cytom.* vol. 50, no. 1, pp. 273–275, 2009.

4.   Z. Zhang, Y. Wang, R. Piestun, and Z. Huang: "Characterizing and correcting camera noise in back-illuminated sCMOS cameras." *Opt. Express*. vol. 29, no. 5, pp. 6668, 2021.

5.   Y. Wang, L. Zhao, Z. Hu, Y. Wang, Z. Zhao, L. Li, and Z.-L. Huang: "Quantitative performance evaluation of a back-illuminated sCMOS camera with 95% QE for super-resolution localization microscopy." *Cytom. Part A*. vol. 91, no. 12, pp. 1175–1183, 2017.

6.   B. Mandracchia, X. Hua, C. Guo, J. Son, T. Urner, and S. Jia: "Fast and accurate sCMOS noise correction for fluorescence microscopy." *Nat. Commun.* vol. 11, no. 1, pp. 1–12, 2020.

7.   B.L. Sprague, R.L. Pego, D.A. Stavreva, and J.G. McNally: "Analysis of Binding Reactions by Fluorescence Recovery after Photobleaching." *Biophys. J.* vol. 86, no. 6, pp. 3473–3495, 2004.

8.   M. Moertelmaier, M. Brameshuber, M. Linimeier, G.J. Schütz, and H. Stockinger: "Thinning out clusters while conserving stoichiometry of labeling." *Appl. Phys. Lett.* vol. 87, no. 26, pp. 1–3, 2005.

9.   P.R. Nicovich, J. Walsh, T. Böcking, and K. Gaus: "NicoLase—An open-source diode laser combiner, fiber launch, and sequencing controller for fluorescence microscopy." *PLoS One*. vol. 12, no. 3, pp. e0173879, 2017.

10.   P. Almada, P.M. Pereira, S. Culley, G. Caillol, F. Boroni-Rueda, C.L. Dix, G. Charras, B. Baum, R.F. Laine, C. Leterrier, and R. Henriques: "Automating multimodal microscopy with NanoJ-Fluidics." *Nat. Commun.* vol. 10, no. 1, pp. 1223, 2019.

11.   Max Born and Emil Wolf: "Principles of Optics: Electromagnetic Theory of Propagation, Interference and Diffraction of Light." , 1980.

12.   T.A. Klar, S. Jakobs, M. Dyba, A. Egner, and S.W. Hell: "Fluorescence microscopy with diffraction resolution barrier broken by stimulated emission." *Proc. Natl. Acad. Sci.* vol. 97, no. 15, pp. 8206–8210, 2000.

13.   S. Puthukodan, E. Murtezi, J. Jacak, and T.A. Klar: "Localization STED (LocSTED) microscopy with 15 nm resolution." *Nanophotonics*. vol. 9, no. 4, pp. 783–792, 2020.

14.   R. Schmidt, T. Weihs, C.A. Wurm, I. Jansen, J. Rehman, S.J. Sahl, and S.W. Hell: "MINFLUX nanometer-scale 3D imaging and microsecond-range tracking on a common fluorescence microscope." *Nat. Commun.* vol. 12, no. 1, pp. 1–12, 2021.

15.   W.E. Moerner and L. Kador: "Optical detection and spectroscopy of single molecules in a solid." *Phys. Rev. Lett.* vol. 62, no. 21, pp. 2535–2538, 1989.

16.   R.M. Dickson, A.B. Cubitt, R.Y. Tsien, and W.E. Moerner: "On/off blinking and switching behaviour of single molecules of green fluorescent protein." *Nature*. vol. 388, no. 6640, pp. 355–358, 1997.

17.   E. Betzig, G.H. Patterson, R. Sougrat, O.W. Lindwasser, S. Olenych, J.S. Bonifacino,

M.W. Davidson, J. Lippincott-Schwartz, and H.F. Hess: "Imaging intracellular fluorescent proteins at nanometer resolution." *Science (80-.).* vol. 313, no. 5793, pp. 1642–1645, 2006.

18. M.J. Rust, M. Bates, and X. Zhuang: "Sub-diffraction-limit imaging by stochastic optical reconstruction microscopy (STORM)." *Nat. Methods*. vol. 3, no. 10, pp. 793–796, 2006.

19. M. Heilemann, S. van de Linde, M. Schüttpelz, R. Kasper, B. Seefeldt, A. Mukherjee, P. Tinnefeld, and M. Sauer: "Subdiffraction-Resolution Fluorescence Imaging with Conventional Fluorescent Probes." *Angew. Chemie Int. Ed.* vol. 47, no. 33, pp. 6172–6176, 2008.

20. T. Dertinger, R. Colyer, G. Iyer, S. Weiss, and J. Enderlein: "Fast, background-free, 3D super-resolution optical fluctuation imaging (SOFI)." *Proc. Natl. Acad. Sci.* vol. 106, no. 52, pp. 22287–22292, 2009.

21. A. Sharonov and R.M. Hochstrasser: "Wide-field subdiffraction imaging by accumulated binding of diffusing probes." *Proc. Natl. Acad. Sci.* vol. 103, no. 50, pp. 18911–18916, 2006.

22. G.J. Schütz, M. Axmann, and H. Schindler: "Imaging Single Molecules in Three Dimensions." *Single Mol.* vol. 2, no. 2, pp. 69–74, 2001.

23. B. Huang, W. Wang, M. Bates, and X. Zhuang: "Three-Dimensional Super-Resolution Imaging by Stochastic Optical Reconstruction Microscopy." *Science (80-.).* vol. 319, no. 5864, pp. 810–813, 2008.

24. M.F. Juette, T.J. Gould, M.D. Lessard, M.J. Mlodzianoski, B.S. Nagpure, B.T. Bennett, S.T. Hess, and J. Bewersdorf: "Three-dimensional sub-100 nm resolution fluorescence microscopy of thick samples." *Nat. Methods*. vol. 5, no. 6, pp. 527–529, 2008.

25. S.R.P. Pavani, M. a Thompson, J.S. Biteen, S.J. Lord, N. Liu, R.J. Twieg, R. Piestun, and W.E. Moerner: "Three-dimensional, single-molecule fluorescence imaging beyond the diffraction limit by using a double-helix point spread function." *Proc. Natl. Acad. Sci.* vol. 106, no. 9, pp. 2995–2999, 2009.

26. Y. Shechtman, S.J. Sahl, A.S. Backer, and W.E. Moerner: "Optimal Point Spread Function Design for 3D Imaging." *Phys. Rev. Lett.* vol. 113, no. 13, pp. 133902, 2014.

27. M. Klessinger: "Konstitution und Lichtabsorption organischer Farbstoffe." *Chemie unserer Zeit*. vol. 12, no. 1, pp. 1–11, 1978.

28. B. Turkowyd, D. Virant, and U. Endesfelder: "From single molecules to life: microscopy at the nanoscale." *Anal. Bioanal. Chem.* vol. 408, no. 25, pp. 6885–6911, 2016.

29. S. Kim, J. Chen, T. Cheng, A. Gindulyte, J. He, S. He, Q. Li, B.A. Shoemaker, P.A. Thiessen, B. Yu, L. Zaslavsky, J. Zhang, and E.E. Bolton: "PubChem 2023 update." *Nucleic Acids Res.* vol. 51, no. D1, pp. D1373–D1380, 2023.

30. N.M. O'Boyle, M. Banck, C.A. James, C. Morley, T. Vandermeersch, and G.R. Hutchison: "Open Babel: An open chemical toolbox." *J. Cheminform.* vol. 3, no. 1, pp. 33, 2011.

31. R. Liu, X. Gao, M. Barbatti, J. Jiang, and G. Zhang: "Promoting Intersystem Crossing of a Fluorescent Molecule via Single Functional Group Modification." *J. Phys. Chem. Lett.* vol. 10, no. 6, pp. 1388–1393, 2019.

32. M.C. DeRosa and R.J. Crutchley: "Photosensitized singlet oxygen and its applications." *Coord. Chem. Rev.* vol. 233–234, pp. 351–371, 2002.

33. C.E. Aitken, R.A. Marshall, and J.D. Puglisi: "An Oxygen Scavenging System for Improvement of Dye Stability in Single-Molecule Fluorescence Experiments." *Biophys. J.* vol. 94, no. 5, pp. 1826–1835, 2008.

34. A. Keppler, S. Gendreizig, T. Gronemeyer, H. Pick, H. Vogel, and K. Johnsson: "A

general method for the covalent labeling of fusion proteins with small molecules in vivo." *Nat. Biotechnol.* vol. 21, no. 1, pp. 86–89, 2003.

35. A. Keppler, M. Kindermann, S. Gendreizig, H. Pick, H. Vogel, and K. Johnsson: "Labeling of fusion proteins of O6-alkylguanine-DNA alkyltransferase with small molecules in vivo and in vitro." *Methods*. vol. 32, no. 4, pp. 437–444, 2004.

36. W. Schroeder, K. Martin, and B. Lorensen: "The Visualization Toolkit." Visualization Handbook. pp. 593–614. *Elsevier* (2006).

37. H.M. Berman: "The Protein Data Bank." *Nucleic Acids Res.* vol. 28, no. 1, pp. 235–242, 2000.

38. M. Ormö, A.B. Cubitt, K. Kallio, L.A. Gross, R.Y. Tsien, and S.J. Remington: "Crystal Structure of the Aequorea victoria Green Fluorescent Protein." *Science (80-.)*. vol. 273, no. 5280, pp. 1392–1395, 1996.

39. L.J. Harris, S.B. Larson, K.W. Hasel, and A. McPherson: "Refined Structure of an Intact IgG2a Monoclonal Antibody." *Biochemistry*. vol. 36, no. 7, pp. 1581–1597, 1997.

40. S. Pospich, F. Merino, and S. Raunser: "Structural Effects and Functional Implications of Phalloidin and Jasplakinolide Binding to Actin Filaments." *Structure*. vol. 28, no. 4, pp. 437-449.e5, 2020.

41. A. Gautier, A. Juillerat, C. Heinis, I.R. Corrêa, M. Kindermann, F. Beaufils, and K. Johnsson: "An Engineered Protein Tag for Multiprotein Labeling in Living Cells." *Chem. Biol.* vol. 15, no. 2, pp. 128–136, 2008.

42. J.B. Grimm, B.P. English, J. Chen, J.P. Slaughter, Z. Zhang, A. Revyakin, R. Patel, J.J. Macklin, D. Normanno, R.H. Singer, T. Lionnet, and L.D. Lavis: "A general method to improve fluorophores for live-cell and single-molecule microscopy." *Nat. Methods*. vol. 12, no. 3, pp. 244–250, 2015.

43. J.B. Grimm, B.P. English, H. Choi, A.K. Muthusamy, B.P. Mehl, P. Dong, T.A. Brown, J. Lippincott-Schwartz, Z. Liu, T. Lionnet, and L.D. Lavis: "Bright photoactivatable fluorophores for single-molecule imaging." *Nat. Methods*. vol. 13, no. 12, pp. 985–988, 2016.

44. E. Hoogendoorn, K.C. Crosby, D. Leyton-Puig, R.M.P. Breedijk, K. Jalink, T.W.J. Gadella, and M. Postma: "The fidelity of stochastic single-molecule super-resolution reconstructions critically depends upon robust background estimation." *Sci. Rep.* vol. 4, no. 1, pp. 3854, 2015.

45. J. Min, C. Vonesch, H. Kirshner, L. Carlini, N. Olivier, S. Holden, S. Manley, J.C. Ye, and M. Unser: "FALCON: fast and unbiased reconstruction of high-density super-resolution microscopy data." *Sci. Rep.* vol. 4, no. 1, pp. 4577, 2015.

46. Stanley R. Sternberg: "Biomedical Image Processing." *Computer (Long. Beach. Calif)*. vol. 16, no. 1, pp. 22–34, 1983.

47. L. Möckl, A.R. Roy, P.N. Petrov, and W.E. Moerner: "Accurate and rapid background estimation in single-molecule localization microscopy using the deep neural network BGnet." *Proc. Natl. Acad. Sci. U. S. A.* vol. 117, no. 1, pp. 60–67, 2020.

48. S. Wolter, A. Löschberger, T. Holm, S. Aufmkolk, M.-C. Dabauvalle, S. van de Linde, and M. Sauer: "rapidSTORM: accurate, fast open-source software for localization microscopy." *Nat. Methods*. vol. 9, no. 11, pp. 1040–1041, 2012.

49. I. Izeddin, J. Boulanger, V. Racine, C.G. Specht, A. Kechkar, D. Nair, A. Triller, D. Choquet, M. Dahan, and J.B. Sibarita: "Wavelet analysis for single molecule localization microscopy." *Opt. Express*. vol. 20, no. 3, pp. 2081, 2012.

50. A. Neubeck and L. Van Gool: "Efficient Non-Maximum Suppression." 18th International Conference on Pattern Recognition (ICPR'06). pp. 850–855. *IEEE* (2006).

51. A. Aristov, B. Lelandais, E. Rensen, and C. Zimmer: "ZOLA-3D allows flexible 3D localization microscopy over an adjustable axial range." *Nat. Commun.* vol. 9, no. 1, pp. 2409, 2018.

52. R.E. Thompson, D.R. Larson, and W.W. Webb: "Precise nanometer localization analysis for individual fluorescent probes." *Biophys. J.* vol. 82, no. 5, pp. 2775–83, 2002.

53. H.B. Curry: "The method of steepest descent for non-linear minimization problems." *Q. Appl. Math.* vol. 2, no. 3, pp. 258–261, 1944.

54. K. Levenberg: "A method for the solution of certain non-linear problems in least squares." *Q. Appl. Math.* vol. 2, no. 2, pp. 164–168, 1944.

55. D.C. Sorensen: "Newton's Method with a Model Trust Region Modification." *SIAM J. Numer. Anal.* vol. 19, no. 2, pp. 409–426, 1982.

56. H.P. William, A.T. Saul, T.V. William, and P. Flaneery Brian: "Numerical Recipes in C - The Art of Scientific Computing," (1992).

57. T.A. Laurence and B.A. Chromy: "Efficient Levenberg-Marquardt Minimization of the Maximum Likelihood Estimator for Poisson Deviates." *Nat. Methods*. 2009.

58. Y. Sun: "Localization precision of stochastic optical localization nanoscopy using single frames." *J. Biomed. Opt.* vol. 18, no. 11, pp. 111418, 2013.

59. A. V. Abraham, S. Ram, J. Chao, E.S. Ward, and R.J. Ober: "Quantitative study of single molecule location estimation techniques." *Opt. Express*. vol. 17, no. 26, pp. 23352, 2009.

60. S. Liu, E.B. Kromann, W.D. Krueger, J. Bewersdorf, and K.A. Lidke: "Three dimensional single molecule localization using a phase retrieved pupil function." *Opt. Express*. vol. 21, no. 24, pp. 29462, 2013.

61. P.N. Petrov, Y. Shechtman, and W.E. Moerner: "Measurement-based estimation of global pupil functions in 3D localization microscopy." *Opt. Express*. vol. 25, no. 7, pp. 7945, 2017.

62. J. Ries: "SMAP: a modular super-resolution microscopy analysis platform for SMLM data." *Nat. Methods*. vol. 17, no. 9, pp. 870–872, 2020.

63. Y. Li, M. Mund, P. Hoess, J. Deschamps, U. Matti, B. Nijmeijer, V.J. Sabinina, J. Ellenberg, I. Schoen, and J. Ries: "Optimal 3D single-molecule localization in real time using experimental point spread functions." *Nat. Methods*. vol. 15, no. 5, pp. 367–369, 2018.

64. K.I. Mortensen, L.S. Churchman, J.A. Spudich, and H. Flyvbjerg: "Optimized localization-analysis for single-molecule tracking and super-resolution microscopy." *Nat. Methods*. vol. 7, no. 9, pp. 377–381, 2010.

65. B. Rieger and S. Stallinga: "The Lateral and Axial Localization Uncertainty in Super-Resolution Light Microscopy." *ChemPhysChem*. vol. 15, no. 4, pp. 664–670, 2014.

66. P.B. STETSON: "DAOPHOT: A COMPUTER PROGRAM FOR CROWDED-FIELD STELLAR PHOTOMETRY." *Publ. Astron. Soc. Pacific*. 1987.

67. S.J. Holden, S. Uphoff, and A.N. Kapanidis: "DAOSTORM: An algorithm for high-density super-resolution microscopy." *Nat. Methods*. vol. 8, no. 4, pp. 279–280, 2011.

68. H. Babcock, Y.M. Sigal, and X. Zhuang: "A high-density 3D localization algorithm for stochastic optical reconstruction microscopy." *Opt. Nanoscopy*. vol. 1, no. 1, pp. 6, 2012.

69. T. TAKESHIMA, T. TAKAHASHI, J. YAMASHITA, Y. OKADA, and S. WATANABE: "A multi-emitter fitting algorithm for potential live cell super-resolution imaging over a wide range of molecular densities." *J. Microsc.* vol. 271, no. 3, pp. 266–281, 2018.

70. T. Falk, D. Mai, R. Bensch, Ö. Çiçek, A. Abdulkadir, Y. Marrakchi, A. Böhm, J.

Deubner, Z. Jäckel, K. Seiwald, A. Dovzhenko, O. Tietz, C. Dal Bosco, S. Walsh, D. Saltukoglu, T.L. Tay, M. Prinz, K. Palme, M. Simons, I. Diester, T. Brox, and O. Ronneberger: "U-Net: deep learning for cell counting, detection, and morphometry." *Nat. Methods*. vol. 16, no. 1, pp. 67–70, 2019.

71. E. Nehme, L.E. Weiss, T. Michaeli, and Y. Shechtman: "Deep-STORM: super-resolution single-molecule microscopy by deep learning." *Optica*. vol. 5, no. 4, pp. 458, 2018.

72. E. Nehme, D. Freedman, R. Gordon, B. Ferdman, L.E. Weiss, O. Alalouf, T. Naor, R. Orange, T. Michaeli, and Y. Shechtman: "DeepSTORM3D: dense 3D localization microscopy and PSF design by deep learning." *Nat. Methods*. 2020.

73. P. Zelger, K. Kaser, B. Rossboth, L. Velas, G.J. Schütz, and A. Jesacher: "Three-dimensional localization microscopy using deep learning." *Opt. Express*. vol. 26, no. 25, pp. 33166, 2018.

74. A. Speiser, L.-R. Müller, P. Hoess, U. Matti, C.J. Obara, W.R. Legant, A. Kreshuk, J.H. Macke, J. Ries, and S.C. Turaga: "Deep learning enables fast and dense single-molecule localization with high accuracy." *Nat. Methods*. vol. 18, no. 9, pp. 1082–1090, 2021.

75. M. El Beheiry and M. Dahan: "ViSP: Representing single-particle localizations in three dimensions." *Nat. Methods*. vol. 10, no. 8, pp. 689–690, 2013.

76. W. Song, A. Matlock, S. Fu, X. Qin, H. Feng, C. V. Gabel, L. Tian, and J. Yi: "LED array reflectance microscopy for scattering-based multi-contrast imaging." *Opt. Lett.* vol. 45, no. 7, pp. 1647, 2020.

77. S. Cheng, S. Fu, Y.M. Kim, W. Song, Y. Li, Y. Xue, J. Yi, and L. Tian: "Single-cell cytometry via multiplexed fluorescence prediction by label-free reflectance microscopy." *Sci. Adv.* vol. 7, no. 3, 2021.

78. W. Ouyang, A. Aristov, M. Lelek, X. Hao, and C. Zimmer: "Deep learning massively accelerates super-resolution localization microscopy." *Nat. Biotechnol.* vol. 36, no. 5, pp. 460–468, 2018.

79. K. Xu, H.P. Babcock, and X. Zhuang: "Dual-objective STORM reveals three-dimensional filament organization in the actin cytoskeleton." *Nat. Methods*. vol. 9, no. 2, pp. 185–188, 2012.

80. B. Huang, S.A. Jones, B. Brandenburg, and X. Zhuang: "Whole-cell 3D STORM reveals interactions between cellular structures with nanometer-scale resolution." *Nat. Methods*. vol. 5, no. 12, pp. 1047–1052, 2008.

81. S. Mayr, F. Hauser, A. Peterbauer, A. Tauscher, C. Naderer, M. Axmann, B. Plochberger, and J. Jacak: "Localization Microscopy of Actin Cytoskeleton in Human Platelets." *Int. J. Mol. Sci.* vol. 19, no. 4, pp. 1150, 2018.

82. M.H. Symons and T.J. Mitchison: "Control of actin polymerization in live and permeabilized fibroblasts." *J. Cell Biol.* vol. 114, no. 3, pp. 503–513, 1991.

83. S.H. Lee, M. Baday, M. Tjioe, P.D. Simonson, R. Zhang, E. Cai, and P.R. Selvin: "Using fixed fiduciary markers for stage drift correction." *Opt. Express*. vol. 20, no. 11, pp. 12177, 2012.

84. Y. Wang, J. Schnitzbauer, Z. Hu, X. Li, Y. Cheng, Z.-L. Huang, and B. Huang: "Localization events-based sample drift correction for localization microscopy with redundant cross-correlation algorithm." *Opt. Express*. vol. 22, no. 13, pp. 15982, 2014.

85. R. Han, L. Wang, F. Xu, Y. Zhang, M. Zhang, Z. Liu, F. Ren, and F. Zhang: "Drift correction for single-molecule imaging by molecular constraint field, a distance minimum metric." *BMC Biophys*. vol. 8, no. 1, pp. 1, 2015.

86. A. Kechkar, D. Nair, M. Heilemann, D. Choquet, and J. Sibarita: "Real-Time Analysis and Visualization for Single-Molecule Based Super-Resolution Microscopy." *PLoS*

One. vol. 8, no. 4, pp. e62918, 2013.

87. F. Hauser and J. Jacak: "Real-Time 3D Single-Molecule Localization Microscopy Analysis Using Lookup Tables." *Biomed. Opt. Express*. vol. 12, no. 8, pp. 4955–4968, 2021.

88. Y. Le Wu, A. Tschanz, L. Krupnik, and J. Ries: "Quantitative Data Analysis in Single-Molecule Localization Microscopy." *Trends Cell Biol.* vol. 30, no. 11, pp. 837–851, 2020.

89. D.M. Owen, D.J. Williamson, A. Magenau, and K. Gaus: "Sub-resolution lipid domains exist in the plasma membrane and regulate protein diffusion and distribution." *Nat. Commun.* vol. 3, no. 1, pp. 1256, 2012.

90. B. Dudok, L. Barna, M. Ledri, S.I. Szabó, E. Szabadits, B. Pintér, S.G. Woodhams, C.M. Henstridge, G.Y. Balla, R. Nyilas, C. Varga, S.-H. Lee, M. Matolcsi, J. Cervenak, I. Kacskovics, M. Watanabe, C. Sagheddu, M. Melis, M. Pistis, I. Soltesz, and I. Katona: "Cell-specific STORM super-resolution imaging reveals nanoscale organization of cannabinoid signaling." *Nat. Neurosci.* vol. 18, no. 1, pp. 75–86, 2015.

91. M. Ester, H.P. Kriegel, J. Sander, and X. Xu: "A Density-Based Algorithm for Discovering Clusters in Large Spatial Databases with Noise." *Second Int. Conf. Knowl. Discov. Data Min.* pp. 226–231, 1996.

92. F. Levet, E. Hosy, A. Kechkar, C. Butler, A. Beghin, D. Choquet, and J.B. Sibarita: "SR-Tesseler: A method to segment and quantify localization-based super-resolution microscopy data." *Nat. Methods*. vol. 12, no. 11, pp. 1065–1071, 2015.

93. S. Lloyd: "Least squares quantization in PCM." *IEEE Trans. Inf. Theory*. vol. 28, no. 2, pp. 129–137, 1982.

94. Z. Zhang, Y. Nishimura, and P. Kanchanawong: "Extracting microtubule networks from superresolution single-molecule localization microscopy data." *Mol. Biol. Cell*. vol. 28, no. 2, pp. 333–345, 2017.

95. A. Zahedi, V. On, R. Phandthong, A. Chaili, G. Remark, B. Bhanu, and P. Talbot: "Deep Analysis of Mitochondria and Cell Health Using Machine Learning." *Sci. Rep.* vol. 8, no. 1, pp. 1–15, 2018.

96. H. Chang, M. Zhang, W. Ji, J. Chen, Y. Zhang, B. Liu, J. Lu, J. Zhang, P. Xu, and T. Xu: "A unique series of reversibly switchable fluorescent proteins with beneficial properties for various applications." *Proc. Natl. Acad. Sci.* vol. 109, no. 12, pp. 4455–4460, 2012.

97. R. Jungmann, M.S. Avendaño, J.B. Woehrstein, M. Dai, W.M. Shih, and P. Yin: "Multiplexed 3D cellular super-resolution imaging with DNA-PAINT and Exchange-PAINT." *Nat. Methods*. vol. 11, no. 3, pp. 313–318, 2014.

98. D. Sage, T.-A. Pham, H. Babcock, T. Lukes, T. Pengo, J. Chao, R. Velmurugan, A. Herbert, A. Agrawal, S. Colabrese, A. Wheeler, A. Archetti, B. Rieger, R. Ober, G.M. Hagen, J.-B. Sibarita, J. Ries, R. Henriques, M. Unser, and S. Holden: "Super-resolution fight club: assessment of 2D and 3D single-molecule localization microscopy software." *Nat. Methods*. vol. 16, no. 5, pp. 387–395, 2019.

99. S. Mayr, F. Hauser, S. Puthukodan, M. Axmann, J. Göhring, and J. Jacak: "Statistical analysis of 3D localisation microscopy images for quantification of membrane protein distributions in a platelet clot model." *PLOS Comput. Biol.* vol. 16, no. 6, pp. e1007902, 2020.